Technische Universität München
Fakultät für Physik
Bayrische Akademie der Wissenschaften
Walther-Meißner-Institut für Tieftemperaturforschung

Master's Thesis in Condensed Matter Physics

Spin Excitations in Nanostructures

Korbinian Rubenbauer

Garching, 6 July 2021

Supervisor: Prof. Dr. Rudolf Gross
Advisors: Dr. Matthias Althammer, Priv.-Doz. Dr. Hans Hübl and Tobias Wimmer

First reviewer (Supervisor): Prof. Dr. Rudolf Gross

Second reviewer: ....

Contents

Chapter 1

Introduction

"Yig was a great god. He was bad medicine. He did not forget things. In the autumn his children were hungry and wild, and Yig was hungry and wild, too." - H. P. Lovecraft in "The Curse of Yig" [LB29; Lov]

Yig, as introduced by the well-known "father of horror" H. P. Lovecraft, is the father of serpents, a half-anthropomorphic being and one of the Great Old Ones. He or it was first introduced in November 1929 in the short story "The Curse of Yig", which was published by Zealia Bishop in the magazine "Weird Tales" [LB29]. Since then and ever since any work written by H. P. Lovecraft is devoured with great thoroughness by his followers, Yig has been an indispensable part of the Lovecraft universe. But it is not only there in horror literature that Yig plays an important role. Also in the field of magnetism research YIG is a widespread and commonly used material. There, YIG is an abbreviation that stands for **y**ttrium **i**ron **g**arnet, a ferrimagnetic material used in many experiments because of its extraordinarily small magnetic damping coefficient [CKL93] going down to values of $\alpha = 4 \times 10^{-5}$ in the bulk [Mai+17; Kli+17] and 1×10^{-4} in thin films [Dub+17]. This allows both transport of spin excitation over long distances with comparatively low losses [Chu+12; Cor+15; Goe+15] and efficient and coherent excitation of its magnetization by microwave driving fields [Hen+73]. For this reason, YIG is also used in this thesis as the basic ferrimagnet. However, no systematic investigations are carried out on the material itself, but instead it is applied as an important basis for subsequent experiments.

These reside either in the general field of research on the transport of magnetic excitations, so-called magnons, or their coupling to other systems. Their common goal is to discover novel technologies for computing. This is necessary since classical electron based computing is slowly but surely reaching its upper limit as the famous Moore's law [Moo06] is coming to an end [Wal16]. In order to still meet the ever-increasing demands for more computational power, novel approaches are inevitably needed, some of which have already been pursued over the past decades [Bou+10]. One promising idea is being pursued through the field of ***spintronics*** [BSW12; BKO12; JWO15; Hir+20], which aims to replace the role of electronic charge in information processing with spin and their magnetic excitation. Already today, some commercial applications have emerged from this, such as the hard disk drive (HDD) [IBM] or, more recently, the magnetoresistive random access memory (MRAM) [Åke05]. Another point of interest, but where development is still in its infancy, is the manipulation and control of magnon currents. This can for example be realized in bilayers of magnetically ordered insulators and normal metals, paving the way towards magnetic information processing devices, i.e. magnon transistors [Goe+15; Gan+16; Cor+18; Wim+19].

This thesis tackles two aspects of spin based computation from the viewpoint of fundamental research. First, the manipulation of magnon transport under microwave pumping is examined. Here, we mainly focus on generating a better understanding of the fundamental properties of high-energy phenomena and parametric processes. Furthermore, investigations on the magnon transport under ferromagnetic resonance are performed. Second, the coupling of magnons to acoustic excitations, i.e. phonons, is more precisely elucidated.

We begin the thesis with a brief discussion of the theoretical foundations in Chapter 2. Here, the idea of a pure spin current is introduced first, followed by an explanation of the (inverse) spin Hall effect, which is commonly used to generate or electrically detect a pure spin current. Then the Karlqvist equations are treated, which describe the magnetic field of a coplanar waveguide. Afterwards, ferromagnetic resonance (FMR) and the vector-network-analyzer (VNA) measurement technique is covered. We conclude the chapter with a discussion of the spin pumping and all-electrical magnon transport phenomenon.

The first set of experiments is presented in Chapter 3. It treats the manipulation and control of pure spin currents via microwave pumping as well as parametric and high-power FMR effects in the spin pumping voltage. We start off by explaining further theoretical concepts, first the dispersion relation of dipolar exchange spin waves in thin films, and second parametric pumping effects. Next, the experimental setup and the measurement technique is displayed, followed by a discussion of the results obtained from spin pumping measurements. The chapter ends with the presentation of the all-electrical magnon transport experiments.

Chapter 4 discusses the second set of experiments that investigates the coupling between magnetic and acoustic excitations. Here, we first explain the basic conceptual setup as well as a theoretical description of the system along with its connection to experimental observables. Subsequently, a theory based simulation of the experimental system is presented. The description of the experiment, the data obtained and its comparison with theory and simulation concludes the chapter.

The thesis closes with a summary of the main achievements in Chapter 5 and an outlook on various future opportunities in Chapter 6.

Appendix A finally describes the methods used for sample fabrication and preparation. There, we do **not** discuss the detailed microscopic mechanisms of each process step, but instead present the process steps in the spirit of a "cooking recipe" to enable an easy reproduction of the samples.

Chapter 2

Theory

This chapter provides an overview of the basic theoretical concepts necessary to understand the experiments discussed later in Chapters 3 and 4. In the course of this, the concept of pure spin currents is first introduced in Section 2.1 and, directly following in Section 2.2, their generation via the spin Hall effect is discussed. Furthermore, ferromagnetic resonance, i.e. the resonant driving of a magnetization through an external microwave field, and an associated measurement technique are explained in Sections 2.4 and 2.5, respectively. Next, Section 2.6 discusses the spin pumping phenomenon, which provides an electrical access to the magnetization dynamics of a ferromagnet around ferromagnetic resonance. This chapter concludes with an explanation of all-electrical magnon transport experiments in Section 2.1.

2.1 Pure Spin Currents

An ordinary current of electrons does not only carry a charge, but also a spin. Assuming vanishing spin-flip scattering, this can be described using a two current model, where the total charge current density $\mathbf{j}_\mathrm{c}$ is split up into two parts, one for spin-up and one for spin-down electrons. The two spin species are described by the current densities $\mathbf{j}^\uparrow$ and $\mathbf{j}^\downarrow$, respectively [Cze11; BSW12; Alt18]

$$\mathbf{j}_\mathrm{c} = \mathbf{j}^\uparrow + \mathbf{j}^\downarrow. \tag{2.1}$$

If $\mathbf{j}^\uparrow \neq \mathbf{j}^\downarrow$, a finite spin current density $\mathbf{j}_\mathrm{s}$ is transported along with the conventional charge current. It can be defined as the difference between the spin-up and spin-down current density [Cze11]

$$\mathbf{j}_\mathrm{s} = -\frac{\hbar}{2e}\left(\mathbf{j}^\uparrow - \mathbf{j}^\downarrow\right), \tag{2.2}$$

where $\hbar$ is the reduced Planck constant and $-e$ the charge of a single electron with $e > 0$ the elementary charge. The factor $-\hbar/2e$ quantifies the amount of spin transported per electron, assuming that one electron with charge $-e$ carries a spin of $-\hbar/2$. In this context, one can think of several extremes for $\mathbf{j}_\mathrm{c}$ and $\mathbf{j}_\mathrm{s}$, which are shown in Fig. 2.1. Note that in general, a spin current is a tensor quantity as both the current direction and the spin polarization are three-dimensional vectors. Here, $\mathbf{j}_\mathrm{s}$ is a three-dimensional vector pointing in the direction of the spin current. It does

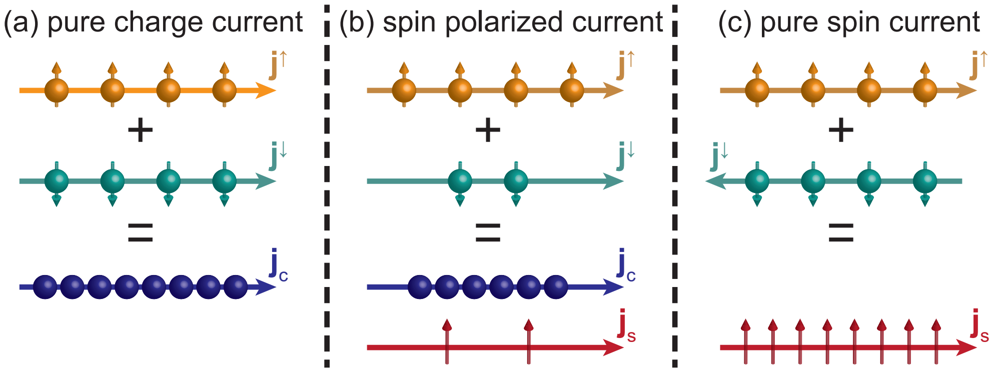

Figure 2.1: (a) Two spin current model representation of a **pure charge current** $\mathbf{j}_c$, which can be split up into two parts $\mathbf{j}^\uparrow$ ($\mathbf{j}^\downarrow$) stemming from the spin-up (spin-down) electrons. In (b) those two contributions are assumed to be unequal ($\mathbf{j}^\uparrow \neq \mathbf{j}^\downarrow$), resulting in a **spin polarized current**. (c) In the most extreme case where the two currents point in opposite direction ($\mathbf{j}^\uparrow = -\mathbf{j}^\downarrow$) a **pure spin current** is created. Adapted from [Wim16].

not contain any information about the spin polarization.

If $\mathbf{j}^\uparrow = \mathbf{j}^\downarrow$, there is a flow of charge while the flow of spins cancels out. The result is a so-called pure charge current (Fig. 2.1 (a)). One can also think of a situation where there are e.g. more spin up than spin down electrons transported, such that the resulting current carries both spin and charge. We call this a spin polarized current (Fig. 2.1 (b)). Lastly, let us consider the case where spin-up and spin-down electrons move in opposite direction. Here, there is no transport of charge, yet one of spin. It is thus called a pure spin current (Fig. 2.1 (c)).

2.2 (Inverse) Spin Hall Effect

The so-called **spin Hall effect** (SHE) is one of the most prominent ways to generate a pure spin current. It is used extensively in the experiments discussed in this thesis. Figure 2.2 (a) illustrates the basic concept of the spin Hall effect.

Here, a charge current is converted into a pure spin current via the spin-orbit interaction. The created spin current is perpendicular to both the charge current and the spin polarization axis. Using the spin Hall angle $\alpha_{\mathrm{SH}} = \sigma_{\mathrm{SH}}/\sigma_{\mathrm{el}}$, which is the ratio between the spin Hall conductivity σ_{SH} and the electrical conductivity σ_{el}, one can write the spin Hall effect induced spin current $\mathbf{j}_{\mathrm{s}}^{\mathrm{SHE}}$ as follows [Hir99]

$$\mathbf{j}_{\mathrm{s}}^{\mathrm{SHE}} = \alpha_{\mathrm{SH}} \left(\frac{\hbar}{2e}\right) \mathbf{j}_c \times \mathbf{s}. \tag{2.3}$$

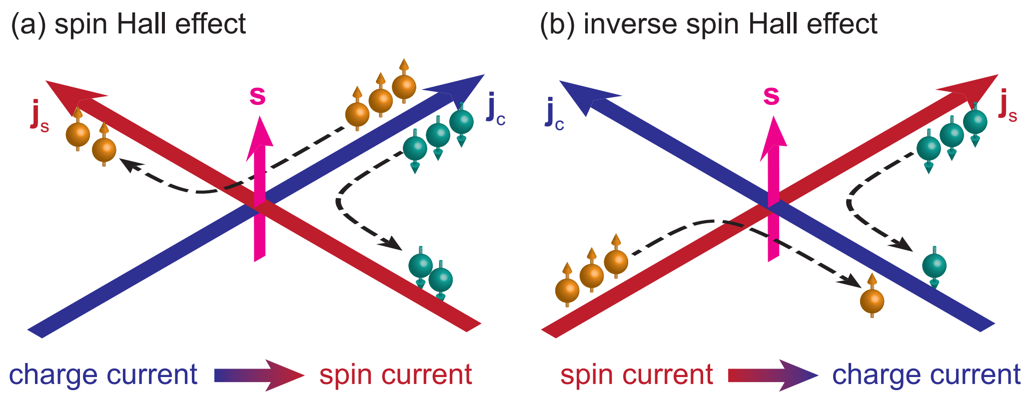

Figure 2.2: (a) Schematic illustration of the spin Hall effect. Conduction electrons are scattered depending on their spin polarization. This creates a pure spin current $\mathbf{j}_\mathrm{s}$ perpendicular to both the spin polarization $\mathbf{s}$ and the charge current $\mathbf{j}_\mathrm{c}$. On the other hand, the inverse spin Hall effect generates a charge current from a spin current, which is depicted in (b).

The spin Hall angle α_SH is a dimensionless material parameter and parameterizes the conversion efficiency between charge and spin currents. The unit vector $\mathbf{s}$ denotes the spin polarization of the pure spin current.

One can now think of the inverse effect where a spin current is transformed into a charge current by the same mechanism. It is commonly used to electrically detect a pure spin current. In analogy, it is called the **inverse spin Hall effect** (ISHE) and can be expressed in the following form [Hir99]

$$\mathbf{j}_\mathrm{c}^\mathrm{ISHE} = \alpha_\mathrm{SH} \left(-\frac{2e}{\hbar} \right) \mathbf{j}_s \times \mathbf{s}. \tag{2.4}$$

Figure 2.2 (b) visualizes the ISHE. Both the SHE and ISHE are enhanced by a strong spin-orbit coupling in the material, as this leads to an increased spin Hall conductivity σ_SH and hence an increased spin Hall angle α_SH. Since the spin-orbit coupling scales with Z^4 (where Z is the atomic charge) [GM18], this effect is most efficient for heavy metals with large nuclei such as platinum (Pt), which is used in this thesis.

2.3 Karlqvist Equations

In the experiments conducted in this thesis, microwave (RF) fields generated by a coplanar waveguide (CPW) or a CPW-like nanostructure were used to drive the magnetizations of the samples. Thus, it is important to be able to calculate an approximate magnitude of those RF fields. In this context, let us consider the

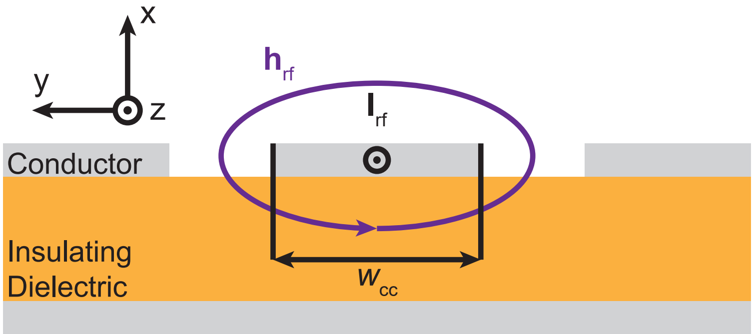

Figure 2.3: Cross section of a typical CPW. The microwave field $\mathbf{h}_{\text{rf}}$ created by an RF current $\mathbf{I}_{\text{rf}}$ through the center conductor of the CPW can be calculated with the Karlqvist equations in the given coordinate system. Adapted from [Lou16].

situation and coordinate system shown in Fig. 2.3.

Assuming an infinitely long extension of the CPW in z-direction, one can approximate the microwave field $\mathbf{h}_{\text{rf}}$ generated by the CPW with the Karlqvist equations. These describe the out-of-plane ($h_{\text{rf,oop}}$ along the x-direction) and in-plane ($h_{\text{rf,ip}}$ along the y-direction) component of the magnetic field created by an uniform current sheet in vacuum [Kar54]

$$h_{\text{rf,oop}}[x,y] = \frac{h_0}{2\pi} \ln\left[\frac{\left(y+\frac{w_{\text{cc}}}{2}\right)^2 + x^2}{\left(y-\frac{w_{\text{cc}}}{2}\right)^2 + x^2}\right], \tag{2.5}$$

$$h_{\text{rf,ip}}[x,y] = \frac{h_0}{\pi}\left(\arctan\left[\frac{y+\frac{w_{\text{cc}}}{2}}{x}\right] - \arctan\left[\frac{y-\frac{w_{\text{cc}}}{2}}{x}\right]\right). \tag{2.6}$$

Here, w_{cc} gives the center conductor width of the CPW and x (y) the distance to the center of the center conductor in out-of-plane (in-plane) direction. Moreover, h_0 is the field magnitude in the middle of the center conductor at $x = y = 0$, which can be calculated as the field amplitude of an infinite sheet [Lou16]

$$h_0 = \frac{I_{\text{rf}}}{2w_{\text{cc}}} = \frac{1}{2w_{\text{cc}}}\sqrt{\frac{P_{\text{rf}}}{Z_0}}, \tag{2.7}$$

with I_{rf} the electrical current flowing through the center conductor. Its value is calculated from the output power P_{rf} of an RF source and the input impedance Z_0 of the CPW, which is assumed to perfectly match the output impedance of the RF source, and thus $Z_0 = 50\,\Omega$.

2.4 Ferromagnetic Resonance

The uniform precession of all magnetic moments in a ferromagnet is commonly referred to as **ferromagnetic resonance** (FMR) [Kit48]. By applying a microwave field, whose frequency is equal to the precession frequency of the magnetic moments, one can resonantly drive and consequently deflect the magnetic moments from their equilibrium position. In the process, the ferromagnet absorbs energy from the microwave field.

We start off by considering the simple case of a single magnetic moment $\boldsymbol{\mu}$ subject to an external magnetic field $\mathbf{H}_{\mathrm{ext}}$. In this situation, a torque $\mathbf{T}$ acting on $\boldsymbol{\mu}$ arises due to the fact that any magnetic moment is naturally connected to an angular moment $\mathbf{L}$ via the gyromagnetic ratio γ

$$\boldsymbol{\mu} = \gamma \mathbf{L}, \tag{2.8}$$

$$\mathbf{T} = \mathrm{d}\mathbf{L}/\mathrm{dt} = -\boldsymbol{\mu} \times \mu_0 \mathbf{H}_{\mathrm{ext}}, \tag{2.9}$$

where $\mu_0 = 4\pi \times 10^{-7}\,\mathrm{NA}^{-2}$ is the vacuum permeability. Due to the torque $\mathbf{T}$, the magnetic moment $\boldsymbol{\mu}$ starts to precess around $\mathbf{H}_{\mathrm{ext}}$. This is described by the dynamic equation of motion for $\boldsymbol{\mu}$ resulting from Eqs. (2.8) and (2.9)

$$\frac{\mathrm{d}\boldsymbol{\mu}}{\mathrm{dt}} = -\gamma \boldsymbol{\mu} \times \mu_0 \mathbf{H}_{\mathrm{ext}}. \tag{2.10}$$

The frequency of the precession is given by the so-called **Larmor frequency**

$$\omega_{\mathrm{L}} = \gamma \mu_0 \left| \mathbf{H}_{\mathrm{ext}} \right|. \tag{2.11}$$

For FMR, the precession of the magnetic moments in the ferromagnet is assumed to be uniform over the entire sample (corresponding to a wavevector of $k = 0$). Consequently, FMR is typically modeled as the precession of one single macrospin, the magnetization $\mathbf{M}$, which is defined as the sum of all magnetic moments $\boldsymbol{\mu}_j$ normalized on the sample volume V

$$\mathbf{M} = \frac{1}{V} \sum_{\boldsymbol{\mu}_{\mathrm{j}} \in \mathrm{V}} \boldsymbol{\mu}_j. \tag{2.12}$$

Hereinafter, we consider a linear approximation of FMR, which is valid for small deflections of $\mathbf{M}$ from its equilibrium position. We define $\mathbf{m} = \mathbf{M}/M_{\mathrm{s}}$ as the unit vector of the magnetization by normalizing on the saturation magnetization M_{s} of the sample.

The unit magnetization $\mathbf{m}$ is brought into an effective magnetic field $\mathbf{H}_{\mathrm{eff}}$, which takes into account that the magnetic field inside a solid is not only given by the external magnetic field $\mathbf{H}_{\mathrm{ext}}$. Instead, additional contributions from the anisotropy field $\mathbf{H}_{\text{ani}}$ and the demagnetization field $\mathbf{H}_{\text{demag}}$ must be incorporated. Those three contributions together form the effective magnetic field [GM18]

$$\mathbf{H}_{\text{eff}} = \mathbf{H}_{\text{ext}} + \mathbf{H}_{\text{ani}} - \mathbf{H}_{\text{demag}}. \tag{2.13}$$

The dynamic motion of $\mathbf{m}$ in $\mathbf{H}_{\text{eff}}$ is also described by Eq. (2.10) by simply replacing $\boldsymbol{\mu}$ with $\mathbf{m}$. This was first formulated in 1935 by L. D. Landau and E. M. Lifshitz and is thus called the Landau-Lifshitz equation [LL65]. The contribution of the exchange field $\mathbf{H}_{\text{ex}}$ to $\mathbf{H}_{\text{eff}}$ is not included in Eq. (2.13), because generally $\mathbf{H}_{\text{ex}} \parallel \mathbf{m}$ and thus, as $\mathbf{m} \times \mathbf{H}_{\text{ex}} = 0$ in Eq. (2.10), $\mathbf{H}_{\text{ex}}$ has no influence on the uniform precession mode.

In reality, there is always some form of damping present in the system, which is not incorporated in Eq. (2.10). It was later included by T. L. Gilbert [Gil04] in 1955 by adding a second term that phenomenologically describes the damping. This will cause the unit magnetization $\mathbf{m}$ to slowly relax towards the effective field $\mathbf{H}_{\text{eff}}$ in a spiral motion described by the **Landau-Lifshitz-Gilbert (LLG) equation** [Gil04]

$$\frac{\mathrm{d}\mathbf{m}}{\mathrm{dt}} = -\gamma \mathbf{m} \times \mu_0 \mathbf{H}_{\text{eff}} + \alpha \mathbf{m} \times \frac{\mathrm{d}\mathbf{m}}{\mathrm{dt}}, \tag{2.14}$$

where α is the phenomenological Gilbert damping parameter that describes the strength of the damping in a given material. In the yttrium iron garnet (YIG) films used in this thesis, it is typically of the order of 10^{-4} to 10^{-2} depending on the quality of the film.

By applying an additional microwave field $\mathbf{h}_{\text{rf}}$, one can deflect the unit magnetization away from the effective magnetic field and hence counteract the afore mentioned damping. For this to work, $\mathbf{h}_{\text{rf}}$ has to be perpendicular to the effective magnetic field $\mathbf{H}_{\text{eff}}$. Figure 2.4 (a) depicts the chosen coordinate system and the considered situation, especially the direction of the forces acting on $\mathbf{m}$. Mathematically, one can treat the oscillating driving field $\mathbf{h}_{\text{rf}}$ as another contribution to the effective field $\mathbf{H}_{\text{eff}}$. Furthermore, for simplicity, the anisotropy field $\mathbf{H}_{\text{ani}}$ is set to zero for the upcoming calculations. Thus we obtain

$$\mathbf{H}_{\text{eff}} = \mathbf{H}_{\text{ext}} + \mathbf{H}_{\text{demag}} + \mathbf{h}_{\text{rf}}, \tag{2.15}$$

where $\mathbf{H}_{\text{demag}} = -\hat{N} M_{\text{s}}\, \mathbf{m}$ with $\hat{N}$ the general demagnetization tensor [MD66].

We now take a closer look at the situation depicted in Fig. 2.4 (a), where the static components $\mathbf{H}_{\text{ext}}$ and $\mathbf{H}_{\text{demag}}$ of the magnetic field are chosen to point along the z-direction. Additionally, $\mathbf{h}_{\text{rf}}$ is assumed to lie in the x-y-plane. We also consider the case where the unit magnetization $\mathbf{m}$ points along the z-direction and only its x- and y-components vary with time, such that $\mathbf{m} = (m_{\text{x}}[t], m_{\text{y}}[t], 1)$ with $m_{\text{x,y}}[t] \ll 1$. This assumption is valid for small amplitudes of the oscillation of the transverse magnetization components m_{x} and m_{y}, referring to a linear regime. For the time-

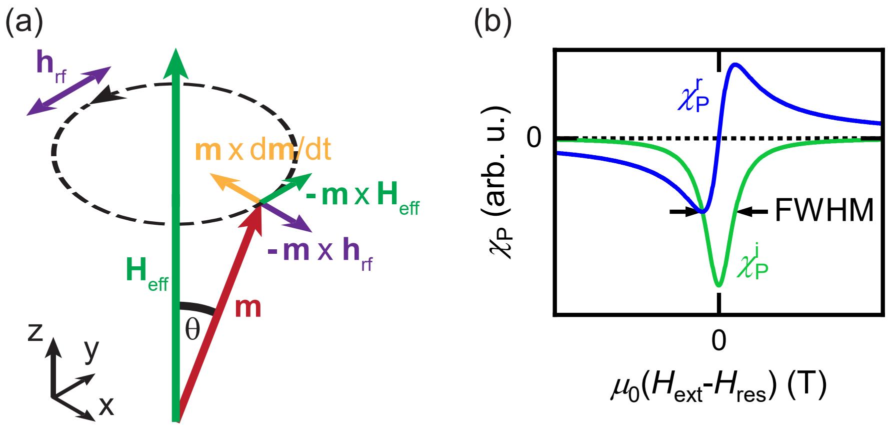

Figure 2.4: (a) When a unit magnetization $\mathbf{m}$ is brought into an effective magnetic field $\mathbf{H}_{\text{eff}}$, it starts a precessional motion around it. Damping in the magnetic system causes $\mathbf{m}$ to relax, resulting in a spiral motion towards $\mathbf{H}_{\text{eff}}$. One can counteract this effect by applying a microwave field $\mathbf{h}_{\text{rf}}$ of the same frequency as the precession of $\mathbf{m}$. The whole situation is described by the LLG equation. The linear response function of the dynamic magnetization to the RF driving field is derived from the LLG equation and given by the Polder susceptibility $\hat{\chi}_{\text{P}}$. (b) Real part $\chi_{\text{P}}^{\text{r}}$ and imaginary part $\chi_{\text{P}}^{\text{i}}$ of the Polder susceptibility as a function of the deviation of the external magnetic field H_{ext} from the resonance field H_{res}. Adapted from [Fla18].

dependence of both $\mathbf{h}_{\text{rf}}$ and $\mathbf{m}$ we choose a linear complex approach. This whole ansatz is summarized in the following with ω the angular frequency of the RF field and the magnetization precession, and i the imaginary unit

$$\mathbf{H}_{\text{eff}}\,(t) = \begin{pmatrix} h_{\text{rf,x}}\, e^{i\omega t} \\ h_{\text{rf,y}}\, e^{i\omega t} \\ H_{\text{ext}} + H_{\text{demag}} \end{pmatrix}, \quad \mathbf{m}\,(t) = \begin{pmatrix} m_{\text{x}}\, e^{i\omega t} \\ m_{\text{y}}\, e^{i\omega t} \\ 1 \end{pmatrix}, \quad m_{\text{x/y}} \ll 1. \tag{2.16}$$

Note that both m_{x} and m_{y} are complex-valued and will contain a phase shift of 90° between them in the solution, which is necessary for a precessional motion of $\mathbf{m}$. We also define the inverse Polder susceptibility $\hat{\chi}_{\text{P}}^{-1}$ in linear approximation as

$$\begin{pmatrix} h_{\text{rf,x}} \\ h_{\text{rf,y}} \end{pmatrix} = \hat{\chi}_{\text{P}}^{-1} \begin{pmatrix} m_{\text{x}} \\ m_{\text{y}} \end{pmatrix}. \tag{2.17}$$

Equation (2.16) is plugged into the LLG Eq. (2.14) and solved for the components of $\hat{\chi}_{\text{P}}^{-1}$ to find

$$\hat{\chi}_{\text{P}}^{-1} = \begin{pmatrix} H_{\text{ext}} + M_{\text{s}}(N_{\text{y}} - N_{\text{x}}) + \frac{i\omega\alpha}{\gamma\mu_0} & -\frac{i\omega}{\gamma\mu_0} \\ \frac{i\omega}{\gamma\mu_0} & H_{\text{ext}} + M_{\text{s}}(N_{\text{z}} - N_{\text{x}}) + \frac{i\omega\alpha}{\gamma\mu_0} \end{pmatrix}. \tag{2.18}$$

The unitless Polder susceptibility $\hat{\chi}_\mathrm{P}$ is obtained by inverting $\hat{\chi}_\mathrm{P}^{-1}$ and describes the response of $\mathbf{m}$ to $\mathbf{h}_\mathrm{rf}$ in the linear regime. It was first derived in 1949 by D. Polder and is given by the following expression [Pol49]

$$\hat{\chi}_\mathrm{P} = \frac{M_\mathrm{s}}{\mathrm{Det}(\hat{\chi}_\mathrm{P}^{-1})} \begin{pmatrix} H_\mathrm{ext} + M_\mathrm{s}(N_\mathrm{z} - N_\mathrm{x}) + \frac{i\omega\alpha}{\gamma\mu_0} & \frac{i\omega}{\gamma\mu_0} \\ -\frac{i\omega}{\gamma\mu_0} & H_\mathrm{ext} + M_\mathrm{s}(N_\mathrm{y} - N_\mathrm{x}) + \frac{i\omega\alpha}{\gamma\mu_0} \end{pmatrix}, \tag{2.19}$$

where $\mathrm{Det}(\hat{\chi}_\mathrm{P}^{-1})$ is the determinant of the inverse Polder susceptibility $\hat{\chi}_\mathrm{P}^{-1}$. We also already replaced the demagnetization field H_demag by a concrete expression dependent on the demagnetization factors N_x, N_y and N_z of the respective spatial directions in the demagnetization tensor $\hat{N}$. Generally speaking, the Polder susceptibility describes how the unit magnetization $\mathbf{m}$ reacts on the application of a small driving field $\mathbf{h}_\mathrm{rf}$. In more detail, the real part of $\hat{\chi}_\mathrm{P}$ describes the dispersive, while the imaginary part characterizes the dissipative reaction. They are both plotted in Fig. 2.4 (b).

The previously mentioned phase shift between m_x and m_y comes explicitly from the non-diagonal entries of $\hat{\chi}_\mathrm{P}$. We can understand this by considering e.g. an RF driving field in y-direction $\mathbf{h}_\mathrm{rf} = (0, h_{\mathrm{rf,y0}})$ and vanishing damping $\alpha = 0$ on resonance $\omega = \omega_\mathrm{res}$, where we find for the magnetization

$$M_\mathrm{s} \begin{pmatrix} m_\mathrm{x} \\ m_\mathrm{y} \end{pmatrix} = \hat{\chi}_\mathrm{P} \begin{pmatrix} h_\mathrm{rf,x} \\ h_\mathrm{rf,y} \end{pmatrix} = \frac{h_\mathrm{rf,y0} M_\mathrm{s}}{\mathrm{Det}(\hat{\chi}_\mathrm{P}^{-1})} \begin{pmatrix} \frac{i\omega_\mathrm{res}}{\gamma\mu_0} \\ H_\mathrm{ext} + M_\mathrm{s}(N_\mathrm{y} - N_\mathrm{x}) \end{pmatrix}, \tag{2.20}$$

which contains a phase shift of i between x- and y-component. This is in many ways similar to a gyroscope in classical mechanics, where a precessional motion is generally found for an object that is already spinning itself. The force stemming from a torque acting on the object is then always maximal in a position shifted forward by 90° in the rotation from where it is applied. Mathematically, this corresponds to a 90° phase shift, which is necessarily reflected in the non-diagonal entries of the susceptibility. This is analogous to the precession of a spin, as the spin itself is by definition an intrinsic form of angular momentum and thus comparable to e.g. a spinning wheel or a gyroscope.

As a next step, we want to determine the resonance frequency f_res and the linewidth of the system. The resonance condition is found as the maximal absolute value of $\hat{\chi}_\mathrm{P}$, which is reached for FMR conditions. It can be calculated by setting $\mathrm{Det}(\hat{\chi}_\mathrm{P}^{-1}) = 0$ and either looking at the real part of the solution for the resonance frequency or the imaginary part for the linewidth, respectively [Sta93]. Furthermore, this is considered in first order of the Gilbert damping parameter α, meaning that all terms of the order of $\mathcal{O}(\alpha^2)$ or higher are neglected. If we first look at the real part of the solution and solve for the resonance frequency, we obtain the famous Kittel formula [Kit48]

$$f_{\mathrm{res}} = \frac{\omega}{2\pi} = \frac{\gamma\mu_0}{2\pi}\sqrt{\left(H_{\mathrm{ext}} + \left(N_{\mathrm{z}} - N_{\mathrm{x}}\right) M_{\mathrm{s}}\right)\left(H_{\mathrm{ext}} + \left(N_{\mathrm{y}} - N_{\mathrm{x}}\right) M_{\mathrm{s}}\right)}. \tag{2.21}$$

In the scope of this thesis, only the solution for a magnetic field in the plane of a thin film is relevant. Note that the surface normal of a film is parallel to the x-axis in the chosen coordinate system. The RF field $\mathbf{h}_{\mathrm{rf}}$ is further assumed to point along the y-axis which is typical for the later experiments. To determine the demagnetization factors $N_{\mathrm{x/y/z}}$ we therefore consider an infinitely extended magnetic thin film lying in the y-z-plane with its normal vector along the x-axis. It is magnetized in-plane, with $\mathbf{m}$ pointing in z-direction, as shown in Fig. 2.4 (a). In this case, the demagnetization factors are

$$N_{\mathrm{x}} = 0\,; \quad N_{\mathrm{y}} = 0\,; \quad N_{\mathrm{z}} = 1. \tag{2.22}$$

Under these constraints, we now calculate $\mathrm{Det}(\hat{\chi}_{\mathrm{P}}^{-1}) = 0$ again, but this time resolve for H_{ext} to obtain

$$H_{\mathrm{ext}} = -\frac{M_{\mathrm{s}}}{2} + \sqrt{\left(\frac{M_{\mathrm{s}}}{2}\right)^2 + \left(\frac{\omega}{\gamma\mu_0}\right)^2} - i\,\frac{\omega\alpha}{\gamma\mu_0}. \tag{2.23}$$

As mentioned before, the real part of Eq. (2.23) gives the resonance magnetic field H_{res}. By multiply with μ_0, we obtain the resonance field for in-plane magnetized thin films

$$\mu_0 H_{\mathrm{res}} = -\frac{\mu_0 M_{\mathrm{eff}}}{2} + \sqrt{\left(\frac{\mu_0 M_{\mathrm{eff}}}{2}\right)^2 + \left(\frac{2\pi}{\gamma}\right)^2 f_{\mathrm{res}}^2}, \tag{2.24}$$

where we substituted M_{s} with $M_{\mathrm{eff}} = M_{\mathrm{s}} + H_{\mathrm{ani}}$. The effective magnetization M_{eff} incorporates the anisotropy field H_{ani}, which in this case is assumed to point in the out-of-plane direction (corresponding to an uniaxial out-of-plane anisotropy). We can now replace the gyromagnetic ratio with its definition for an electron $\gamma = g_{\mathrm{e}}\mu_{\mathrm{B}}/\hbar$, where μ_{B} is the Bohr magneton and g_{e} an effective g-factor of the electrons in the ferromagnet, which is typically $g_{\mathrm{e}} \approx 2$. This gives us the final form that will be used to fit the data in the later experiments

$$\mu_0 H_{\mathrm{res}} = -\frac{\mu_0 M_{\mathrm{eff}}}{2} + \sqrt{\left(\frac{\mu_0 M_{\mathrm{eff}}}{2}\right)^2 + \left(\frac{2\pi\hbar}{g_{\mathrm{e}}\mu_{\mathrm{B}}}\right)^2 f_{\mathrm{res}}^2}. \tag{2.25}$$

Generally, Eq. (2.25) describes the external magnetic field amplitude $\mu_0 H_{\mathrm{res}}$ required to drive the magnetization $\mathbf{m}$ in ferromagnetic resonance, given that an RF driving field $\mathbf{h}_{\mathrm{rf}}$ of constant frequency f_{res} is applied.

As a next step, we study the dissipative aspect of FMR by considering the imaginary part of the solution to $\mathrm{Det}(\hat{\chi}_{\mathrm{P}}^{-1}) = 0$ given in Eq. (2.23). The result can be related to the half-width-half-maximum ΔH_{HWHM} of the resonance peak [Sta93]

$$\Delta H_{\mathrm{HWHM}} = \frac{2\pi\alpha}{\mu_0\gamma} f_{\mathrm{res}}. \tag{2.26}$$

The experimentally observed linewidth is usually the full-width-half-maximum, i.e. $\Delta H_{\mathrm{FWHM}} = 2\,\Delta H_{\mathrm{HWHM}}$ (see also Fig. 2.4 (b)). Moreover, the linewidth in experiments typically has a finite positive value even for $f_{\mathrm{res}} = 0$. To account for this, a constant inhomogeneous contribution $\Delta H_{\mathrm{inhom}}$ is added to Eq. (2.26). Multiplying everything with μ_0 again, we obtain the frequency dependence of the experimentally observed linewidth ΔH_{FMR} of ferromagnetic resonance

$$\mu_0\Delta H_{\mathrm{FMR}} = \mu_0\Delta H_{\mathrm{inhom}} + \frac{4\pi\alpha}{\gamma} f_{\mathrm{res}}. \tag{2.27}$$

Lastly, we can define the ellipticity ϵ of the magnetization precession cone from the Polder susceptibility [Mül+21]

$$\epsilon = \sqrt{1 + \frac{\mu_0 M_{\mathrm{eff}}}{\mu_0 H_{\mathrm{ext}}}}. \tag{2.28}$$

It quantifies the deformation of the precession from a perfect circle towards an ellipse. It is minimal ($\epsilon = 1$) for a perfectly circular precession and goes to infinity for an infinitely elliptical, i.e. a linear precession.

2.5 Microwave Transmission Spectroscopy Probing Magnetization Excitation

One way to experimentally measure the frequency dependent Polder susceptibility during ferromagnetic resonance is to use a vector network analyzer (VNA) to detect the phase-sensitive microwave power absorption of the ferromagnetic sample.

Here, we measure the transmission signal through a coplanar waveguide (CPW) as the complex S_{21} parameter of a vector network analyzer (VNA). The CPW is used to provide the RF driving field (given by the Karlqvist equations, see Section 2.3) to the ferromagnetic sample. Generally, S_{21} is defined as the ratio between the input and output complex voltage V_1 and V_2

$$S_{21} = \frac{V_2}{V_1} = \frac{|V_2|}{|V_1|} e^{i(\psi_2 - \psi_1)}, \tag{2.29}$$

where $|V_j|$ is the magnitude and ψ_j the phase of port j. The transmission signal S_{21} consists of two parts. First, a background signal S_{21}^0 created by the measurement setup, which is independent of the sample. Second, the change in signal ΔS_{21} caused by the absorption of the sample, which can be calculated as follows [Sil+16; Ber+18]

$$\Delta S_{21} = \frac{S_{21} - S_{21}^0}{S_{21}^0}. \tag{2.30}$$

The absorption of microwave power by the sample around ferromagnetic resonance can be treated as an induced complex inductance L_0 that adds up onto the inductance $Z_0 = 50\,\Omega$ of the unloaded CPW. This causes a signal change ΔS_{21}, which can be expressed using a voltage divider model [Mül19]

$$\Delta S_{21} = -\frac{1}{2}\frac{i\omega L_0}{Z_0 - i\omega L_0}. \tag{2.31}$$

An exact expression for L_0 is derived by Berger *et al.* [Ber+18] and implemented into Eq. (2.31) in [Mül19]. The result is an expression for the complex S_{21} parameter

$$S_{21} = S_{21}^0 \left(1 + \Delta S_{21}\right) = S_{21}^0 - i\, C_{\mathrm{geo}}\, e^{i\psi} \left(\chi_{\mathrm{yy}} + \chi_{\mathrm{xx}}\right). \tag{2.32}$$

For simplification, all geometric and setup parameters are combined in the constant C_{geo}, which gives the amplitude of the change in S_{21} around the FMR. The total phase change of the signal is also summed up in a single parameter $\psi = \psi_2 - \psi_1$. χ_{yy} and χ_{xx} are the diagonal entries of the Polder susceptibility $\hat{\chi}_{\mathrm{P}}$ as discussed in Section 2.4 (Eq. (2.17)). If we, without loss of generality, assume that the RF field created by the CPW is parallel to the y-axis, then $h_{\mathrm{rf,x}} = 0$ and we can write the components of the unit magnetization $\mathbf{m}$ perpendicular to the effective magnetic field H_{eff} as follows

$$m_{\mathrm{x}} M_{\mathrm{s}} = \chi_{\mathrm{xy}} h_{\mathrm{rf,y}}, \tag{2.33}$$
$$m_{\mathrm{y}} M_{\mathrm{s}} = \chi_{\mathrm{yy}} h_{\mathrm{rf,y}}. \tag{2.34}$$

Since we are mostly interested in the changes ΔS_{21} of the transmission, we can plug Eq. (2.34) back into Eq. (2.32) and conclude for the magnitude of ΔS_{21}

$$|\Delta S_{21}| \propto |m_{\mathrm{y}}| \propto |\mathbf{m}_\perp|, \tag{2.35}$$

where $\mathbf{m}_\perp$ is the component of the magnetization perpendicular to the effective magnetic field. Equation (2.35) gives a direct connection between the observable ΔS_{21} and $|\mathbf{m}_\perp|$, which quantifies the deflection of $\mathbf{m}$ from its equilibrium position. We will come back to this later in Section 4.1.2.

2.6 Spin Pumping

In this thesis, a lot of emphasis is put on a phenomenon called **spin pumping**, which was first proposed by Tserkovnyak *et al.* [TBB02a] in 2002. In general, an externally driven magnetization precession in a ferromagnetic insulator (FMI) pumps a net spin current into an adjacent normal metal (NM). This spin current can be transformed into a charge current via the inverse spin Hall effect, which can be measured as a voltage drop across the normal metal perpendicular to both the direction and polarization of the pumped spin current. We refer to this signal as the **spin pumping voltage**. In this chapter, we will go step by step over the details behind this process. A more extensive explanation can be found e.g. in the PhD thesis of Franz Dominik Czeschka [Cze11], whose approach we will closely follow.

We consider a bilayer of a normal metal (NM) and a ferromagnetic insulator (FMI). The magnetization of the FMI is driven by an external RF field. This causes a periodic oscillation of the magnetization component $\mathbf{m}_\perp$ perpendicular to the effective magnetic field as discussed in Section 2.4. Thus, an AC spin current $\mathbf{j}_\mathrm{s}^\mathrm{pump}$ arises across the interface between the ferromagnetic insulator and the normal metal. It can be calculated using time-dependent scattering theory [TBB02a]

$$\mathbf{j}_\mathrm{s}^\mathrm{pump} = \frac{\hbar}{4\pi}\left(g_r^{\uparrow\downarrow}\mathbf{m}\times\frac{d\mathbf{m}}{dt} - g_i^{\uparrow\downarrow}\frac{d\mathbf{m}}{dt}\right). \tag{2.36}$$

Here, $\mathbf{m}(t)$ is the time dependent order parameter of the ferromagnet, i.e the unit vector of the magnetization. $g^{\uparrow\downarrow} = g_r^{\uparrow\downarrow} + i g_i^{\uparrow\downarrow}$ is the complex spin-mixing conductance split up in its real $g_r^{\uparrow\downarrow}$ and imaginary $g_i^{\uparrow\downarrow}$ component. Note that the direction of $\mathbf{j}_\mathrm{s}^\mathrm{pump}$ gives the spin polarization and **not** the spin current direction. For FMR experiments, the form of the first term in Eq. (2.36) is similar to the Gilbert term in the LLG Eq. (2.14), thus generating an additional contribution to the damping of the magnetization precession. The second term can be seen as an additional field causing a shift of the resonance position.

Generally, the spin-mixing conductance $g^{\uparrow\downarrow}$ depends on the FMI|NM interface. It describes how effective a spin current can be transferred across a certain interface and is conceptually similar to the impedance in electrical transport. In this thesis, yttrium iron garnet (YIG) is used as a FMI and platinum (Pt) as a NM. For the YIG|Pt interface, the imaginary component of the spin-mixing conductance is a lot smaller than the real one $g_i^{\uparrow\downarrow} \ll g_r^{\uparrow\downarrow}$ [Che+13; Alt+13]. Thus, the second term of Eq. (2.36) can be neglected in the following discussion, simplifying it to

$$\mathbf{j}_\mathrm{s}^\mathrm{pump} = \frac{\hbar}{4\pi} g_r^{\uparrow\downarrow}\mathbf{m}\times\frac{d\mathbf{m}}{dt}. \tag{2.37}$$

Consequently, the polarization of the created spin current $\mathbf{j}_\mathrm{s}^\mathrm{pump}$ is perpendicular to both $\mathbf{m}$ and $d\mathbf{m}/dt$. Its magnitude is proportional to $g_r^{\uparrow\downarrow}$. This is depicted in Fig. 2.5.

This spin current consists out of an AC and a DC component. The DC part is obtained via time averaging of Eq. (2.37). By assuming a circular magnetization precession, one finds that the x- and y-component of $\mathbf{j}_\mathrm{s}^\mathrm{pump}$ vanishes, whereas the

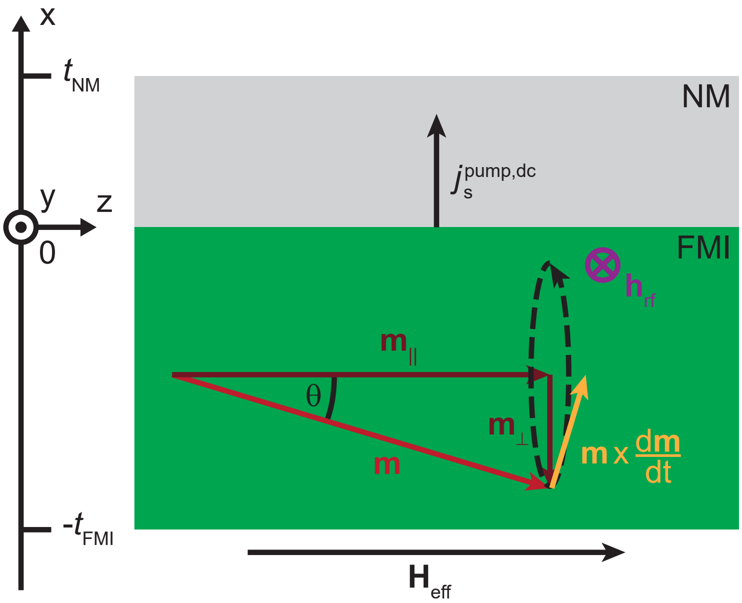

Figure 2.5: A bilayer of a normal metal (NM) on top of a ferromagnetic insulator (FMI). The unit magnetization $\mathbf{m}$ of the FMI is aligned along an effective magnetic field $\mathbf{H}_{\text{eff}}$. Thus, $\mathbf{m}$ can be split up into a part parallel $\mathbf{m}_{||}$ and one perpendicular $\mathbf{m}_\perp$ to $\mathbf{H}_{\text{eff}}$. An RF field $\mathbf{h}_{\text{rf}}$ drives the precessional motion of the magnetization around the effective field with cone angle θ. As a result, a spin current $j_{\text{s}}^{\text{pump,dc}}$ is pumped into the NM. Adapted from [Cze11].

component polarized in z-direction retains a finite DC amplitude of [Mos+10]

$$j_{\text{s}}^{\text{pump,dc}} = \frac{\hbar\omega_{\text{mw}}}{4\pi} g_r^{\uparrow\downarrow} \sin^2\theta, \tag{2.38}$$

where ω_{mw} is the frequency of the RF driving field $\mathbf{h}_{\text{rf}}$ and θ the precession cone angle, i.e. the angle between $\mathbf{H}_{\text{eff}}$ and $\mathbf{m}$.

So far, we neglected anisotropy fields as well as demagnetization fields. In thin films however, they can have a strong influence on the shape of the magnetization precession, deforming it from a circular to an elliptical motion. Those additional contributions can all be included in the effective magnetic field $\mathbf{H}_{\text{eff}}$, leading to a correction prefactor c_{corr} multiplied with $j_{\text{s}}^{\text{pump,dc}}$. Further details about this issue can be found in Ando *et al.* [AYS09]. However, they are not discussed within the scope of this thesis.

The spin current $j_{\text{s}}^{\text{pump,dc}}$ pumps magnetic excitations into the NM. In the ideal case, the NM acts as a perfect spin sink, where all spins injected by $j_{\text{s}}^{\text{pump,dc}}$ relax via spin flip scattering and/or leave the interface sufficiently fast [TBB02a]. The total spin current through the interface would hence be given by $j_{\text{s}}^{\text{tot}} \approx j_{\text{s}}^{\text{pump,dc}}$.

Especially, a backflow of spins from the NM into the FMI could be disregarded. In reality, however, $j_{\mathrm{s}}^{\mathrm{pump,dc}}$ creates a spin accumulation at the NM interface, resulting in a backflow of spins $j_{\mathrm{s}}^{\mathrm{back,dc}}$ from the NM into the FMI. The total spin current is then given by [TBB02b]

$$j_{\mathrm{s}}^{\mathrm{tot}} = j_{\mathrm{s}}^{\mathrm{pump,dc}} - j_{\mathrm{s}}^{\mathrm{back,dc}}. \tag{2.39}$$

In extreme cases, this can result in a vanishing total spin current $j_{\mathrm{s}}^{\mathrm{tot}} \approx 0$ when spin-flip scattering is absent [TBB02b]. In general, one can correct for this effect by using an effective spin mixing conductance $g_{\mathrm{eff}}^{\uparrow\downarrow}$ instead of $g^{\uparrow\downarrow}$, which is assumed in the following discussion.

As stated before, the total spin current $j_{\mathrm{s}}^{\mathrm{tot}} \neq 0$ pumps magnetic excitations from the FMI into the NM. This gives rise to a spin chemical potential bias at the FMI|NM interface. Consequently, a spin current is created and transported diffusely through the metal in a non-conserved way. It can be described by the one-dimensional spin diffusion equation [KM63; BM65; LG67]

$$\frac{\partial \mu_s}{\partial t} = D_{\mathrm{NM}} \frac{\partial^2 \mu_s}{\partial x^2} - \frac{\mu_s}{\tau_{\mathrm{sf}}}. \tag{2.40}$$

Here, $\mu_s = \mu_s^{\uparrow} - \mu_s^{\downarrow}$ is the difference in chemical potential between the individual spin directions, D_{NM} the spin diffusion constant in a normal metal and τ_{sf} the spin flip scattering time. In the following, we will consider the steady state and the strong spin-flip scattering ($\omega_{\mathrm{mw}}\tau_{\mathrm{sf}} \ll 1$) limit, where the partial derivative of the spin accumulation with respect to time vanishes ($\partial \mu_s / \partial t = 0$) [TBB02b]. Eq. (2.40) is solved under the two boundary conditions that first the spin current vanishes at the interface between the NM and the vacuum [TBB02b]

$$j_{\mathrm{s}}\left[x = t_{\mathrm{NM}}\right] = 0 = \left.\frac{\partial \mu_s}{\partial x}\right|_{x = t_{\mathrm{NM}}}, \tag{2.41}$$

and second the spin current at the FMI|NM interface is continuous [TBB02b]

$$j_{\mathrm{s}}\left[x = 0\right] = j_{\mathrm{s}}^{\mathrm{tot}} = -\frac{\hbar}{2e}\frac{\sigma_{\mathrm{NM}}}{e}\left.\frac{\partial \mu_s}{\partial x}\right|_{x=0}. \tag{2.42}$$

Here, σ_{NM} is the electrical conductivity of the NM. The result is a dependency of the spin chemical potential (and thus the spin current) on the distance to the FMI|NM interface, eventually creating a spin current in the normal metal [Mos+10]

$$j_{\mathrm{s}}\left[x\right] = j_{\mathrm{s}}^{\mathrm{tot}} \frac{\sinh\left[\frac{t_{\mathrm{NM}} - x}{\lambda_{\mathrm{sd}}}\right]}{\sinh\left[\frac{t_{\mathrm{NM}}}{\lambda_{\mathrm{sd}}}\right]}. \tag{2.43}$$

Here, j_s is the amplitude of the spin current directed out of the interface/film plane (in x-direction). It depends mainly on the ratio between the thickness t_{NM} of the NM and the spin diffusion length λ_{sd} in the NM. In the case of small thicknesses $t_{\mathrm{NM}} < \lambda_{\mathrm{sd}}$, this corresponds to a nearly linear decay with the distance x to the interface. For thick layers $t_{\mathrm{NM}} \gg \lambda_{\mathrm{sd}}$, the spin current already vanishes close to the FMI|NM interface and never reaches the upper edge of the NM [Cze11].

The inverse spin Hall effect (see Section 2.2) converts the spin current $j_s[x]$ from Eq. (2.43) in the NM into a transverse charge current. This is described by Eq. (2.4) which is repeated in the following

$$\mathbf{j}_c^{\mathrm{ISHE}}[x] = \alpha_{\mathrm{SH}} \left(-\frac{2e}{\hbar}\right) j_s[x]\, \hat{\mathbf{e}}_x \times \mathbf{s},$$

where $\hat{\mathbf{e}}_x$ is the unit vector in x-direction. Here, we can already see that the charge current $\mathbf{j}_c^{\mathrm{ISHE}}$ has the same dependence on the distance to the FMI|NM interface as the spin current $j_s[x]$. As it further has to be perpendicular to both $\mathbf{s}$ (spin orientation) and $\mathbf{j}_s$ (which points in the normal direction of the film), the charge current $\mathbf{j}_c^{\mathrm{ISHE}}$ flows in y-direction in the chosen coordinate system. This is shown in Fig. 2.6. Note that the point of view has been rotated by 90° around the x-axis compared to Fig. 2.5, allowing for an illustration of the ISHE induced charge current in the NM.

In open circuit conditions, the charge current $\mathbf{j}_c^{\mathrm{ISHE}}$ causes a charge imbalance, resulting in a positive charge at one end and a negative charge at the other end of the normal metal. This generates a compensating electrical field $\mathbf{E}_{\mathrm{comp}}$ pointing in the opposite direction of the charge current, which grows in strength until an equilibrium state between $\mathbf{j}_c^{\mathrm{ISHE}}$ and $\mathbf{E}_{\mathrm{comp}}$ is reached.

The compensating electrical field can be calculated assuming a uniform shape, which is valid in cases where the dimension of the sample in y-direction is much larger than in x-direction, i.e. when its thickness is much smaller than its length. This applies to all designs used in the later experiments. Detailed calculations can be found in [Mos+10] and [Cze11]. Both eventually derive the following expression for the compensating electric field

$$\mathbf{E}_{\mathrm{comp}} = \frac{e\, g_{\mathrm{eff}}^{\uparrow\downarrow} \left(\alpha_{\mathrm{SH}} \lambda_{\mathrm{sd}} \tanh\left[t_{\mathrm{NM}}/(2\lambda_{\mathrm{sd}})\right]\right) \hat{\mathbf{e}}_x \times \mathbf{s}}{\sigma_{\mathrm{FMI}} t_{\mathrm{FMI}} + \sigma_{\mathrm{NM}} t_{\mathrm{NM}}}\, \omega_{\mathrm{mw}} c_{\mathrm{corr}} \sin^2\theta, \tag{2.44}$$

where e is the elementary charge, σ_{FMI} (t_{FM}) the conductivity (thickness) of the ferromagnetic insulator layer, σ_{NM} the conductivity of the normal metal layer and ω_{mw} the RF driving frequency. Over the entire length L_{NM} of the normal metal, this

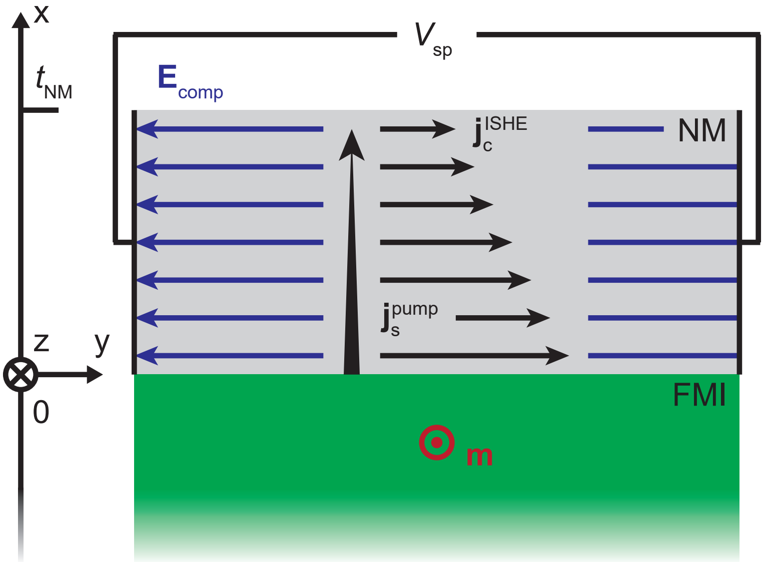

Figure 2.6: A spin current $\mathbf{j}_s^{\text{pump}}$ is pumped from a FMI into a NM. This creates a charge current $\mathbf{j}_c^{\text{ISHE}}$ in the NM via the inverse spin Hall effect. It is perpendicular to both $\mathbf{j}_s^{\text{pump}}$ and the unit magnetization $\mathbf{m}$ of the FMI. Consequently, the charge separation generates a compensating electrical field $\mathbf{E}_{\text{comp}}$ that can be measured as a spin pumping voltage V_{sp}. Adapted from [Cze11].

results in the so-called **spin pumping voltage**

$$V_{\text{sp}} = E_{\text{comp}} L_{\text{NM}} = \frac{e\, g_{\text{eff}}^{\uparrow\downarrow} \left(\alpha_{\text{SH}} \lambda_{\text{sd}} \tanh\left[t_{\text{NM}}/(2\lambda_{\text{sd}})\right]\right)}{\sigma_{\text{FMI}} t_{\text{FMI}} + \sigma_{\text{NM}} t_{\text{NM}}}\, \omega_{\text{mw}} c_{\text{corr}} L_{\text{NM}} \sin^2\theta. \qquad (2.45)$$

An important conclusion from Eq. (2.45) is the quadratic dependence of the spin pumping voltage V_{sp} on the sine of the cone angle θ of the magnetization precession ($V_{\text{sp}} \propto \sin^2\theta$), which has been confirmed in experiments [Cze+11; Zho+16].

If we split the unit magnetization into a part parallel to the effective field ($\mathbf{m}_{\|}$) and one perpendicular to it ($\mathbf{m}_{\perp}$), then $|\mathbf{m}_{\perp}| = |\mathbf{m}| \sin\theta$ and we can rewrite the dependence of the spin pumping voltage on the cone angle in terms of the magnetization components

$$V_{\text{sp}} \propto \sin^2\theta \propto \frac{|\mathbf{m}_{\perp}|^2}{|\mathbf{m}|^2}. \qquad (2.46)$$

We will refer to this later in Section 4.1.2 in this thesis.

Recapitulating, a resonantly driven magnetization in a ferromagnetic insulator pumps a spin current into an adjacent normal metal film. Via the inverse spin Hall effect, this spin current is eventually transformed into a measurable electric voltage, the so-called **spin pumping voltage**. This allows for easy electronic access to the magnetization dynamics in a FMI.

2.7 All-Electrical Magnon Transport Experiments

All-electrical magnon spin transport measurements can be realized with structured bilayers of ferromagnetic insulators (FMI) and normal metals (NM). In this thesis, structures similar to the one depicted in Fig. 2.7 are used, where two normal metal strips are deposited on top of a ferromagnetic insulator. The strips are electrically insulated and physically separated by a distance d. A charge current is applied on the left normal metal strip, which we call injector. Via the spin Hall effect (see Section 2.2) a spin accumulation is created at the interface to the ferromagnetic insulator. This leads to a finite spin transport across the interface, whose properties will be discussed in detail later in this section.

The spin transport across the interface injects magnons into the ferromagnetic insulator creating an imbalance in the magnon density. This gives rise to a magnon current diffusing in all directions. It can be described by the magnon spin diffusion equation, which was already discussed in Eq. (2.40) in the context of spin pumping (see Section 2.6). Similar to before, we consider the steady state limit under strong spin-flip scattering. This time, however, we expand the spacial derivative to three dimensions and obtain for the magnon chemical potential μ_m

$$D_\mathrm{FMI}\nabla^2\mu_\mathrm{m} = \frac{\mu_\mathrm{m}}{\tau_\mathrm{m}}, \tag{2.47}$$

where D_FMI is the magnon diffusion constant in a ferromagnetic insulator and τ_m the magnon spin lifetime, which summarizes all non-conserving magnon processes. From this, one can define the magnon diffusion length as

$$\lambda_\mathrm{m} = \sqrt{D_\mathrm{FMI}\,\tau_\mathrm{m}}. \tag{2.48}$$

Equation (2.47) can be solved analytically in one dimension only. A more detailed discussion of this case can be found in Section 2.6.

Coming back to the structure depicted in Fig. 2.7, some of the magnons diffusing through the ferromagnetic insulator reach the interface to the second normal metal strip, which we call detector. There, the inverse process compared to the injector takes place: The magnons scatter at the interface and create a spin accumulation in the normal metal, which gives rise to a spin current that is transformed into a charge current via the inverse spin Hall effect. Similar to spin pumping (see Section 2.6), this charge current can be measured as an electrical voltage.

The whole process is only possible for a parallel configuration of the spin polariz-

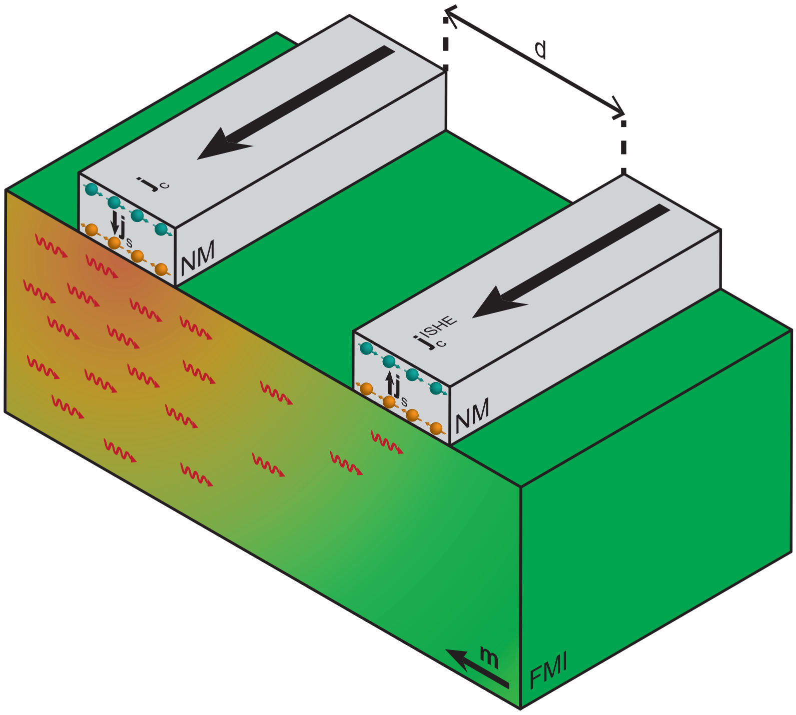

Figure 2.7: 3D schematic of a typical device for all-electrical magnon transport experiments. Two normal metal (NM) strips are structured on top of a ferromagnetic insulator (FMI). A charge current $\mathbf{j}_{\mathrm{c}}$ is driven through the left strip (injector). Via the spin Hall effect, a transverse spin current $\mathbf{j}_{\mathrm{s}}$ is created. This gives rise to a spin accumulation at the NM|FMI interface, which injects magnons into the ferromagnetic insulator via interfacial spin-flip scattering. Those magnons are transported diffusely in all directions through the ferromagnetic insulator. Some of them reach the second normal metal strip, where they are detected via the inverse spin Hall effect, eventually resulting in a charge current $\mathbf{j}_{\mathrm{c}}^{\mathrm{ISHE}}$ in the right strip (detector). Adapted from [Wim16].

ation $\mathbf{s}$ of the electrons in the normal metal and the unit magnetization $\mathbf{m}$ of the ferromagnetic insulator. This can be explained by taking a closer look at the scattering processes at the NM|FMI interface in the injector. In general, a spin current $\mathbf{j}_{\mathrm{s,int}}$ across the interface between a metal and a magnetically ordered insulator can be described as follows [BT15]

$$\begin{aligned}\mathbf{j}_{\mathrm{s,int}} =& \frac{1}{4\pi}\left(g_{\mathrm{eff,i}}^{\uparrow\downarrow} + g_{\mathrm{eff,r}}^{\uparrow\downarrow}\,\mathbf{m}\times\right)\left(\mu_{\mathrm{s}}^{0}\,\mathbf{s}\times\mathbf{m} - \hbar\,\frac{d\mathbf{m}}{dt}\right)\\ &+\left\{g\left(\mu_{\mathrm{m}} + \mu_{\mathrm{s}}^{0}\,\mathbf{s}\cdot\mathbf{m}\right) + S\left(T_{\mathrm{m}} - T_{\mathrm{e}}\right)\right\}\mathbf{m},\end{aligned} \tag{2.49}$$

where $\mu_{\mathrm{s}}^{0}\,\mathbf{s}$ denotes the spin accumulation at the interface due to the spin current in the normal metal with μ_{s}^{0} the spin chemical potential at the interface and $\mathbf{s}$ the three-dimensional unit vector of the spin. Note that consequently and opposing to the equation for the (inverse) spin Hall effect, $\mathbf{j}_{\mathrm{s,int}}$ does **not** point into the spin current direction, but rather gives the polarization of the transported spin. Besides, μ_{m} is the magnon chemical potential characterizing a non equilibrium magnon accumulation or depletion in the ferromagnetic insulator. Furthermore, $g \propto (T/T_{\mathrm{c}})^{3/2} g^{\uparrow\downarrow}$, where T is the temperature and T_{c} the Curie temperature. It describes the spin conductance across the interface for $\mathbf{s} \parallel \mathbf{m}$ and at finite temperatures. Thermally driven spin currents independent of the spin polarization $\mathbf{s}$ are characterized by the spin Seebeck coefficient S. In addition, T_{m} and T_{e} are the temperatures of the magnons in the ferromagnetic insulator and the electrons in the normal metal, respectively. Note that for low temperatures, $g^{\uparrow\downarrow}_{\mathrm{eff,i}}$ and $g^{\uparrow\downarrow}_{\mathrm{eff,r}}$ still hold finite values, whereas g and S both approach zero [BT15].

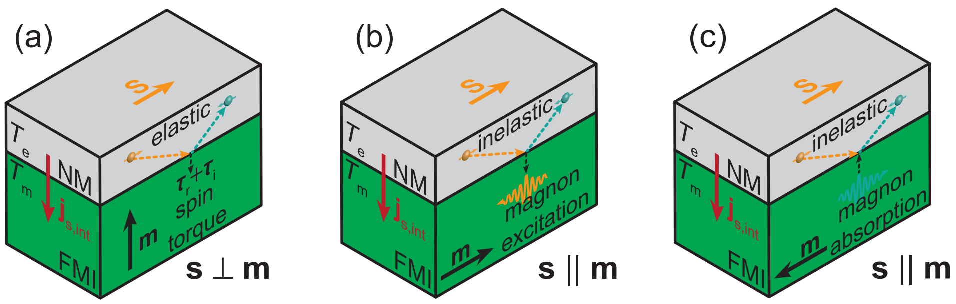

Figure 2.8: Spin flip scattering processes for electrons at the interface between a normal metal (NM) and a ferromagnetic insulator (FMI). (a) When $\mathbf{s} \perp \mathbf{m}$ the spin flip scattering is of elastic nature. Two spin torques τ_{r} and τ_{i} acting on $\mathbf{m}$ arise. In (b) and (c) where $\mathbf{s} \parallel \mathbf{m}$, the spin flip scattering at the interface is inelastic. (b) When $\mathbf{s}$ and $\mathbf{m}$ are parallel to each other, this leads to an excitation of magnons in the ferromagnetic insulator due to spin angular momentum conservation. (c) When $\mathbf{s}$ and $\mathbf{m}$ are antiparallel, magnons are absorbed from the ferromagnetic insulator. Thermal injection via a temperature difference between T_{e} and T_{m} is possible in all three cases, independent of the geometric configuration. Adapted from [Wim21].

In order to better understand Eq. (2.49), the upcoming paragraphs discuss the individual terms in turn in detail. Generally, the first line of Eq. (2.49) describes non-thermal processes which are finite even at zero temperature, while the second line is only non-zero for finite temperatures.

The terms in the first line $\propto \mu_{\mathrm{s}}^0 \, \mathbf{s} \times \mathbf{m}$ are largest when $\mathbf{s} \perp \mathbf{m}$, which is shown in Fig. 2.8 (a). Here, the electrons scatter elastically off the interface and perform a spin flip, thus creating a surplus of $\hbar$ in spin angular momentum. Since spin angular momentum is a conserved quantity, this has to be compensated by the ferromagnetic insulator. Consequently, two torques

$$\tau_{\mathrm{r}} \propto g^{\uparrow\downarrow}_{\mathrm{eff,r}} \, \mathbf{m} \times (\mathbf{s} \times \mathbf{m}) \, ,$$

and

$$\tau_{\mathrm{i}} \propto g_{\mathrm{eff,i}}^{\uparrow\downarrow} \left(\mathbf{s} \times \mathbf{m}\right),$$

arise, which transfer the excess spin angular momentum into the ferromagnetic insulator. On the one hand, τ_{r} is commonly referred to as damping like torque [Slo89; Ber96]. It transfers a loss of the transverse spin momentum of the scattered electrons into the magnetic order of the ferromagnetic insulator. On the other hand, τ_{i} is called field-like torque. It directly acts onto the magnetization of the ferromagnetic insulator.

The loss of transverse spin momentum via τ_r scales with the real part of $g_{\mathrm{eff}}^{\uparrow\downarrow}$, hence corresponding to the dissipative part of the spin-mixing conductance. The imaginary part retains the original spin momentum of the scattered electrons and therefore corresponds to the non-dissipative part. This concept is somewhat similar to the real and imaginary components of the electrical impedance, which correspond to dissipative and non-dissipative processes in electrical circuits, respectively. As previously discussed in Section 2.6, the terms $\propto d\mathbf{m}/dt$ are responsible for the spin pumping phenomenon.

The first term in the second line of Eq. (2.49) proportional to g describes inelastic scattering processes at the interface. They are depicted in Fig. 2.8 (b) and (c) and are largest when $\mathbf{s} \parallel \mathbf{m}$. When $\mathbf{s}$ and $\mathbf{m}$ are parallel (antiparallel) to each other, magnons in the thermal spectrum are either excited into (depleted from) the ferromagnetic insulator. Note that this process is only possible for finite temperatures. It is also the main mechanism used for magnon injection in structures like the one shown in Fig. 2.7. The voltage created by such magnons at the detector strip is called **SHE induced magnon transport voltage $V_{\mathrm{det}}^{\mathrm{SHE}}$**.

The preceding discussion implies that a specific geometry ($\mathbf{s} \not\perp \mathbf{m}$) is required to observe all-electrical magnon transport and explains why its amplitude is dependent on the angle φ between the magnetization $\mathbf{m}$ of the ferromagnetic insulator and the polarization $\mathbf{s}$ of the spin accumulation at the interface. It is largest when they are parallel and zero when they are perpendicular to each other. Thus, this injection process follows an angle symmetry proportional to $\cos\varphi$. Since the detection is done with the exact inverse process to the injection, the same angular dependence arises for it. The total transport signal of spin Hall injected magnons is therefore proportional to

$$V_{\mathrm{det}}^{\mathrm{SHE}} \propto \cos^2\left(\varphi\right). \tag{2.50}$$

This effect is commonly referred to as **all-electrical magnon transport**.

Coming back to Eq. (2.49), we still need to discuss the second term in line two, which is proportional to S. It is independent of the relative orientation between $\mathbf{s}$ and $\mathbf{m}$, but still requires a finite temperature. Here, a difference between the electron temperature T_e and the magnon temperature T_m causes spin angular momentum to be injected into or absorbed from the ferromagnetic insulator. Its polarization is always antiparallel to $\mathbf{m}$ because the thermal excitation acts as a disturbance of the magnetic order in the ferromagnetic insulator. This is commonly known as the **spin Seebeck effect** (SSE) [Xia+10; Uch+10]. Magnons created in this fashion form the second contribution to the voltage arising at the detector strip. We call it the **Joule heating induced magnon transport voltage** $V_\mathrm{det}^\mathrm{therm}$.

In an experiment with a structure similar to the one shown in Fig. 2.7, the charge current $\mathbf{j}_\mathrm{c}$ through the injector strip will cause Joule heating due to the electrical resistance of the normal metal strip. This will introduce the required temperature gradient between T_e and T_m, thus exciting magnons via the spin Seebeck effect. Because the electrical voltage at the detector strip is generated via the same process as for SHE induced magnons, the detection process of thermally injected magnons is also sensitive on φ, whereas this is **not** the case for their injection. In total, this gives rise to the following angular dependence for the Joule heating induced voltage

$$V_\mathrm{det}^\mathrm{therm} \propto \cos(\varphi)\,. \tag{2.51}$$

The voltage measured at the detector strip is a superposition of both the SHE and Joule heating induced transport voltage. In the experiment, we use their different symmetries to separate their contributions to the total voltage. This will be discussed later in Section 3.4.1.

Chapter 3

Microwave Control of Magnons

For incoherent excitation, the transport of magnetic excitation in a ferrimagnetic insulator is described by the diffusion of magnons. We want to take a look at the explicit case discussed in Section 2.7, where magnons are injected into a ferrimagnetic insulator at one spot and the amount of magnons reaching a second spot is measured. One can now think of ways to influence and control this magnon transport. This can be implemented, for example, by the DC injection of magnons in between the two spots, which reduces or enhances the damping of the magnon transport. The first observation of this phenomenon was reported by Cornelissen *et al.* [Cor+18] in 2018. In extreme cases, this can even lead to a zero-damping state as shown by Wimmer *et al.* [Wim+19] one year later. However, there are also other methods to control the magnon transport, one of which works via microwave injection of magnons into the ferrimagnetic insulator through ferromagnetic resonance. This was first reported by Liu *et al.* [Liu+19] in 2019. In this thesis, we expand on this concept by increasing the driving power to reach the parametric pumping regime. Besides magnon transport, we also simultaneously measure the DC spin pumping voltage up to the nonlinear regime.

3.1 Theoretical Concepts

Generally, when a driving force with high power is applied to a harmonic oscillator, so-called parametric effects can occur. Here, a second resonance condition is met when the frequency of the driving force is equal to twice the resonance frequency of the oscillator. Such an effect was first reported by Michael Faraday in 1831 [Far31] and can even be observed and modeled in peculiar systems such as rainworms [MP20]. Here, we focus on the parametric excitation of the magnetization of a ferrimagnet, where there are two main mechanisms and geometries in which such effects can occur. The upcoming section discusses those processes and their connection to the magnon dispersion relation from a theoretical point of view.

3.1.1 Dispersion of Dipolar Exchange Spin Waves in Thin Films

In magnetic materials, the spins can create waves, similar to phonons in a lattice, for example. The dependency of the angular frequency ω_m of those spin waves on their wavevector k is given by the dispersion relation, which is influenced by both the dipolar and the exchange interaction between the spins. For ferromagnetic thin films magnetized in-plane, which are used in this thesis, the dispersion relation is given by [HP40; KS86; KP10]

$$\omega_\mathrm{m}\left[k, H_\mathrm{ext}\right] = \mu_0\gamma \sqrt{\begin{aligned}&\left(H_\mathrm{ext} + Jk^2 + M_\mathrm{s}\frac{1-\exp[-kd]}{kd}\right)\\ &\times\left(H_\mathrm{ext} + Jk^2 + M_\mathrm{s}\left(1 - \frac{1-\exp[-kd]}{kd}\right)\sin^2[\phi]\right)\end{aligned}}, \tag{3.1}$$

where $J = 2A/(\mu_0 M_\mathrm{s})$ is the spin stiffness parameter calculated from the exchange constant $A = 3.7\,\mathrm{pJ\,m^{-1}}$ [Kli+14] for YIG and the saturation magnetization M_s. Further, d is the thickness of the film, $\mathbf{H}_\mathrm{ext}$ the external magnetic field and $\phi \sphericalangle (\mathbf{k}, \mathbf{m})$ the angle between the wavevector $\mathbf{k}$ of the spin wave and the magnetization $\mathbf{m}$ of the ferromagnetic thin film. Note that ω_m does not only depend on the amplitude $k = |\mathbf{k}|$ of the wavevector, but also on the magnitude $H_\mathrm{ext} = |\mathbf{H}_\mathrm{ext}|$ of the applied external magnetic field.

Equation (3.1) spans up a continuous array of dispersion relations, one for each value of ϕ and thus for each propagation direction of the spin wave. Hereinafter, we will mainly consider two extreme cases: (i) the magnetization and the wavevector are parallel to each other (backward volume mode, $\phi = 0$) or (ii) they are perpendicular to each other (Damon-Eshbach mode, $\phi = \pi/2$). Figure 3.1 depicts both dispersion relations and the array of dispersions in between for an arbitrarily chosen external magnetic field amplitude of $\mu_0 H_\mathrm{ext} = 50\,\mathrm{mT}$ and a film thickness of $d = 23.5\,\mathrm{nm}$, which is equal to the one of the film used in the experiment.

Obviously, the dispersion of the uniform mode with $k = 0$ is independent of the angle ϕ. On the one hand, for finite values of k, the Damon-Eshbach mode immediately starts off with a positive slope. Its minimal frequency is thus reached at $k = 0$. For low k values, an approximately linear dependence ensues. On the other hand, the backward volume mode initially exhibits a negative slope and a minimal value $\omega_\mathrm{m}(k_\mathrm{min})$ for a finite $k_\mathrm{min} > 0$. After that, the dispersion starts to increase again similar to the Damon-Eshbach mode. The depth of the so created dip in the backward volume mode strongly depends on the film thickness d. The thinner the films the less pronounced is the dip. For larger values of k, the modes are separated by a constant offset and show a parabolic shape $\omega_\mathrm{m} \propto k^2$ dominated by the exchange interaction. The anisotropic dipolar interaction prevails for small k values. This can be understood by imagining a spin wave as a series of spins that are slightly tilted against each other. Both the dipolar and the exchange interaction energetically favor a parallel alignment of the spins. For large wavevectors, the wavelength of the spin wave is small and neighboring spins are strongly tilted with respect to each other. Because the exchange interaction is stronger than the dipolar interaction at close ranges, its resulting energy contribution dominates. Consequently, for large

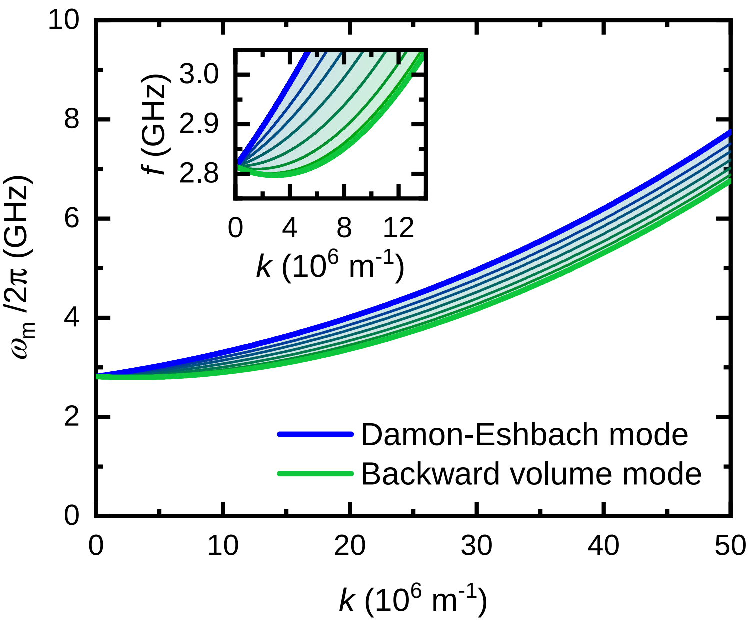

Figure 3.1: Dispersion relation of dipolar exchange spin waves in a magnetic thin film. The dispersion consists of an array of curves for each angle ϕ between the wavevector $\mathbf{k}$ and the magnetization $\mathbf{m}$ of the film. The two limiting cases are plotted for the backward volume mode ($\phi = 0$) and the Damon-Eshbach mode ($\phi = \pi/2$). The inset in the upper left depicts a zoom of the dispersion, highlighting the minimum for the backward volume mode.

k values, the dispersion is well approximated by the exchange dominated parabolic branch according to $\omega_\mathrm{m} = \mu_0\gamma \left(H_\mathrm{ext} + Jk^2\right)$. For small wavevectors, the wavelength of the spin wave is relatively large and the individual spins are only slightly tilted with respect to their direct neighbors. Stronger tilts only arise when considering spins which are far away from each other, i.e. long distances. There, the exchange interaction is weak and the dipolar interaction dominates.

Changes of the external magnetic field H_ext do **not** change the shape of the dispersion, but instead shift it upward for higher field amplitudes and downward for lower field amplitudes. Consequently, the minimal energy required to excite a magnon, which is given by the minimum $\omega_\mathrm{m}(k_\mathrm{min})$ of the dispersion, is also increased or decreased, respectively. Magnons can only be excited if the excitation energy exceeds this minimal magnon energy. Exciting magnons with larger k values generally also requires more energy. In this picture, the condition for ferromagnetic resonance is for example given by the value $H_\mathrm{ext,fmr}$ for which the frequency of the magnons with $k = 0$ aligns with the frequency ω_rf of the RF driving field ($\omega_\mathrm{m}[0, H_\mathrm{ext,fmr}] = \omega_\mathrm{rf}$). We can use this idea to obtain an expression for the dependence between the resonance frequency ω_res and the respective resonant magnetic field H_res by calculating the limit $k \to 0$ of Eq. (3.1)

$$\omega_{\mathrm{res}} \equiv \lim_{k \to 0} \omega_{\mathrm{m}} \left[k, H_{\mathrm{res}}\right] = \mu_0 \gamma \sqrt{H_{\mathrm{res}} \left(H_{\mathrm{res}} + M_{\mathrm{s}}\right)}. \tag{3.2}$$

We solve this for H_{res} under the condition of parametric pumping ($\omega_{\mathrm{res}} = 2\pi f_{\mathrm{rf}}/2$), where two magnons with half the energy (and thus the frequency) of the photon are created

$$\mu_0 H_{\mathrm{onset}} \equiv \mu_0 H_{\mathrm{res}} = -\frac{\mu_0 M_{\mathrm{eff}}}{2} + \sqrt{\left(\frac{\mu_0 M_{\mathrm{eff}}}{2}\right)^2 + \left(\frac{\pi}{\gamma}\right)^2 f_{\mathrm{rf}}^2}, \tag{3.3}$$

Here, similar to Section 2.4, we replaced the saturation magnetization M_{s} with an effective magnetization M_{eff}. We define the obtained H_{res} as the onset magnetic field $\mu_0 H_{\mathrm{onset}}$ for parametric pumping because it is the highest field value for which magnons can be excited into the Damon-Eshbach mode via parametric pumping. In the experiment, it is equal to the highest magnetic field where parametric effects can be observed. At lower field values, magnons can be excited into states with higher k values. As this is energetically more demanding, the observed amplitude of the parametric pumping will slowly decrease for a decreasing magnetic field amplitude. Note that Eq. (3.3) is similar to the Kittel description of the resonance field of FMR (see Eq. (2.25) in Section 2.4). Only the resonance condition is adjusted to the parametric case where $f_{\mathrm{res}} = f_{\mathrm{rf}}/2$.

This is only correct because magnons are excited mainly into the Damon-Eshbach mode by parametric pumping [Kre+18; Noa+19]. If one could directly excite magnons in the backward volume mode, one could not just take the limit for $k \to 0$, but would have to calculate the minimum of the backward volume mode $\omega_{\mathrm{m}}(k_{\mathrm{min}})$ instead. Even so, in the experiments presented in this thesis, the used films were so thin that the depth of the dip only corresponds to a shift of the dispersion via a magnetic field change of around 2 mT.

3.1.2 Parametric Pumping

Previously in Section 2.4, we already discussed ferromagnetic resonance. Here, we consider the same situation again, where a magnetization $\mathbf{m}$ is brought into a static effective magnetic field $\mathbf{H}_{\mathrm{eff}}$. At this point, we have to discern two fundamentally different situations. (i) **Perpendicular pumping**, where the RF driving field $\mathbf{h}_{\mathrm{rf}}$ is applied perpendicular to the effective magnetic field and thus to the magnetization in equilibrium without driving field ($\mathbf{h}_{\mathrm{rf}} \perp \mathbf{H}_{\mathrm{eff}}$). (ii) **Parallel pumping**, where the RF driving field is parallel to the magnetization ($\mathbf{h}_{\mathrm{rf}} \parallel \mathbf{H}_{\mathrm{eff}}$). The former occurs in the same geometry as ferromagnetic resonance. Both situations are depicted in Fig. 3.2. For both of them, the RF driving field is twice the frequency of the magnetization precession. This is the characterizing feature of parametric pumping. In this section, we discuss the details of each case starting with (i) perpendicular

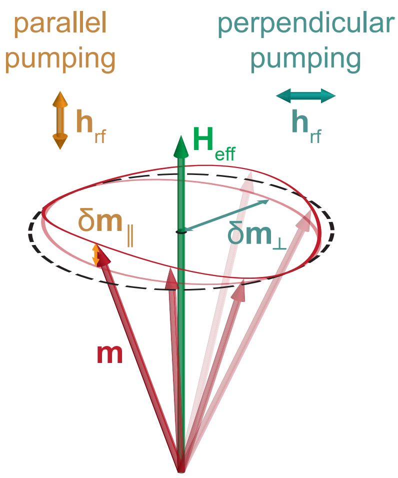

Figure 3.2: Elliptically precessing unit magnetization vector $\mathbf{m}$ in a static effective magnetic field $\mathbf{H}_{\mathrm{eff}}$. The RF driving field $\mathbf{h}_{\mathrm{rf}}$ is applied either perpendicular or parallel to the effective field $\mathbf{H}_{\mathrm{eff}}$ and thus couples to either $\delta\mathbf{m}_{\perp}$ or $\delta\mathbf{m}_{\parallel}$.

pumping and ending with (ii) parallel pumping.

Perpendicular pumping was first observed in 1953 by R. W. Damon [Dam53] and one year later by N. Bloembergen and S. Wang [BW54]. A few years later in 1957 H. Suhl gave the first theoretical description of the observed phenomenon [Suh57]. With some slight variations, his theory is still used until today.

As described above, perpendicular pumping corresponds to the same geometry as ferromagnetic resonance (cyan in Fig. 3.2). For low powers of the RF driving field $\mathbf{h}_{\mathrm{rf}}$, we are in the linear regime and thus only observe the ferromagnetic resonance peak when the frequency of the RF driving field equals the frequency of the uniform magnetization precession ($\omega_{\mathrm{rf}} = \omega_{\mathrm{m}}$). If one increases the driving power up into the nonlinear regime, higher order processes start to play a significant role. A schematic diagram of those is shown in Fig. 3.3. In a rough estimate, the nonlinear regime is reached when the amplitude of the driving field exceeds the linewidth of the magnetic material. Assuming i.e. a linewidth of $\sim 5\,\mathrm{mT}$, a driving power of $\sim 8\,\mathrm{dBm}$ would be needed for the structure used in the experiments (for which we can set $w_{\mathrm{cc}} = 500\,\mathrm{nm}$, $Z_0 = 50\,\Omega$, $x = 0\,\mathrm{m}$ and $y = 500\,\mathrm{nm}$ in Eq. (2.5)).

For perpendicular pumping, two additional features appear if one measures the power absorption of the FMI as a function of the external magnetic field. First, a premature saturation of the main ferromagnetic resonance peak can be seen. This is caused by the 4 magnon scattering process shown in Fig. 3.3 (b), which is called second order Suhl instability. Here, the photons from the external RF driving field create magnons in the uniform mode ($k = 0$). This is the usual process for

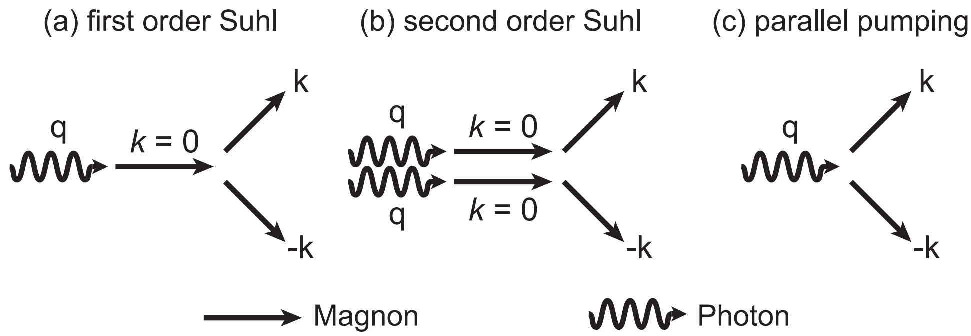

Figure 3.3: Schematic representation of microscopic processes involved in parametric pumping. (a) and (b) are related to perpendicular pumping, while (c) corresponds to the parallel pumping instability. The magnons are depicted as straight arrows, photons as wiggly lines. Adapted from [Spa64; RA90].

ferromagnetic resonance. We now consider a scattering event where two magnons with $k = 0$ scatter with each other, creating two new magnons. Because momentum- and energy conservation is required, those magnons have a finite k value with the same amplitude but of opposite sign. Furthermore, they have the same frequency as the original magnons and are hence typically scattered into the backward volume mode (or more generally into modes with small angles ϕ that exhibit a minimum in the dispersion at finite wavevectors $k_{\mathrm{min}} > 0$) [Spa64]. Otherwise, there are no accessible states in the dispersion. When the RF driving field exceeds a critical value (its exact expression is discussed together with the other processes at the end of this section), this scattering process becomes relevant. It transports excess energy from the uniform mode into spin waves with finite k values. A premature saturation and broadening of the ferromagnetic resonance peak is the consequence [Spa64; RA90]. The theoretically expected shape of a measurement signal is shown in Fig. 3.4 (a). It is backed up and confirmed by experimental data [AAS11; San+11; Zho+16; Dus+19].

Second, a subsidiary peak appears at lower magnetic fields than the main resonance at FMR. This is depicted in Fig. 3.4 (b) and is caused by the 3 magnon scattering event shown in Fig. 3.3 (a), which is called first order Suhl instability. Here, similar to before, one magnon with $k = 0$ is created from a photon of the RF driving field. It scatters into two magnons with the same finite k value of opposite sign. Contrary to before, their frequencies are half the one of the original magnon due to energy conservation [Spa64]. Equations (3.4) and (3.5) exemplarily state the momentum and energy conservation law for the first order Suhl instability

$$\hbar k_0 = \hbar k_1 + \hbar k_2 = 0 \qquad \rightarrow k_1 = -k_2, \tag{3.4}$$

$$\hbar \omega_{\mathrm{m},0} = \hbar \omega_{\mathrm{m},1} + \hbar \omega_{\mathrm{m},2} \qquad \rightarrow \omega_{\mathrm{m},1} = \omega_{\mathrm{m},2} = \frac{\omega_{\mathrm{m},0}}{2}. \tag{3.5}$$

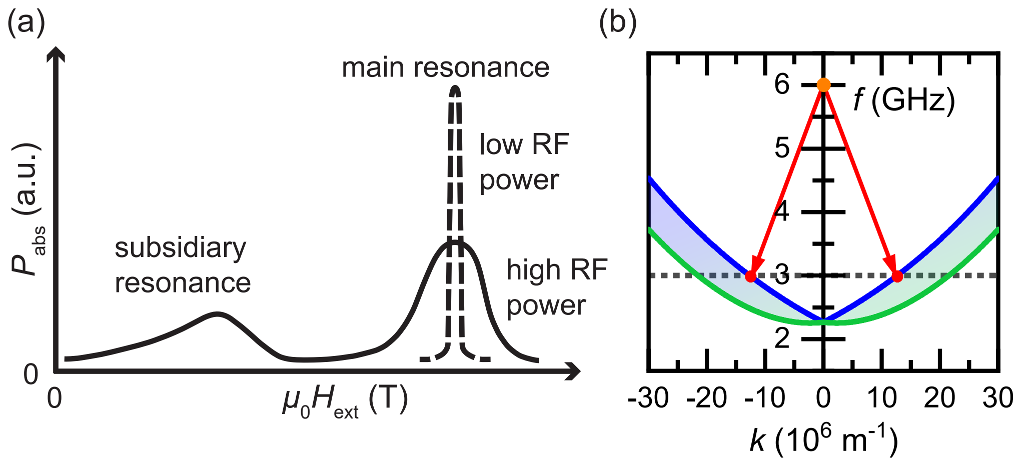

Figure 3.4: (a) Typical behavior of the power absorption P_{abs} of the FMI as a function of the external magnetic field H_{ext} in the perpendicular pumping geometry. The dashed line shows the signal for low powers of the RF driving field, whereas the continuous line depicts it for high powers. Adapted from [Spa64]. (b) Creation process of magnons by parallel pumping visualized via the dispersion relation. A photon (orange dot) with e.g. 6 GHz frequency creates two magnons (red dots) with 3 GHz frequency each.

Here, the index 0 represents the original $k = 0$ magnon and the indices 1 and 2 the two scattered magnons.

In the case (ii) of parallel pumping, the RF driving field is applied parallel to the magnetization. The associated microscopic process is depicted in Fig. 3.3 (c). In contrast to the perpendicular pumping, the chosen geometry does **not** allow for a conversion of photons of the RF driving field into magnons with $k = 0$. Consequently, **no** ferromagnetic resonance peak will appear. Only after exceeding a certain critical driving field amplitude, a subsidiary peak will appear at lower fields. Here, the photons of the driving field are directly converted into two magnons with half the photon frequency and the same finite k value of opposite sign [Spa64].

One requirement for such a direct conversion is a finite ellipticity in the precession of the magnetization, as depicted in Fig. 3.2. The ellipticity causes a variation $\delta\mathbf{m}_{\parallel}$ of the magnetization component parallel to the effective field. It is easily created by e.g. an anisotropy between two perpendicular directions in the ferromagnetic insulator [BPH17]. In the later experiments, the magnetic moment is always aligned in the plane of a thin film such that one of the two directions perpendicular to it is pointing out of and the other in the film plane. This is sufficient to create a relevant anisotropy and thus ellipticity. The RF driving field can only couple and deflect the so created variation $\delta\mathbf{m}_{\parallel}$. This also graphically makes clear why the frequency of the driving field needs to be double the frequency of the created magnons. If we take a look at the variance of $\delta\mathbf{m}_{\parallel}$, which in the end describes the "up and down movement" of the magnetization, one can easily see that the eigenfrequency of this oscillation is exactly twice the precession frequency of the magnetization around $\mathbf{H}_{\text{eff}}$.

By now, parallel pumping is a well-established technique in experiments, and its consequences were mostly studied using Brillouin light scattering spectrocopy (BLS). One of the most famous achievements was the creation of a magnon Bose-Einstein condensation by Demokritov *et al.* in 2006 [Dem+06], which could be reproduced and confirmed by various other works in later years [Ser+14; Cla+15]. It proves that incredibly high magnon densities can be reached via parametric pumping. By its basics, this fact seems very promising for the amplification of the all-electrical magnon transport previously discussed in Section 2.7. A more detailed analysis of experimental achievements through parallel pumping can be found in the physical review by T. Brächer, P. Pirro and B. Hillebrands [BPH17].

As mentioned above, a threshold behavior is typical for all parametric processes, where parametric pumping effects can only be observed once a critical driving field power/amplitude h_{c} is reached. Before that, an increase in driving power does **not** result in any noticeable differences. After the threshold is overcome, an increase in pumping power is strongly reflected in an increase of the power absorption by the ferromagnetic insulator [Spa64].

The critical fields for all processes are calculated in detail by S. M. Rezende and F. M. de Aguiar [RA90] or M. Sparks [Spa64]. They depend among other things on the angle ϕ between the wavevector $\mathbf{k}$ and the unit magnetization $\mathbf{m}$, and are minimal for a specific angle ϕ_{min}, which is different for each of the scattering processes shown in Fig. 3.3 [RA90].

	first order Suhl	second order Suhl	parallel pumping
ϕ_{min}	$\pi/4$	0	$\pi/2$

The minimal critical field $h_{\text{c,s1,min}}$ of the first order Suhl and $h_{\text{c,pp,min}}$ of the parallel instability are equal to each other, which makes it difficult to differentiate between those two effects. They are calculated for the respective values of ϕ_{min} given above to obtain [Spa64; RA90]

$$\mu_0 h_{\text{c,pp,min}} = \mu_0 h_{\text{c,s1,min}} = \frac{\omega_{\text{p}} \mu_0 \Delta H_{\text{k}}}{\mu_0 \gamma M_{\text{s}}}, \tag{3.6}$$

where $\omega_{\text{p}} = \omega_{\text{rf}}$ is the pumping frequency and ΔH_{k} the magnon linewidth, i.e the relaxation frequency of magnons with wavevector k in units of the magnetic field. This means that the critical field is smaller for a lower RF driving field frequency or magnon linewidth, and higher for a smaller saturation magnetization.

The minimal threshold field $h_{\text{c,s2,min}}$ for the second order Suhl instability in YIG is typically a factor of $\approx 10^{-2}$ smaller than the critical field for parallel pumping or the first order Suhl instability [RA90]. Generally, it is given by [Spa64; RA90]

$$\mu_0 h_{\mathrm{c,s2,min}} = \frac{\mu_0 \Delta H_0}{2} \sqrt{\frac{\Delta H_{\mathrm{k}}}{M_{\mathrm{s}}}}, \tag{3.7}$$

where ΔH_0 is the energy relaxation frequency of the uniform precession mode with $k = 0$ in units of the magnetic field.

3.2 Experiment

All-electrical magnon transport experiments are usually based on a similar sample layout. Since we want to investigate nonlinear and high-energy effects such as the parametric pumping instabilities discussed above, the experimental setup has to be optimized to generate as high amplitudes of the RF driving field as possible. The underlying idea pursued for this purpose is the one of an on-chip antenna, which can generate these high field amplitudes due to its close proximity and small width. This section describes the experimental setup, sample layout and measurement technique used to obtain all of the data presented later in this chapter.

3.2.1 Setup

The nanostructure used in the experiment is based on the magnon transport structure introduced in Fig. 2.7 of Section 2.7, for which we use platinum (Pt) as a normal metal and yttrium iron garnet (YIG) as a ferromagnetic insulator. In order to generate a microwave driving field, a third strip of a different conducting material is introduced in between the two normal metal strips. It serves as a microstrip antenna. The entire structure is depicted in Fig. 3.5.

The two Pt strips are identical in their physical dimensions. They are $t_{\mathrm{Pt}} = 5\,\mathrm{nm}$ thick, $w_{\mathrm{Pt}} = 500\,\mathrm{nm}$ wide and $l_{\mathrm{Pt}} = 50\,\mathrm{\mu m}$ long. The microwave antenna in the middle has the same width $w_{\mathrm{ant}} = 500\,\mathrm{nm}$ as the Pt strips, but is with $t_{\mathrm{ant}} = 85\,\mathrm{nm}$ around 17 times thicker. It is build as a trilayer stack of a thin ruthenium (Ru), a thick copper (Cu) layer and a thin tantalum (Ta) cap (Ru(7 nm)|Cu(75 nm)|Ta(3 nm)). The edge to edge distance between the antenna and each Pt strip is $w = 250\,\mathrm{nm}$, such that the edge to edge distance between the Pt strips is 1 µm. Both the Pt strips and the antenna are contacted via Al wire bonding onto square bonding pads with 200 µm side length. Figure 3.6 shows a schematic visualization and a microscope picture of this structure.

As depicted in Fig. 3.5, an AC current $I_{\mathrm{inj}} = I_{\mathrm{inj},0} \sin \omega_{\mathrm{ac}} t$ with $I_{\mathrm{inj},0} = 200\,\mathrm{\mu A}$ and $f_{\mathrm{ac}} = \omega_{\mathrm{ac}}/(2\pi) = 7.121\,\mathrm{Hz}$ was driven through the left Pt strip using a Keithley 6221 DC and AC current source, thus serving as a magnon injector. The right Pt strip is the detector. It was connected to a Stanford Research Systems Model SR560 low noise preamplifier in order to generate sufficiently large signal amplitudes. The

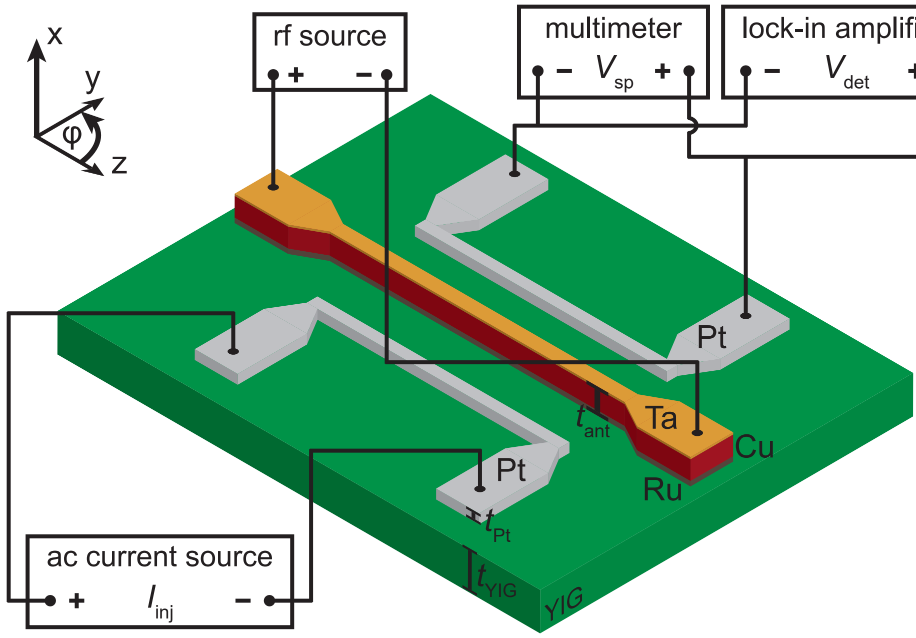

Figure 3.5: Schematic illustration of the experiment setup and coordinate system. Two platinum (Pt) strips are nanostructured on top of a yttrium iron garnet (YIG) thin film. The left Pt strip is connected to an AC current source and serves as an injector of magnons into the YIG. The right Pt strip is connected to both a multimeter and a lock-in amplifier and thus used as a magnon detector. The third strip in the middle consists of a trilayer of Ru|Cu|Ta. It is connected to an RF source and serves as a microwave antenna. Inspired from [Wim21].

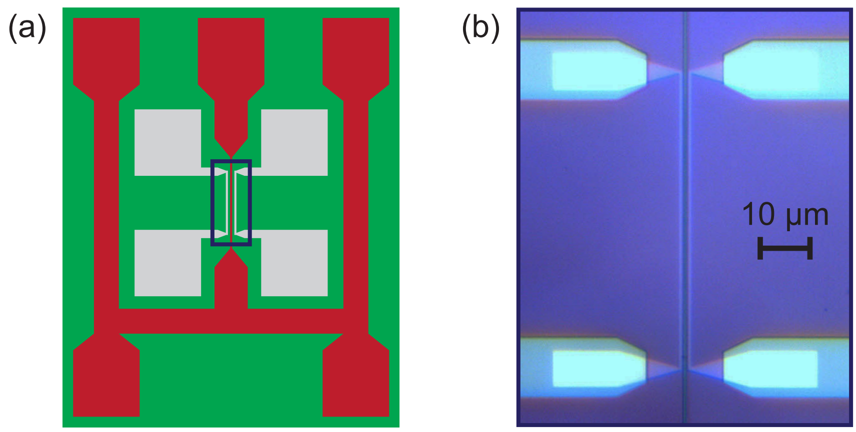

Figure 3.6: (a) Schematic drawing of the entire structure measured in this thesis including the bonding pads (**not** to scale). (b) Microscope image of the center (indicated by the blue rectangle) for better visibility. The thick horizontal strips on the left and right are the leads to the Pt strips, which themselves are vertical in this image. The microstrip antenna can be seen as the vertical strip in between the two Pt strips.

preamplifier was operated in DC coupling mode due to the very low frequency of the AC current. A 30 Hz low pass filtering was further introduced to suppress higher harmonics and possible perturbations created by the 50 Hz line frequency.

A Zurich Instruments HF2LI lock-in amplifier was plugged into the 50 Ω output of the preamplifier. Its clock is synced with the AC current source. Thus, it measures the first and second harmonic voltages $V_{\mathrm{det}}^{1\omega}$ and $V_{\mathrm{det}}^{2\omega}$ at the detector strip, which correspond to magnon transport induced at the injector via SHE and Joule heating effects, respectively (see Section 2.7). The 600 Ω output of the preamplifier was connected to a Keithley 2010 Mulitmeter, measuring the DC spin pumping voltage V_{sp} along the detector strip. The microwave current driven through the microstrip antenna was generated by a Rohde & Schwarz SMF 110A Signal Generator. All measurements were conducted in the ***CHAOS*** cryostat system at the WMI at a temperature of $T = 280\,\mathrm{K}$. Furthermore, we apply a static external magnetic field $\mathbf{H}_{\mathrm{ext}}$ in the film plane of the YIG and typically perpendicular to the strips. The detailed process of the magnon transport is again visualized in Fig. 3.7.

3.2.2 Lock-In Measurement Technique

A detailed explanation of the used lock-in AC measurement technique is given in the following. As mentioned before, a low frequency AC current $I_{\mathrm{inj}}(t) = I_{\mathrm{inj},0}\sin(\omega_{\mathrm{ac}}t)$ is applied at the injector. Consequently, the current at the detector strip created by magnon transport also oscillates with the same frequency $f_{\mathrm{ac}} = \omega_{\mathrm{ac}}/(2\pi)$. It is further subject to a phase shift Ψ. In total, the detector AC current can then be written as

$$I_{\mathrm{det}}(t) = I_{\mathrm{det},0}\sin(\omega_{\mathrm{ac}}t + \Psi)\,. \tag{3.8}$$

This results in a measured voltage at the detector of

$$V_{\mathrm{det}}(t) = R_1 I_{\mathrm{det}}(t) + R_2 I_{\mathrm{det}}^2(t) + \mathcal{O}\left(I_{\mathrm{det}}^3(t)\right), \tag{3.9}$$

which we approximated as a Taylor expansion until second order in $I_{\mathrm{det}}(t)$. R_1 and R_2 are coefficients characterizing the efficiency of the whole magnon transport.

$V_{\mathrm{det}}(t)$ is measured with a lock-in amplifier, meaning that the n-th harmonic voltage $V^{\mathrm{n}\omega}$ is detected. For each harmonic, this is done for two 90° phase-shifted channels X and Y. Mathematically, one can express this as first a multiplication of $V_{\mathrm{det}}(t)$ with $\sin(\omega_{\mathrm{ac}}t)$ for the X channel and $\cos(\omega_{\mathrm{ac}}t)$ for the y channel, and second

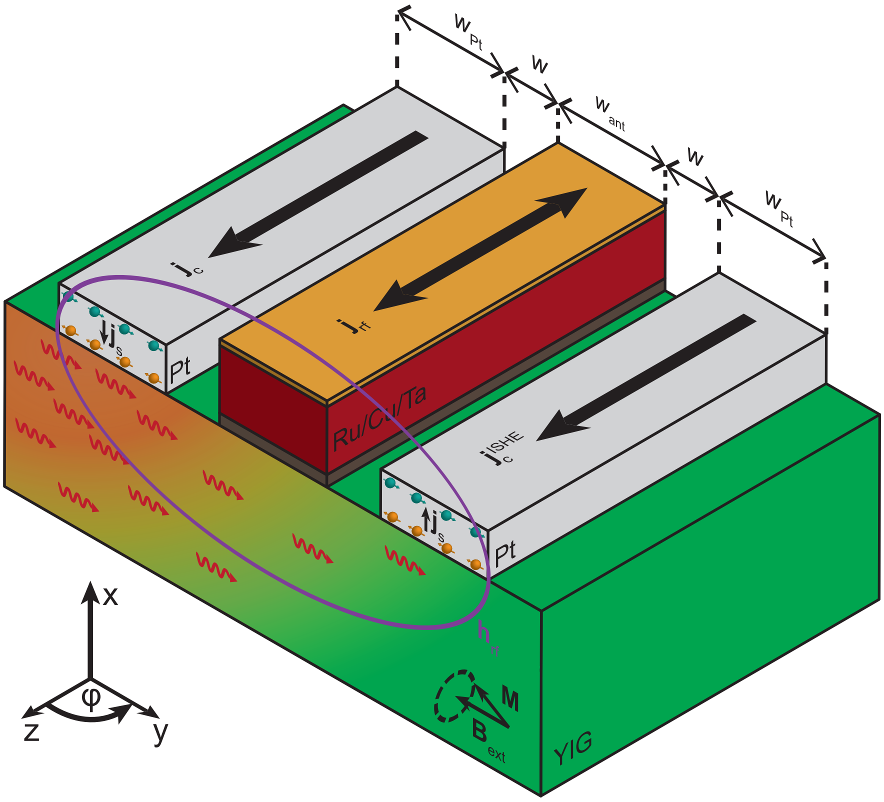

Figure 3.7: Side cut through the structure shown in Fig. 3.5. A charge current $\mathbf{j}_\mathrm{c}$ is applied at the upper Pt strip (injector), creating a spin current $\mathbf{j}_\mathrm{s}$ via the spin Hall effect. Via scattering at the Pt|YIG interface, magnons (red wiggly arrows) are injected into the YIG, where they diffuse in all directions. Some reach the lower Pt strip (detector), where the inverse process occurs, giving rise to a charge current $\mathbf{j}_\mathrm{c}^\mathrm{ISHE}$ that can be measured as an electrical voltage. The Ru|Cu|Ta microstrip antenna in the middle generates a microwave driving field $\mathbf{h}_\mathrm{rf}$ via the RF current $\mathbf{j}_\mathrm{rf}$. This is used to drive the magnetization $\mathbf{M}$ of the YIG film. $\mathbf{M}$ is aligned by an external magnetic field $\mathbf{B}_\mathrm{ext}$. Note that $\mathbf{h}_\mathrm{rf}$ has a relevant component parallel to $\mathbf{M}$ below the antenna as well as one perpendicular to $\mathbf{M}$ below the injector/detector. Consequently, both parallel and perpendicular pumping effects can occur.

an integration over a time interval T_{int}

$$V_{\text{X}}^{\text{n}\omega} = \frac{\sqrt{2}}{T_{\text{int}}} \int\limits_{t}^{t+T_{\text{int}}} \sin\left(n\omega_{\text{ac}} t'\right) V_{\text{det}}\left(t'\right)\, \text{d}t', \tag{3.10}$$

$$V_{\text{Y}}^{\text{n}\omega} = \frac{\sqrt{2}}{T_{\text{int}}} \int\limits_{t}^{t+T_{\text{int}}} \cos\left(n\omega_{\text{ac}} t'\right) V_{\text{det}}\left(t'\right)\, \text{d}t'. \tag{3.11}$$

We plug in the expressions for $V_{\text{det}}\left(t\right)$ and $I_{\text{det}}\left(t\right)$ given in Eqs. (3.8) and (3.9), and solve the integrals to obtain the first and second harmonic voltages

$$V_{\text{X}}^{1\omega} = \frac{1}{\sqrt{2}} I_{\text{det},0} R_1 \cos\Psi, \qquad V_{\text{X}}^{2\omega} = \frac{1}{2\sqrt{2}} I_{\text{det},0}^2 R_2 \sin 2\Psi, \tag{3.12}$$

$$V_{\text{Y}}^{1\omega} = \frac{1}{\sqrt{2}} I_{\text{det},0} R_1 \sin\Psi, \qquad V_{\text{Y}}^{2\omega} = -\frac{1}{2\sqrt{2}} I_{\text{det},0}^2 R_2 \cos 2\Psi. \tag{3.13}$$

Due to the finite phase shift Ψ observed in the experiments, the total signal amplitude is spread across the X and Y channel of the lock-in amplifier. Since one wants to measure the full signal amplitude and **not** some arbitrary fraction of it, one needs to further rearrange those voltages. This is done via a simple rotation matrix

$$\begin{pmatrix} V_{\text{X}'}^{\text{n}\omega} \\ V_{\text{Y}'}^{\text{n}\omega} \end{pmatrix} = \begin{pmatrix} \cos n\Psi & \sin n\Psi \\ -\sin n\Psi & \cos n\Psi \end{pmatrix} \begin{pmatrix} V_{\text{X}}^{\text{n}\omega} \\ V_{\text{Y}}^{\text{n}\omega} \end{pmatrix}. \tag{3.14}$$

The angle Ψ is determined iteratively via trial and error of various different values until there is no signal amplitude left in either one of the two channels. Consequently, by applying Eq. (3.14) to Eqs. (3.12) and (3.13), the full amplitude of the first harmonic is rotated into the X channel and the one of the second harmonic into the Y channel

$$V_{\text{X}'}^{1\omega} = \frac{1}{\sqrt{2}} I_{\text{det},0} R_1, \qquad V_{\text{X}'}^{2\omega} = 0, \tag{3.15}$$

$$V_{\text{Y}'}^{1\omega} = 0, \qquad V_{\text{Y}'}^{2\omega} = -\frac{1}{2\sqrt{2}} I_{\text{det},0}^2 R_2. \tag{3.16}$$

The origin of the phase shift Ψ is not entirely clear. There are various different possibilities. For example, even though the clocks of the AC current source and the lock-in amplifier are synced, the devices could have different trigger conditions. Also, the preamplifier or the magnon transport could give rise to a phase shift. Because we can correct for the phase shift as described above, a detailed analysis of the origin is not required for the scope of this thesis.

3.3 Spin Pumping Measurements

In this section, the DC spin pumping voltage is investigated first around FMR and second in the parametric pumping regime. For both cases, its frequency and power dependence is studied and discussed. We use the experimental setup and parameters given in Section 3.2.1, but for now we only consider the DC voltage measured by the multimeter.

3.3.1 Frequency Dependence of FMR

For all measurements presented in Chapter 3, the spin pumping and transport voltages were measured in parallel and simultaneously. The contribution of the magnon transport induced voltage to the spin pumping voltage V_{sp} can be neglected though because the amplitude of the transport induced voltage is negligibly small compared to the spin pumping voltage and even falls below the noise floor of the multimeter.

We start off by considering the frequency dependence of the FMR signature in the spin pumping voltage. For this, a microwave current of constant power $P_{\mathrm{rf}} = 5\,\mathrm{dBm}$ and frequency f_{rf} is driven through the microstrip antenna. The external magnetic field is applied in a fixed direction perpendicular to the Pt strips ($\varphi = 90°$). Its amplitude is varied from large positive values to zero and then from large negative values (corresponding to $\varphi = 270°$) to zero. This measurement protocol is repeated for various different RF frequencies. The acquired data is plotted in Fig. 3.8. Since there is some trapped flux present in the superconduction coils of the magnet cryostat, and the amplitude of the field is determined from the amplitude of the current flowing through the coils that create the field, this gives rise to a systematic error of the order of a few milli-Tesla in the measured field amplitude. Unfortunately, this can **not** be corrected with the measurement scheme described above.

By changing the magnitude of the external magnetic field, we vary the precession frequency of the magnetization until, at a given field, it matches the frequency of the applied RF driving field and the FMR condition is fulfilled. There, the magnetization absorbs energy from the driving field and is deflected from its equilibrium position, which we can measure as an increase in the spin pumping voltage as discussed in Section 2.6. In the linear driving regime, a Lorentzian lineshape is expected for this so-called FMR peak, which we also observe in the experiment. For lower RF driving frequencies as e.g. 4 GHz, which is shown in the inset on the upper left of Fig. 3.8, we observe a splitting of the FMR peak into two. They are separated from each other by an increasing field difference as the RF driving frequency decreases. This can be explained by a splitting of the ferromagnetic resonance into two different modes, which is also observed for other YIG films fabricated via PLD at the WMI. For $f_{\mathrm{rf}} \geq 10\,\mathrm{GHz}$, the different FMR modes can no longer be discerned. This makes it difficult to analyse the lineshape for lower frequencies, which is the main reason

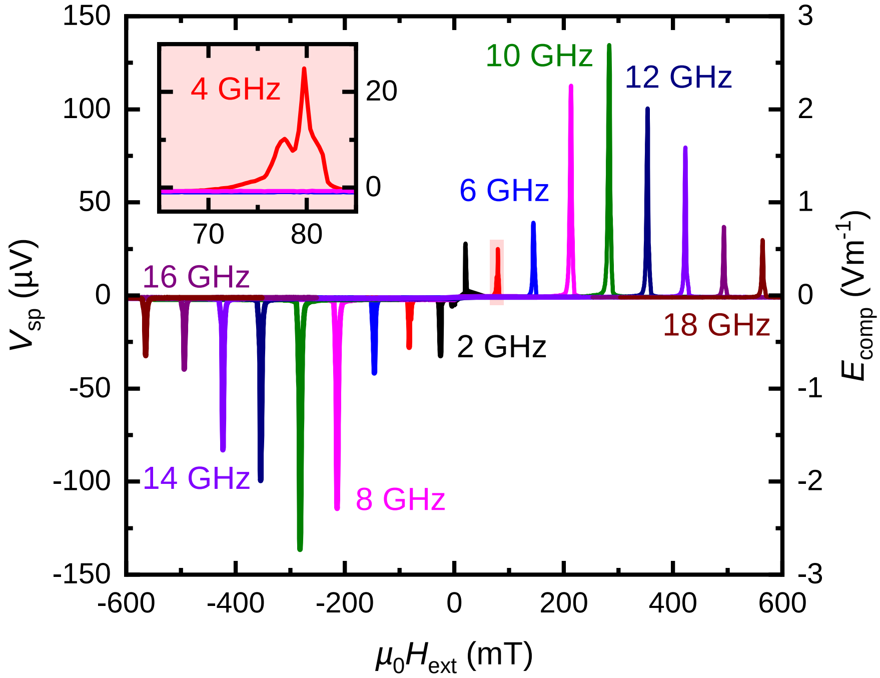

Figure 3.8: Magnetic field $\mu_0 H_{\mathrm{ext}}$ dependence of the spin pumping voltage V_{sp} for a constant RF driving power of 5 dBm, but various different frequencies which are color coded. The right y-axis shows the compensating electrical field E_{comp} in the Pt strip, which is equal to the spin pumping voltage normalized on the Pt strip length. The inset on the upper left displays a zoom on the FMR peak for an RF driving frequency of 4 GHz.

why we will later use only higher frequencies for a detailed analysis. Note that the used RF driving power of 5 dBm is already on the verge of the nonlinear/power broadening regime according to the quick estimate given in Section 3.1.2.

Another characteristic feature of FMR spin pumping is the inversion of the sign of the spin pumping voltage for an inverted external magnetic field direction (negative field amplitude), because this inverts the direction of the magnetization of the YIG film and thus also the spin polarization of the magnons injected into the platinum. Eventually, this results in an inverse direction of the inverse spin Hall effect induced charge current and compensating electrical field (see Section 2.6). Hence, the spin pumping voltage is of negative sign.

For each RF frequency, a Lorentzian of the following form is fitted to both FMR peaks at negative and positive fields

$$V_{\rm sp}\left[\mu_0 H_{\rm ext}\right] = V_{\rm sp,0} + \frac{A_0}{\pi}\frac{\mu_0\Delta H}{\left(\mu_0 H_{\rm ext} - \mu_0 H_{\rm res}\right)^2 + \mu_0^2\Delta H^2}, \tag{3.17}$$

$$A_{\rm sp} = \frac{A_0}{\pi\mu_0\Delta H}, \tag{3.18}$$

$$\mu_0\Delta H_{\rm FMR} = 2\mu_0\Delta H, \tag{3.19}$$

where $A_{\rm sp}$ is the amplitude of the peak and A_0, ΔH, $V_{\rm sp,0}$ and $H_{\rm res}$ are the fit parameters. We then average between the fit parameters obtained for positive and negative fields. From this, the linewidth $\mu_0\Delta H_{\rm FMR}$ and resonance field $\mu_0 H_{\rm res}$ of the FMR peak is extracted. This is repeated for an RF driving power of 15 dBm using a slightly modified measurement scheme, where the field is swept from high positive amplitudes to zero and from zero to high negative amplitudes, so that averaging between the positive and negative values also corrects for the trapped flux in the system. Figure 3.9 depicts for both RF powers the frequency dependence of (a) the resonance field and (b) the linewidth.

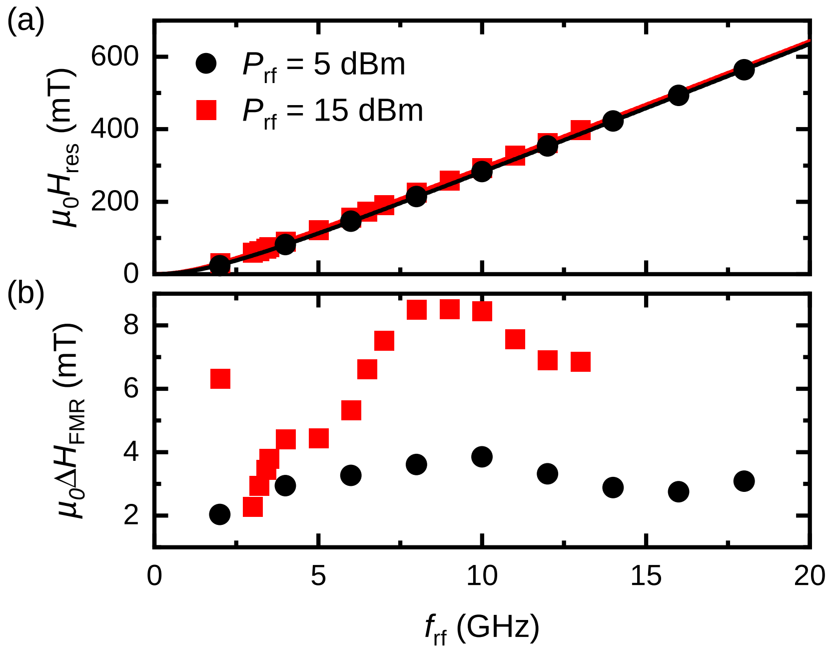

Figure 3.9: (a) Resonant external magnetic field $\mu_0 H_{\rm res}$ and (b) linewidth $\mu_0\Delta H_{\rm FWHM}$ of the FMR peak as a function of the RF driving frequency $f_{\rm rf}$. Both are depicted for an RF power of 5 dBm in black circles and 15 dBm in red squares.

As discussed in Section 2.4, the frequency dependence of the resonant magnetic field is fitted with Eq. (2.25), which describes the Kittel FMR mode for an in-plane magnetized thin film, to extract the g-factor g_e and the effective magnetization M_{eff}. The obtained values are summarized in Table 3.1. They are in good agreement with results reported in literature [Sun+12; Alt+13; Wim+19] and the bulk value of $\mu_0 M_s = 178\,\mathrm{mT}$ for the saturation magnetization of YIG [HRT74].

P_{rf} [dBm]	g_e	$\mu_0 M_{eff}$ [mT]
0	1.993 ± 0.016	163 ± 20
5	1.993 ± 0.008	173 ± 4
15	2.026 ± 0.004	131 ± 2

Table 3.1: Values of the fit parameters of Eq. (2.25). For an RF driving frequency of 5 dBm and 15 dBm, the spin pumping data was fitted. The values for 0 dBm are obtained from a reflectometry measurement.

In Fig. 3.9 (a), we see a clear shift of the resonance field curve to larger magnetic fields for the higher driving power of 15 dBm. This can be explained either by a heating of the sample due to the high amplitude of the RF driving current flowing through the microstrip antenna, which introduces thermal magnetic excitations into the YIG and thus reduces the saturation magnetization, or by a wide opening of the precession cone angle, which likewise reduces the saturation magnetization. Both scenarios lead to the decrease of the effective magnetization with the higher driving power visible in Table 3.1.

As discussed in Section 2.4, we expect a linear increase of the linewidth with the driving frequency for a Gilbert damping mechanism. This is **not** the case in the experimental data shown in Fig. 3.9 (b), and thus the data was **not** fitted with Eq. (2.27). The deviation can be explained by the complicated splitting of the FMR into two modes for low frequencies, which is nonetheless fitted with the simple Lorentzian lineshape given by Eq. (3.17). This is far from perfect and results in an unclear convergence of the fit, which contains only one of the two peaks for some RF frequencies or spans over both of them for others, depending on the initial conditions of the fit and the spacing of the peaks. This renders it impossible to make any credible statements about the frequency dependence of the linewidth. But even with this limitation, a strong increase is clearly visible when comparing the high to the low driving power, which is the main aspect to take away from this paragraph.

The frequency dependence of the amplitude A_{sp} of the FMR peak is **not** analyzed further here. In general, the dependence is **not** trivial, as it may contain non-linear phenomena in certain frequency ranges [Cas+12]. In a simple picture, one would expect a linear decrease of the spin pumping voltage with the RF driving frequency [Har+11; Cas+12]. This is **not** observed in the experiment, where we instead see a more or less constant amplitude level for $2\,\mathrm{GHz} \leq f_{rf} \leq 6\,\mathrm{GHz}$, then a large sudden increase until the maximum is reached for 10 GHz. After that, a steady decrease is visible. This deviation from the theoretical expectations can be explained by an imperfect and not optimized setup, i.e. no 50 Ω matching and no design optimization of the microstrip antenna, leading to relevant frequency-dependent losses of driving power. Therefore, and because this is not of importance in the experiments, it is not analyzed further in the scope of this thesis.

3.3.2 Power Dependence of FMR

In this section, the power dependence of the FMR signature in the spin pumping voltage is discussed. The measurement protocol stays similar to the one used before in Section 3.3.1. We again apply the external magnetic field in a fixed direction perpendicular to the Pt strips and sweep its amplitude from large positive over zero to large negative values. We repeat those sweeps for several different RF driving powers while keeping the frequency fixed. Figure 3.10 depicts the spin pumping voltage around ferromagnetic resonance for an RF driving frequency of 6 GHz on the left and 14 GHz on the right.

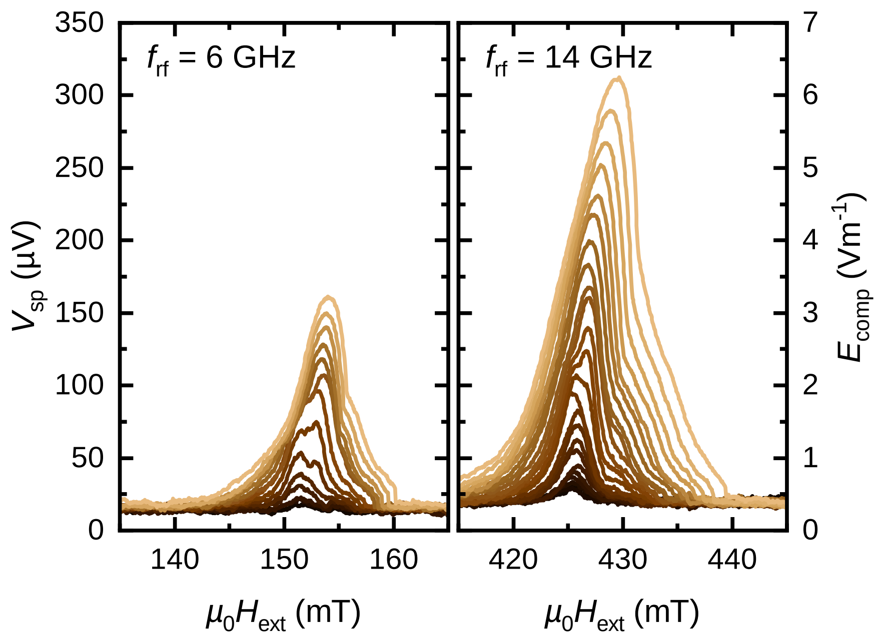

Figure 3.10: Spin pumping voltage V_{sp} as a function of the external magnetic field $\mu_0 H_{ext}$ for an RF driving frequency of 6 GHz on the left and 14 GHz on the right. For both frequencies, different RF driving powers are shown ranging from −5 dBm in black to 15 dBm for 6 GHz and 18 dBm for 14 GHz RF driving frequency in light orange. The right y-axis again shows the compensating electrical field E_{comp}.

The data for 14 GHz was measured in two different sets. Due to an imperfect alignment of the sample, there is a noticeable shift in both the baseline of the spin pumping voltage and the resonance field of FMR between those two sets. This shift is corrected in Fig. 3.10 by adding an arbitrarily chosen constant to both the baseline and the field of the second measurement series so that it fits the first, making it unreasonable to compare the resonance fields between the two sets. However, this correction does **not** affect a detailed analysis of the linewidth and amplitude of the FMR peak.

Figure 3.10 shows a clear increase of the amplitude of the FMR peak with increasing driving powers for both frequencies. The linewidth initially remains at a constant level, but increases continuously once a certain power has been exceeded. Furthermore, the resonance field shifts towards higher fields for higher driving powers, corresponding to a blue-shift of the precession frequency of the magnetization. In addition, a deformation of the line shape can be seen, which manifests itself in a low slope on the low-field side and a steep slope on the high-field side of the resonance. These effects are also observed in various other works [Igu+12; Lus+15; Bau+15; Dus+19] and several explanations have been put forward.

One possible explanation for the shoulder on the high-field side is an effect first reported by Cheng *et al.* [Che+20], who called it *"nonlocal" spin pumping*. By this they actually refer to a spin pumping voltage created by magnons excited somewhere in the YIG away but **not** under the Pt strip, which transfer their angular momentum into the YIG under the stip and thus generate a magnetization precession there as well. We call this effect ***propagating magnon induced spin pumping***. In general, the FMR resonance field/frequency changes when a Pt thin film is deposited on top of the YIG, so that two distinct peaks are expected in the voltage, one for the local and one for the propagating magnon induced spin pumping [Che+20]. This makes it possible to differentiate between the two contributions. Whether the propagating magnon induced or local spin pumping voltage dominates is mainly determined by the width of the Pt film. If it is very slim, like the Pt strips in this thesis, an extreme dominance of the propagating magnons is to be expected [Che+20]. Consequently, one would assign the main resonance to the propagating magnon induced signal and the deformation on the high-field side to the local signal. This would mean in contradiction to Cheng *et al.* [Che+20] a slightly higher ferromagnetic resonance frequency of the YIG|Pt bilayer compared to the bare YIG. In this case, the most likely location for the generation of the propagating magnons would be next to the three-strip structure (i.e. in Figs. 3.5 and 3.7 towards the right of the detector strip). However, there is a second conceivable scenario, where the main peak is created by both magnons excited locally below the detector strip and propagating magnons stemming from below the injector strip, while the high-field part is generated by the resonance of propagating magnons from the bare YIG next to the detector strip, whose signal is not as strong as expected because they are excited further away from the microstrip antenna and thus with a lower driving field amplitude. Following this, a direct comparison in this regard is difficult due to the complexity of our sample layout. For low RF driving powers, the amplitude of the local spin pumping is very small/below the noise level and only the propagating magnon induced contribution is visible. As the driving power increases the local voltage steadily increases as well until it exceeds the noise level at some point. Due to the close proximity of both peaks in terms of resonance field and frequency, they can not be differentiated. Instead, they appear together in from of a seemingly deformed lineshape.

Other theoretically conceivable explanations for both the resonance field shift and the linewidth distortion, besides the propagating magnon induced spin pumping, are either (i) nonlinear processes by which the resonant frequency itself becomes power dependent, (ii) a heating of the YIG at high powers that reduces the saturation magnetization, or (iii) a wide opening of the precession cone angle that likewise reduces the magnitude of the static magnetization component [Lus+15]. A systematic discussion of these effects in Lustikova *et al.* [Lus+15] deduces, among other things, that for both (ii) and (iii) hysteretic effects should appear quickly in the spin pumping voltage. Since this is not the case for their data, they conclude in agreement with [Bau+15] that (i) nonlinear processes such as the second order Suhl instability (see Section 3.1.2) must play a major role by transferring energy from the uniform precession into the spin wave spectrum [Lus+15]. Since we observe the same in Fig. 3.10, we conclude that we have strong evidence that the region of nonlinear FMR was indeed reached in our experiments.

The data obtained for 6 GHz suffers again from the mode splitting of the FMR which was already discussed in Section 3.3.1. This is particularly striking in the medium power range, where one can clearly see two distinguishable peaks, which begin to overlap as the linewidth increases for higher RF driving powers. Accordingly, we focus on the measurements for 14 GHz RF driving frequency in the upcoming quantitative analysis. For this, similar to before, a Lorentzian (as in Eq. (3.17)) is fitted to both the positive and negative field FMR peak for each RF driving power, from which the average amplitude A_{sp} and linewidth $\mu_0 \Delta H_{\mathrm{FMR}}$ is extracted. They are both plotted against the RF driving power in Fig. 3.11, where the (a) upper and (b) lower panel shows the linewidth and amplitude, respectively.

Figure 3.11 (a) quantitatively confirms the observation from before that the linewidth remains constant at about 3 mT up to a driving power of 5 dBm, and then increases sharply with some power law up to 8.2 mT for 18 dBm. As can be seen in Fig. 3.11 (b) and the inset, the amplitude of the FMR peak in the spin pumping voltage initially increases more or less linearly with power. Again at around 5 dBm driving power, a kink can be seen, after which the increase is reduced. This is referred to as the premature saturation of the main resonance and can be explained by the second order Suhl instability process (see Section 3.1.2) [An+04; Ols+07]. It was also observed by Zhou *et al.* [Zho+16], who found a linear power dependence of the cone angle

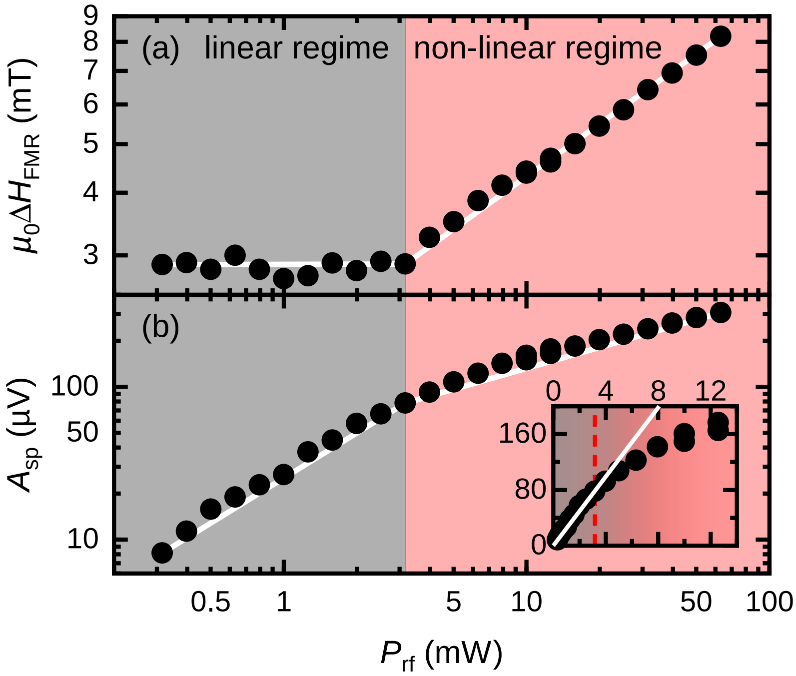

Figure 3.11: (a) Linewidth $\mu_0 \Delta H_{\mathrm{FMR}}$ and (b) amplitude A_{sp} of the FMR peak in the spin pumping voltage as a function of the RF driving power P_{rf} and for a frequency of 14 GHz in double logarithmic scale. The gray area marks the linear and the red area the nonlinear regime. The inset shows a zoom onto the lower powers of the spin pumping amplitude with linearly scaled axes. All white lines are introduced as guides to the eye.

squared in the linear and a dependence of θ^2 on $P_{\mathrm{rf}}^{1/3}$ in the nonlinear regime. As further investigated in [Zho+16], this can **not** be due to a non-linearity of the spin pumping process itself, as the spin pumping voltage is linearly proportional to $\sin^2 \theta$ for all powers (and thus follows Eq. (2.45) of Section 2.6) [Cze+11; Zho+16]. In addition, the kink appears suddenly after 5 dBm driving power is exceeded and thus exhibits the characteristic threshold behavior of the second order Suhl instability.

If only an increase of the linewidth were to be seen, this could also be explained by a power broadening effect. However, since additionally a strong drop of the amplitude increase, a deformation of the lineshape and, as shown in the next Section 3.3.3, parametric pumping effects are observed, higher order processes (see Section 3.1.2) must inevitably play an essential role. In conclusion and in agreement with literature [An+04; Ols+07; Bau+15; Zho+16], this indicates the achievement of a nonlinear regime of ferromagnetic resonance.

3.3.3 Parametric Pumping

We now turn our focus away from the field region of ferromagnetic resonance and expand it on the whole field range. The measurement scheme remains equivalent to Section 3.3.2, but this time only an RF driving frequency of 6 GHz is considered. Figure 3.12 shows in (a) the entire measured field range and focuses in (b) on the region of low external magnetic fields. Similar to before, the field sweep was repeated for several RF driving powers ranging from −5 dBm in dark brown to 15 dBm in light orange. In fact, those are the same measurements that were already shown in the left panel of Fig. 3.10, in which they were focused on the FMR.

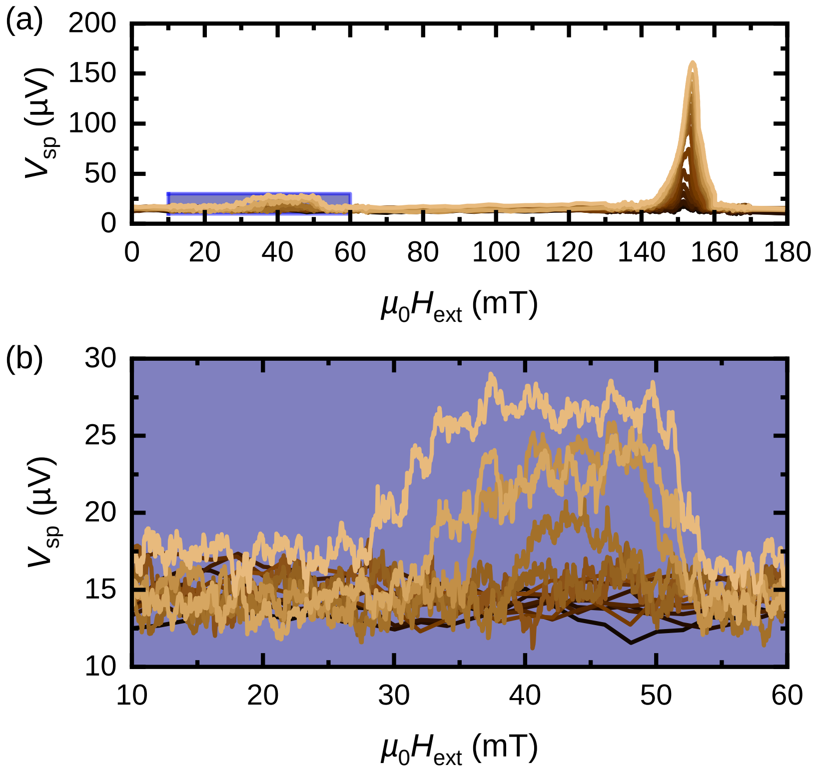

Figure 3.12: Spin pumping voltage V_{sp} as a function of the external magnetic field $\mu_0 H_{ext}$ for increasing RF powers P_{rf} (color coded with dark brown for low powers and bright orange for high powers) but with the same RF frequency of 6 GHz.

In Fig. 3.12 (a) one can, besides the FMR signature around 150 mT, see the formation of a secondary resonance at lower magnetic fields from around 30 mT to 50 mT. It can be identified as the subsidiary resonance created by the parametric pumping effects discussed in Section 3.1.2 and is much wider and lower in amplitude compared to the FMR peak. In addition, the lineshape of the peak is **not** Lorentzian at all, but rather has some undefined rectangle-like shape. Figure 3.12 (b) displays the subsidiary resonance in greater detail. One can now see that it first appears for an RF driving power of 12 dBm and continuously grows in width and amplitude for higher powers. This threshold behavior is characteristic for parametric effects (see Section 3.1.2). Interestingly, the observed threshold power of 12 dBm is much higher than that of the linewidth broadening discussed previously in Section 3.3.2. This is consistent with theoretical expectations, since the second order Suhl instability causes the linewidth broadening and its critical field is much smaller than that of the first order Suhl or parallel pumping instability that create the subsidiary resonance [RA90]. Transforming the experimentally observed threshold driving powers of 5 dBm and 12 dBm into RF field amplitudes via the Karlqvist equations (see Section 2.3), we obtain for the out-of-plane field $\mu_0 h_{\mathrm{rf,oop}}$ below the middle of the detector strip ($x = 0\,\mathrm{m}$ and $y = 750\,\mathrm{nm}$) and the in-plane field $\mu_0 h_{\mathrm{rf,ip}}$ below the microstrip antenna ($x = 5\,\mathrm{nm}$ and $y = 0\,\mathrm{m}$)

$$\mu_0 h_{\mathrm{rf,oop}}\,[5\,\mathrm{dBm}] = 2.0\,\mathrm{mT}, \tag{3.20}$$

$$\mu_0 h_{\mathrm{rf,ip}}\,[5\,\mathrm{dBm}] = 8.8\,\mathrm{mT}, \tag{3.21}$$

$$\mu_0 h_{\mathrm{rf,oop}}\,[12\,\mathrm{dBm}] = 4.4\,\mathrm{mT}, \tag{3.22}$$

$$\mu_0 h_{\mathrm{rf,ip}}\,[12\,\mathrm{dBm}] = 19.8\,\mathrm{mT}, \tag{3.23}$$

where we used the geometric dimension of the sample given in Section 3.2.1 and assumed a power loss of 20% as well as an input impedance of $Z_0 = 50\,\Omega$. Those rough estimates further affirm the fact that there is about one order of magnitude difference in the amplitude of the driving field between the broadening of the main resonance and the appearance of the subsidiary resonance.

Another striking feature is the fact that the high field end of the subsidiary resonance peak remains at a roughly constant field for all RF driving powers, while the lower field end expands steadily with increasing power. In analogy to the terminology already introduced in Section 3.1.1, the higher end of the parametric pumping peak is called **onset magnetic field** H_{onset}. There, we also predicted the extension of the lower field end, as magnons with larger wavevectors can be excited at lower fields for higher driving powers. The measured signature also shows a great resemblance to the prediction shown in Fig. 3.4 (a). We therefore conclude that it is indeed caused by these parametric processes.

Similar measurements were conducted by Ando *et al.* [AAS11], where they observed the same characteristics, i.e. the threshold behavior of the subsidiary resonance, its broadening towards lower field and its constant onset. They attribute their observations to a nonlinear coupling between the driving field and the magnetization dynamics. In their setup, the RF driving field was applied exclusively perpendicular to the external magnetic field. Thus, parallel pumping is prohibited and only the first and second order Suhl instabilities can be considered as the reason for their observations. They also conclude that perpendicular pumping effects occur at much lower RF driving field amplitudes compared to parallel pumping. For that reason, and because of the great similarities between Fig. 3.4 (a) and Fig. 3.12, one could argue that this conclusion also applies to our observations. However, in order to achieve certainty in this matter, further measurements are necessary in geometries that clearly exclude either parallel or perpendicular pumping.

Furthermore, similar effects are reported by An *et al.* [An+04] in permalloy, i.e. a different material system, where they likewise see a premature saturation of the main FMR peak and the appearance of a subsidiary resonance at lower external magnetic fields. They explicitly argue that all these signatures must clearly be symptoms of nonlinear spin wave processes because, first, premature saturation occurs at driving powers far below those for which classical power broadening would be expected, and second, the subsidiary resonance absolutely can **not** be explained without nonlinear processes such as parallel pumping or the first order Suhl instability. Moreover, both effects do **not** occur continuously but abruptly and thus show a clear threshold behavior [An+04]. Since all these arguments also apply to our measurements, we can finally and conclusively confirm that the nonlinear region has been reached.

Besides the power dependence of the parametric pumping instabilities, we can also analyze its frequency behavior. For this reason, we consider another measurement series where the RF driving power is fixed at 15 dBm, which is well above the observed threshold, and field-sweeps are recorded for different RF driving frequencies between 2 GHz and 13 GHz and plotted in Fig. 3.13.

There, similar to before in Fig. 3.8, one can clearly see the FMR peaks. In addition, a subsidiary resonance is visible for some RF frequencies. Similar to the FMR peak, there is a frequency dependence of the amplitude of the subsidiary resonance peak, which reaches its highest amplitude for 4 GHz to 6 GHz driving frequency. For higher frequencies, the amplitude is much smaller. At frequencies greater than or equal to 12 GHz, the subsidiary resonance is not visible or its amplitude falls below the noise level. The inverted sign for negative magnetic fields further confirms the spin pumping origin of the signal. Based on this, the RF driving frequency of 6 GHz was chosen for the power dependent analysis discussed earlier, as it is the highest frequency (and thus the least influenced by the mode splitting for the FMR) that still holds a significant amplitude.

For the RF driving frequencies 2 GHz and 3 GHz, the subsidiary resonance is no longer separated from the FMR, but instead both peaks overlap. For YIG films, this overlap of the subsidiary resonance and the FMR typically occurs for RF driving frequencies below 3.28 GHz [Cro+91]. In our case, this results in a broadening of the lineshape, which is best visible for 2 GHz in the inset of Fig. 3.13. There, the higher field end of the peak still has the basic Lorentzian lineshape of the FMR peak. Contrary, the peak extends far at the lower field end in the typical manner shown

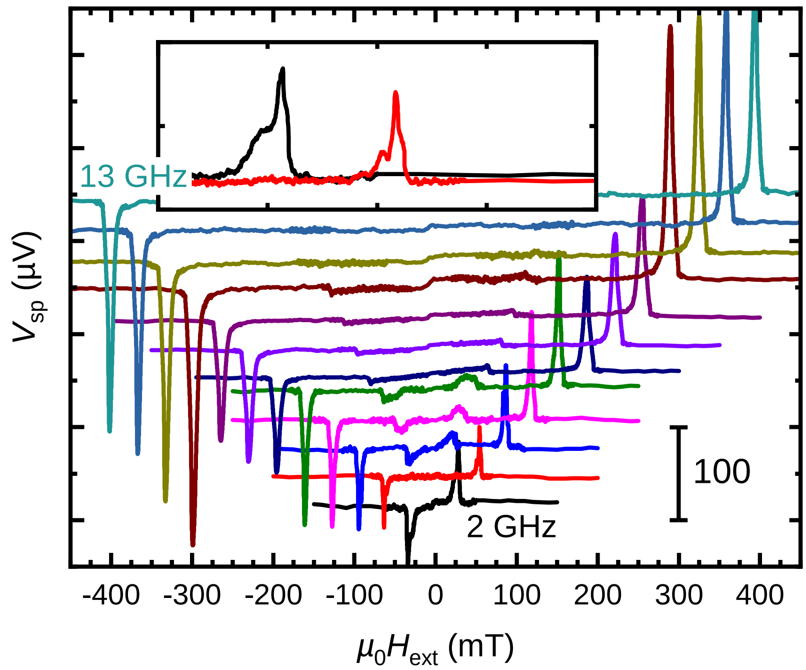

Figure 3.13: Field-sweeps of the spin pumping voltage V_{sp} for a fixed RF driving power of 15 dBm and various frequencies from 2 GHz in black to 13 GHz in cyan in steps of 1 GHz. In order to achieve better visibility, an offset is introduced between the field-sweep of each frequency. The inset shows a zoom on the peak for 2 GHz and 3 GHz driving frequency, in which the ticks on the x- and y-axis are kept at the same distance.

in Fig. 3.12. This effect was first observed in the late 1950s by several independent groups [LSP58; SLP58; Ros60]. It can be explained by an actual overlap of the resonance condition of the first order Suhl instability and the FMR [CP].

As already discussed in Section 3.3.1, an analysis of the frequency dependence of the amplitude is not reasonable and thus omitted in this thesis. Instead, we extract the onset field of the parametric pumping peak for each frequency and fit it with Eq. (3.3) (see Section 3.1.1 for the derivation). The error stemming from the trapped flux in the magnet coils is again reduced by averaging between negative and positive fields. Figure 3.14 shows both the experimental data (filled circles) and the theory fit (gray line).

Similar to our previous analysis in Section 3.3.1, the effective g-factor and the effective magnetization are obtained from the fit:

$$g_e = 1.99 \pm 0.07, \tag{3.24}$$

$$\mu_0 M_{\text{eff}} = (150 \pm 20)\,\text{mT}. \tag{3.25}$$

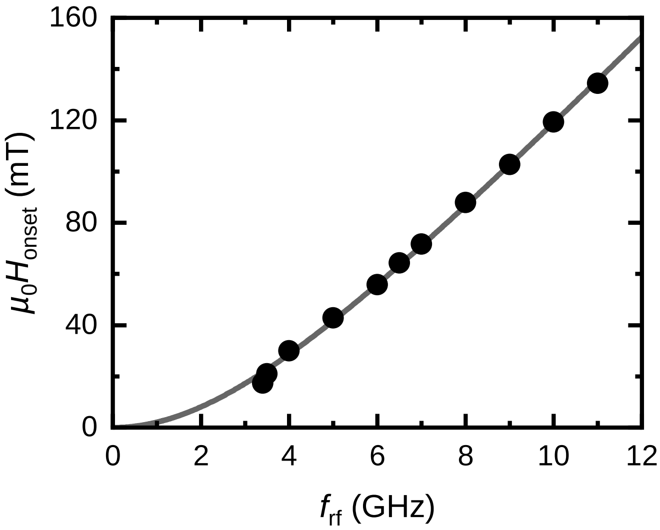

Figure 3.14: Frequency dependence of the onset field $\mu_0 H_{\mathrm{onset}}$ of the parametric pumping peak for an RF power of 15 dBm. The data is fitted with Eq. (3.3) (gray line).

Comparing these values with those obtained before in Table 3.1, we find a perfect agreement. Especially, the reduction of the effective magnetization M_{eff} due to the microwave heating of the YIG is nicely reflected here as well.

3.4 All-Electrical Magnon Transport Experiments

In this section, magnon transport effects are discussed. We start off by characterizing the transport amplitude with well established angle dependent magnon transport measurements. After that, an RF driving field is introduced, and its influence on the magnon transport around ferromagnetic resonance is investigated and compared to the results obtained by Liu *et al.* [Liu+19]. Finally, the existence and origin of possible measurement artifacts in the transport voltages is analyzed.

3.4.1 Transport Characterization

First, the magnitude of the magnon transport in our sample is characterized using the all-electrical magnon transport measurement technique. In these measurements, **no** microwave current is applied to the microstrip antenna and consequently also **no** RF driving field. A static external magnetic field of fixed magnitude $\mu_0 H_{\mathrm{ext}} = 50\,\mathrm{mT}$ is applied in the film plane of the YIG. This is sufficient to fully magnetize the YIG along its direction. The magnetic field direction is turned around the x-axis (variation of φ, see Figs. 3.5 and 3.7) and we measure the first and second harmonic voltage in steps of 5° of φ at the detector strip via the lock-in measurement technique (see Section 3.2.2). The result is plotted in Fig. 3.15, where one can see the first and second harmonic voltage in the upper and lower panel, respectively. A voltage offset and an imperfect angle alignment of the sample are already corrected.

We also connected the first harmonic to the SHE transport voltage and the second harmonic to the Joule heating transport voltage

$$V_{\mathrm{det}}^{1\omega} = V_{\mathrm{det}}^{\mathrm{SHE}} \propto \cos^2(\varphi)\,, \tag{3.26}$$

$$V_{\mathrm{det}}^{2\omega} = V_{\mathrm{det}}^{\mathrm{therm}} \propto \cos(\varphi)\,. \tag{3.27}$$

By applying an AC current to the injector Pt strip, the charge current and thus also the polarization direction of the SHE injected magnons varies periodically. Consequently, the created voltage at the detector is also subject to a variation with the same frequency as the injector charge current and is picked up in the first harmonic of the lock-in amplifier. For the Joule heating injection of magnons, only a heat gradient is necessary, which is independent of the charge current direction in the injector strip. The thermal injection of magnons instead varies with the absolute value of the charge current and thus at twice its frequency. Consequently, it is detected in the second harmonic signal of the lock-in amplifier.

As discussed in Section 2.7, we expect a dependence on the cosine squared of the angle φ for the SHE and a cosine dependence for the Joule heating transport voltage, which is also observed in Fig. 3.15 in the experiment. By changing φ, we vary the orientation between the magnetization $\mathbf{M}$ of the YIG and the polarization of the spin current $\mathbf{s}$. For $\varphi = 0°$ and $\varphi = 180°$, the magnetization is parallel to the z-axis

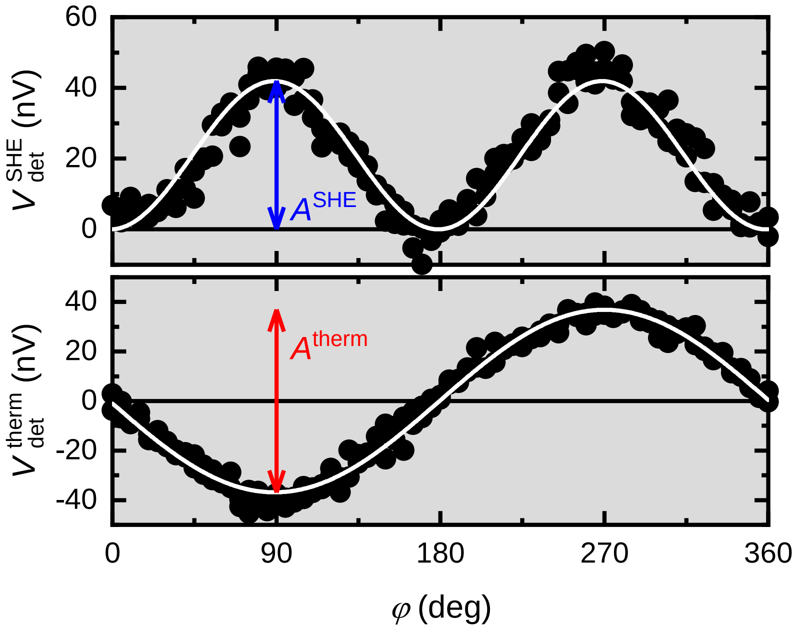

Figure 3.15: All-electrical magnon transport voltages in the absence of an RF driving field. For a constant external magnetic field amplitude of 50 mT, the field is rotated in plane by an angle φ with respect to the x-axis. The upper panel shows the first and the lower panel the second harmonic voltage, which are created from SHE and Joule heating induced magnon transport, respectively. The white line in the upper panel is a cosine squared fit to the data, while in the lower panel it is a cosine fit. Of these, the amplitudes A^{SHE} (in blue) and A^{therm} (in red) of the transport voltages are extracted.

and $\mathbf{M} \perp \mathbf{s}$. Consequently, and since both the SHE and the Joule heating induced magnons can only be detected via the ISHE, **no** magnons are detected at the Pt detector strip and thus $V_{\mathrm{det}} = 0$. For $\varphi = 90°$, the SHE transport voltage reaches its highest value as $\mathbf{M} \parallel \mathbf{s} \parallel \hat{\mathbf{e}}_{\mathrm{y}}$ and thus the SHE magnon injection and ISHE detection is maximal. Reversing the direction of $\mathbf{H}_{\mathrm{ext}}$ so that $\varphi = 270°$ and $\mathbf{M} \parallel \mathbf{s} \parallel -\hat{\mathbf{e}}_{\mathrm{y}}$ has no influence on the SHE transport voltage, but inverts the sign of the Joule heating transport voltage. This is because in the Joule heating case, only the detection process is dependent on the orientation of $\mathbf{m}$, whereas for the SHE contribution, both injection and detection depend on the orientation of $\mathbf{m}$ and thus the two minus signs cancel out.

The SHE and Joule heating induced magnon transport voltages are fitted with a cosine squared and cosine, respectively. From the amplitude of the fits, we obtain the amplitudes A^{SHE} and A^{therm} of the respective magnon transport voltage

$$A^{\mathrm{SHE}} = 42\,\mathrm{nV} \tag{3.28}$$

$$A^{\mathrm{therm}} = 74\,\mathrm{nV} \tag{3.29}$$

Similar samples fabricated and measured in the same way at the Walther-Meißner-Institute yielded significantly higher amplitudes. For example, Gückelhorn *et al.* [Güc+20] observed $A^{\mathrm{SHE}} \approx 0.4\,\mu\mathrm{V}$ and $A^{\mathrm{therm}} \approx 0.04\,\mu\mathrm{V}$ for half the injector current of this thesis ($I_{\mathrm{inj}} = 100\,\mu\mathrm{A}$), and Wimmer *et al.* [Wim+19] $A^{\mathrm{SHE}} \approx 0.25\,\mu\mathrm{V}$ and $A^{\mathrm{therm}} \approx 0.01\,\mu\mathrm{V}$ for an even lower injector current ($I_{\mathrm{inj}} = 50\,\mu\mathrm{A}$). From this, in a rough estimate, we would expect in our measurement about twice the transport amplitudes observed in Gückelhorn *et al.* [Güc+20]. This is not the case. Instead, the transport amplitudes observed in this thesis are at least an order of magnitude smaller compared to [Wim+19; Güc+20]. The reason for this suppression is most likely an absorption of magnons by the microstrip antenna in between the two Pt strips. Since the materials used for the antenna are conducting, spin transfer across its interface to the YIG film and the subsequent conversion into a charge current via the ISHE is possible. This corresponds to the formation of an addition loss channel for magnons, which reduces the amount of magnons reaching the detector Pt strip and consequently the amplitudes of the magnon transport voltages. A systematic study and discussion of this phenomenon can be found in [Kar21].

3.4.2 FMR Spin Transport

In this section, we discuss the influence of FMR on magnon transport. Therefore, an RF driving field with a frequency of 14 GHz is applied to the antenna structure. Similar to Section 3.3, an external magnetic field is applied perpendicular to the Pt strips ($\varphi = 90°$), so that both the spin pumping and transport voltages are maximal. Its amplitude is then swept from large positive values over zero to large negative values (corresponding to $\varphi = 270°$). The DC spin pumping voltage as well as the transport voltages are measured simultaneously. In fact, these are the very same measurements of which the spin pumping voltage was already shown and discussed before in Section 3.3.2. Assuming that there is no time variation of the DC spin pumping voltage with the lock-in frequency, the voltages measured by the lock-in amplifier are, in analogy to the last section, equal to the SHE and Joule heating induced magnon transport voltages. This is assumed for the discussion and comparison in this section. However, we assume that the voltages are dominated by measurement artifacts caused by a leakage of the spin pumping voltage into the lock-in detection. This is presented in more detail in the next Section 3.4.3 and the reason why we will, regarding our data, refrain from calling the first and second harmonic voltages SHE and Joule heating transport voltages in the following.

Figure 3.16 depicts the field dependence of the first and second harmonic voltage around ferromagnetic resonance for various different RF driving powers. Because the magnon transport is roughly constant with the field, every feature corresponds to a modulation of the harmonic voltages, while the baseline is given by the transport. Note that, as before in Fig. 3.10, the data was collected in two different measurement runs and consequently the second set of data had to be shifted by adding a constant

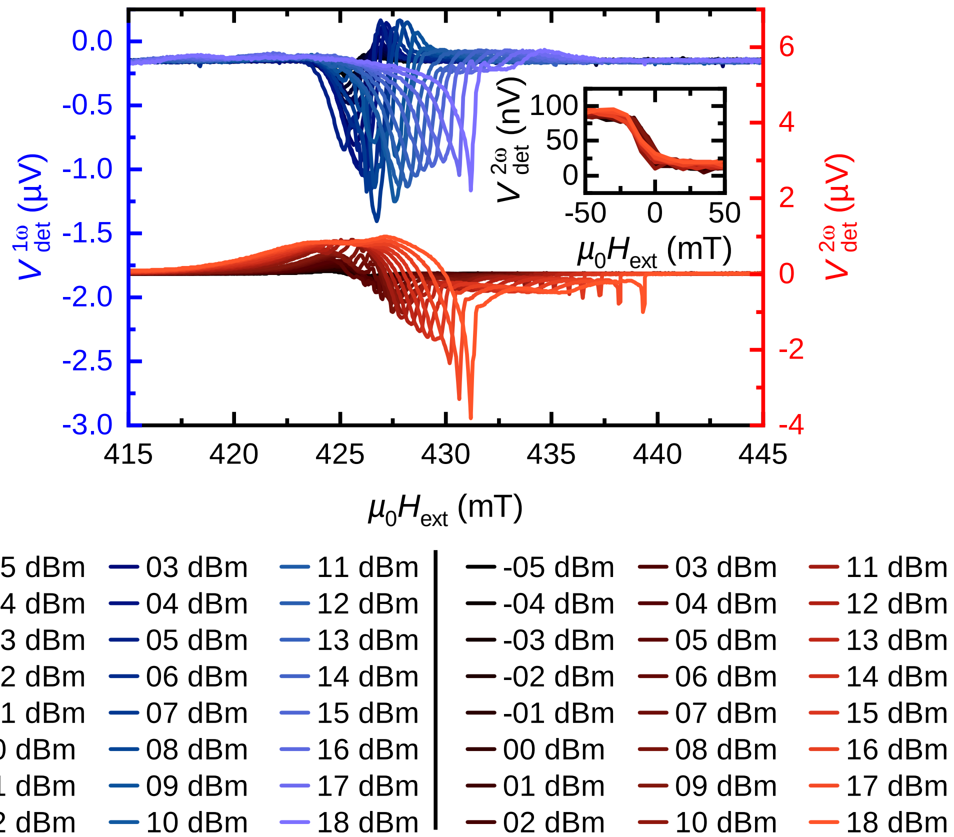

Figure 3.16: First and second harmonic voltages $V_{\mathrm{det}}^{1\omega}$ and $V_{\mathrm{det}}^{2\omega}$ of the lock-in detection as a function of the external magnetic field magnitude $\mu_0 H_{\mathrm{ext}}$ and for an RF driving frequency of 14 GHz and various powers given below. The inset shows a zoom on the second harmonic voltage around zero external magnetic field.

field and voltage offset in order to match the first data set.

For both harmonics, we observe a pronounced peak-dip-shape with about a few microvolt amplitude, which is approximately two orders of magnitude larger than the maximum magnon transport signals determined in the previous chapter (see Eqs. (3.28) and (3.29)). For the first harmonic voltage, a dip towards negative voltages can be observed at the lower field end, whose amplitude is larger than that of the peak at the higher field end. The dip towards negative voltages would correspond to a suppression of the magnon transport and the peak towards higher voltages to an enhancement. Since the amplitude of the dip is much larger than the basic transport amplitude, it would correspond not only to a suppression but to an inversion of the magnon transport signal. This is rather puzzling and unexpected, thus hinting towards the influence of measurement artifacts.

For the second harmonic voltage, a peak appears at the lower field end and a dip at the higher field end. Note that, in contrast to the first harmonic, for the second harmonic voltage and positive external magnetic fields, a peak corresponds to a suppression and a dip to an enhancement of the magnon transport. For higher powers, a second dip appears at the very end of the high field side. Similar to before, the amplitudes of both peak and dip are much larger than the baseline, which would again imply a transport modulation around two orders of magnitude larger than the basic amplitude and accordingly a signal inversion for the peak. Furthermore, the inset of Fig. 3.16 shows a sign switching at zero field, which is characteristic for Joule heating induced magnon transport. There, the magnetization direction and thus the polarization of thermally injected magnons is reversed by the external magnetic field, which changes the sign of the detector voltage, i.e. a change in Fig. 3.15 from $\varphi = 90°$ to $270°$. The amplitude of this voltage change is $74\,\mathrm{nV}$ and thereby consistent with the amplitude of the Joule heating induced magnon transport (given by Eq. (3.29) in Section 3.4.1).

Compared to the measurements conducted by Liu *et al.* [Liu+19], we observe a similar general shape. They also find the same peak-dip features in the first and second harmonic signals, but with much lower amplitudes. In their case, there is no inversion of the transport, but rather a strong suppression of the signal up to 95% of the baseline. Since the absolute signal amplitude is about one order of magnitude larger in our measurements, the lineshape of the features is much more clearly visible. Furthermore, Liu *et al.* observe an asymmetric peak at low powers, where there is a strong enhancement of the SHE induced transport only at a positive but not a negative external magnetic field lower than the FMR. They attribute this to a chiral nonreciprocal surface mode and report that the feature is much more pronounced for thicker films (they compare a 210 nm to a 100 nm thick film) due to the higher number of standing spin wave modes in thicker films. We do **not** detect this feature in our measurements because we use a much thinner film ($t_{\mathrm{YIG}} = 23\,\mathrm{nm}$) and therefore it should be strongly suppressed.

Nevertheless, a quantitative analysis similar to the one in Liu *et al.* [Liu+19] is attempted below. For this, the amplitude relative to the baseline and the field position of each peak/dip are manually determined. The former can be done for all measured powers, while the latter is done only for the powers measured in the first measurement run, since positions can not be compared quantitatively between the two data sets. Figure 3.17 shows the power dependence of both (a) amplitude and (b) resonance field of the peak and dip in the first harmonic voltage.

In Fig. 3.17 (a), a strong increase in the linear regime can be seen at first, which stagnates after reaching the nonlinear regime. There, the amplitude of the dip remains at a constant level, while that of the peak collapses and afterwards stays at a constant low level. This saturation effect was also reported by Liu *et al.* [Liu+19] and

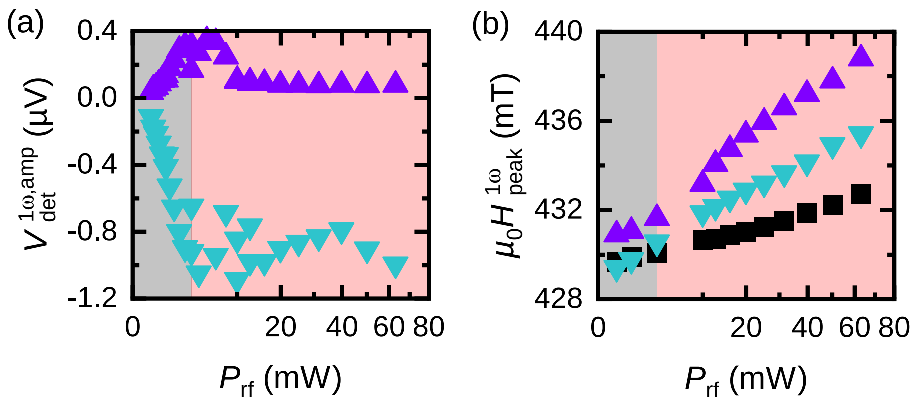

Figure 3.17: (a) Amplitude $V_{\mathrm{det}}^{1\omega,\mathrm{amp}}$ and (b) position $\mu_0 H_{\mathrm{peak}}^{1\omega}$ of the peak (purple up triangles) and the dip (blue down triangles) in the first harmonic voltage $V_{\mathrm{det}}^{1\omega}$. As a reference, the black squares in (b) depict the position of the peak in the DC spin pumping voltage. The x-axis is in square root scale and thus according to Section 2.3 linearly proportional to the RF driving field amplitude. The linear and nonlinear regions are indicated by a gray and red background, respectively, similar to Fig. 3.11.

is explained by strong scattering of the SHE induced magnons with magnons created via the second order Suhl instability process. They further report a field alignment of the (suppression) dip and ferromagnetic resonance, which, according to them, could be explained by a heating of the YIG due to the high microwave absorption at FMR, which reduces the effective magnetization and in the course of this also the magnon transport. Yet, they admit to not having full understanding and that this effect is not sufficient to explain such a strong suppression. For the linear regime, we can confirm this alignment with the data shown in Fig. 3.17 (b). In the nonlinear regime, however, FMR peak and transport dip start to drift apart. But this is most likely due to the fact, that the FMR resonance field is determined via a Lorentzian fitting, which can not account for the deformation of the lineshape and therefore does not reflect the actual maximum for highly nonlinear driving powers (see Fig. 3.10). The field position of the (enhancement) peak is, in agreement with Liu *et al.* [Liu+19], always at higher fields than the dip. In their work, they provide a conceivable explanation by identifying it as the external magnetic field where the RF driving frequency coincides with the minimum of the backward volume mode ($\omega_{\mathrm{rf}} = \omega\left(k_{\mathrm{min}}\right)$, see Section 3.1.1). Consequently, magnons are pumped into this minimum, which increases the magnon density and thus the overall magnon conductivity. The idea seems reasonable as a strong enhancement of the transport by an increase of magnon density is also reported in other works [Cor+18; Wim+19]. But since the minimum becomes much flatter for smaller film thicknesses, and in our case the difference to the FMR mode is only around 2 mT small, we can **not** clearly ascribe it to this effect.

In Fig. 3.18 (a), the power dependence of peak and dip amplitude is shown for the

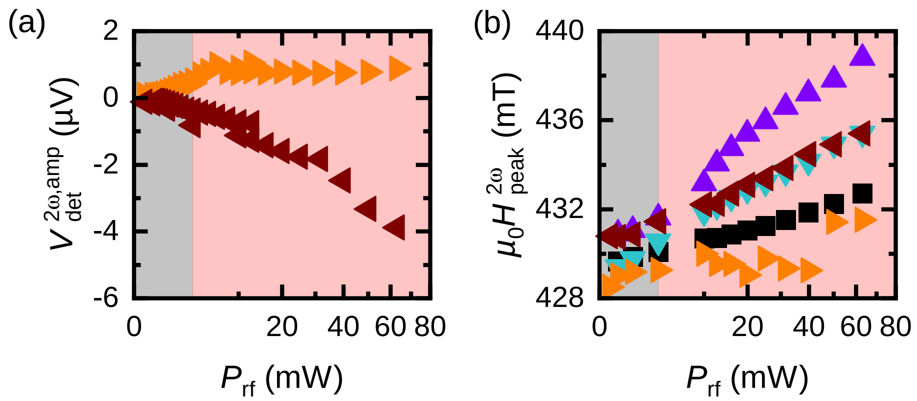

Figure 3.18: (a) Amplitude $V_{\rm det}^{2\omega,\rm amp}$ and (b) position $\mu_0 H_{\rm peak}^{2\omega}$ of the peak (orange right triangles) and the dip (red left triangles) in the second harmonic voltage $V_{\rm det}^{2\omega}$. As a reference, the black squares in (b) depict the position of the peak in the DC spin pumping voltage. The purple up and blue down triangles give the position of peak and dip, respectively, in the first harmonic signal.

second harmonic voltage. With increasing driving power, we observe a steady increase of the (enhancement) dip. In contrast, the (suppression) peak increases at first, but saturates quickly in the nonlinear regime. Similar to before, our power dependent observations are in good qualitative agreement with [Liu+19]. Figure 3.18 (b) depicts the position of peak and dip in the second and first harmonic voltage as well as the FMR peak in the DC spin pumping voltage. There, one can see that, for both harmonics, the transport suppression is always on the lower and the enhancement on the higher field end. In the linear regime, the suppression peak in the second harmonic coincides with the suppression dip in the first harmonic and the FMR. For higher powers, the alignment gets increasingly worse. This is mainly due to the very broad shape of the peak in $V_{\rm det}^{2\omega}$, which gives a big error/range for the position of the maximum. The enhancement dip in $V_{\rm det}^{2\omega}$ and peak in $V_{\rm det}^{1\omega}$ also lie on top of each other in the linear regime, but start to drift apart when the driving power is increased. All observations in the linear regime agree nicely with Liu *et al.* [Liu+19], where also suppression and enhancement coincide in the SHE and Joule heating induced magnon transport voltages.

3.4.3 Measurement Artifacts

At the start of the last Section 3.4.2 we already briefly mentioned possible measurement artifacts in the first and second harmonic voltage, as the modulation amplitudes are suspiciously large. This indicates that the spin pumping voltage is leaking into the lock-in detection technique. How this can be explained and how the mechanism behind it works is discussed in this section. For this purpose, the normalized spin pumping, first and second harmonic voltage are plotted in Fig. 3.19 around the FMR.

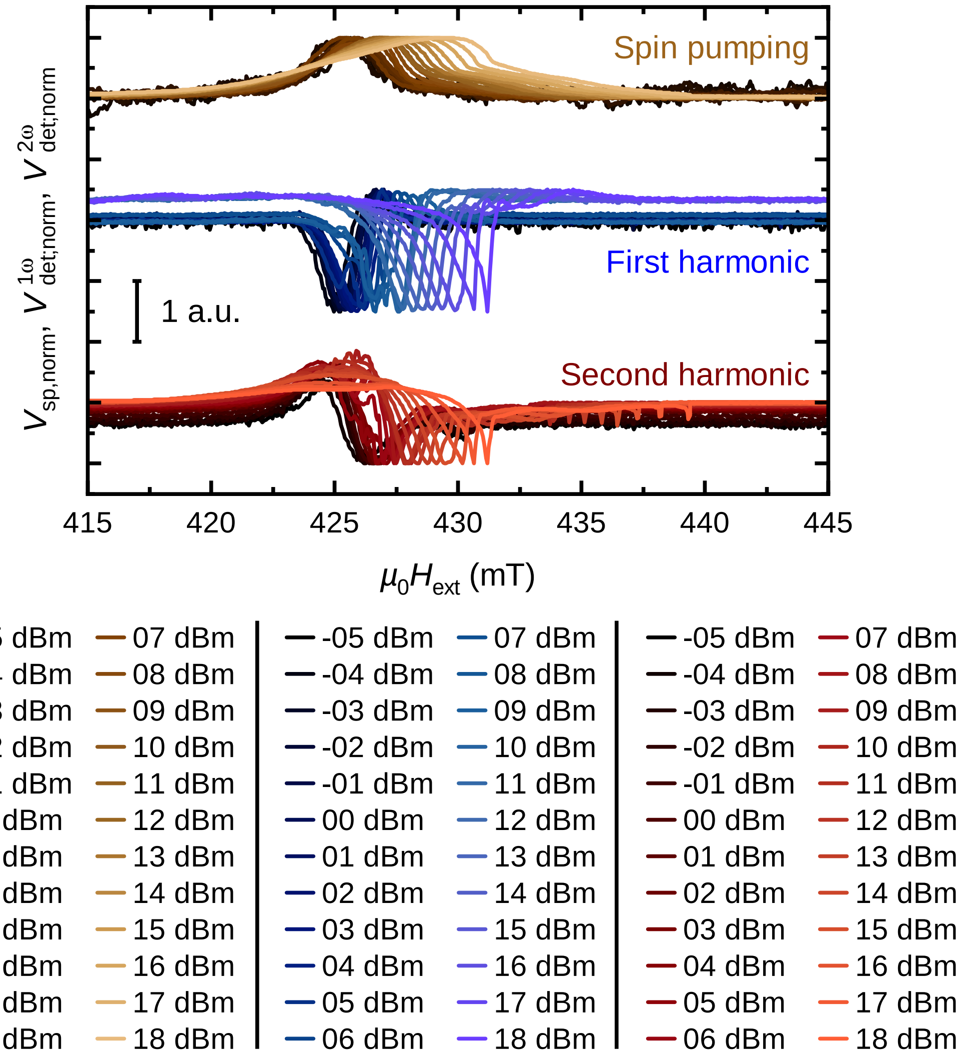

Figure 3.19: Overview over the normalized DC spin pumping voltage $V_{\mathrm{sp,norm}}$, the first harmonic $V^{1\omega}_{\mathrm{det,norm}}$ and the second harmonic $V^{2\omega}_{\mathrm{det,norm}}$ voltage for 14 GHz RF driving frequency and various powers given below. For every power, the voltages are each normalized to an interval of $[-1, 1]$ by its maximum and minimum value.

In general, because the amplitude of the step at zero field in $V_{\mathrm{det}}^{2\omega}$ is equal to the Joule heating magnon transport amplitude (as discussed in the previous Section 3.4.2), one can be certain that the baselines of both harmonic voltages are actually created via magnon transport only. This agrees with the fact, that the baselines of the voltages are determined away from the FMR condition, where there is no or only a negligibly small spin pumping voltage and therefore also **no** spurious contribution to the lock-in detection. Around the FMR, where high DC voltages are created via spin pumping, extreme modulations of the first and second harmonic voltages are observed. In this field range, which is shown in Fig. 3.19, a remarkable similarity between the modulations of the second harmonic and the first derivative/slope of the spin pumping voltage can be recognized. As the amplitude of the spin pumping peak is larger by about four orders of magnitude compared to the baseline transport voltages ($A_{\mathrm{sp}} \approx 100\,\mu\mathrm{V}$ versus $A^{\mathrm{SHE}} = 42\,\mathrm{nV}$ or $A^{\mathrm{therm}} = 74\,\mathrm{nV}$), already a tiny leakage in the range of a few percent would be able to create the observed amplitudes of the modulations. All of this points to the spin pumping voltage as the cause of the measurement artifacts.

We now want to qualitatively discuss a possible mechanism for leakage of V_{sp} into the lock-in detection. For this, the first derivative of the spin pumping voltage is calculated numerically using *Origin 2020* [Ori]. It is plotted in Fig. 3.20 together with the second harmonic voltage and the spin pumping voltage. This is done for two different RF driving frequencies and at each frequency for two different powers in order to make sure that the similarities do not only appear for a specific set of conditions, but instead are always present. Figure 3.20 makes it even clearer that the observed modulations in $V_{\mathrm{det}}^{2\omega}$ correspond exactly to the first derivative of V_{sp} in terms of qualitative shape. Thus, to give just one concrete example, the second small enhancement peak at high fields in the second harmonic can now be correlated with a sudden step in the spin pumping voltage. This is indicated by the blue arrows in Fig. 3.20, where it is particularly well visible for 14 GHz RF driving frequency and 15 dBm power. Note that the amplitudes were rescaled so that the qualitative similarities can be easily seen. However, this does **not** affect our conclusions, since the experimental amplitudes can be rescaled by different factors that we can not account for in a numerical derivative.

Since the lock-in amplifier detects the amplitude of the variation of the voltage with a specific frequency f_{ac}, and if the spin pumping voltage is assumed to be the cause of the measurement artifacts, it must also be at least partially time-dependent with the same frequency (or multiples of it). The origin of this time dependence might be the injector strip, through which the AC injector current of frequency $f_{\mathrm{ac}} = 7.121\,\mathrm{Hz}$ is driven. As its geometric dimensions are similar to those of the microstrip antenna, by analogy it creates an oscillating Oersted field according to the Karlqvist equations (see Section 2.3), which has the time dependence of the injector current. This time-variation is very slow and many orders of magnitude smaller than the RF driving

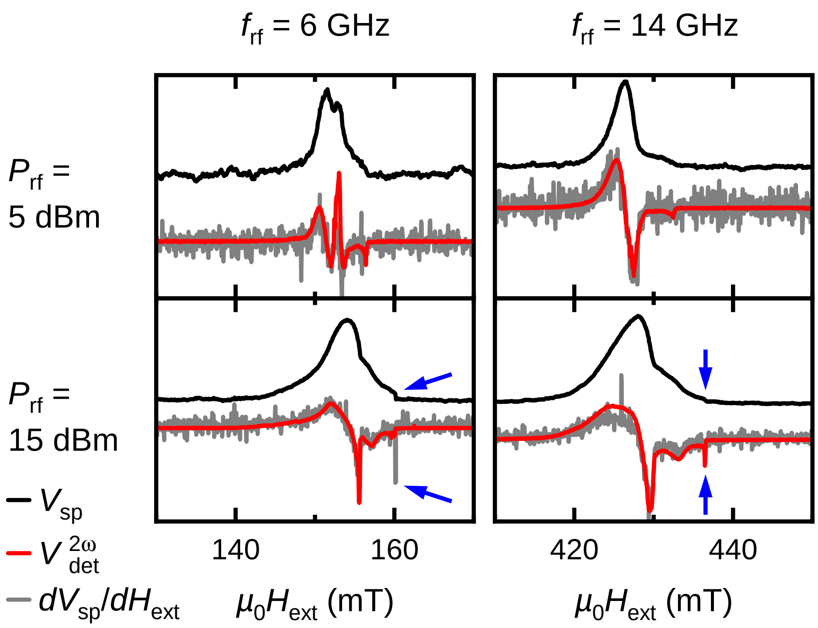

Figure 3.20: Magnetic field dependence of the DC spin pumping voltage V_{sp}, its first derivative $dV_{\mathrm{sp}}/dH_{\mathrm{ext}}$ with respect to the external magnetic field and the second harmonic voltage $V_{\mathrm{det}}^{2\omega}$ of the lock-in amplifier, each scaled by an arbitrary factor. The great qualitative resemblance between the first derivative and the second harmonic voltage indicates a leakage of the spin pumping voltage into the lock-in detection.

field, which is in the GHz-regime. Thus, the Oersted field of the injector can **not** drive the magnetization itself, but instead influences the resonance condition via a modulation of the external magnetic field

$$\mathbf{H}_{\mathrm{ext}}[t] = H_{\mathrm{ext}}\,\hat{\mathbf{e}}_{\mathrm{y}} + h_{\mathrm{inj,ip}}\,\hat{\mathbf{e}}_{\mathrm{y}} \sin[\omega_{\mathrm{ac}}t] + h_{\mathrm{inj,oop}}\,\hat{\mathbf{e}}_{\mathrm{x}} \sin[\omega_{\mathrm{ac}}t]\,. \tag{3.30}$$

On the one hand, the in-plane component of the injector Oersted field directly creates a time-dependence of the amplitude of the otherwise static magnetic field used to align the magnetization of the YIG. According to FMR theory (see Section 2.4), this naturally introduces a variation of the eigenfrequency of the magnetization precession. Consequently, the DC spin pumping voltage would be subject to the same variation and is thus picked up by the lock-in amplifier. The amplitude of the in-plane component of the Oersted field of the injector is negligibly small directly below the detector. However, as discussed previously in Section 3.3.2, we expect that most of the DC voltage stems from the propagating magnon induced spin pumping effect. If we consider the scenario, where the propagating magnons are initially excited directly below the injector, a much higher in-plane component can be assumed there. A rough estimate with Eq. (2.6) yields $h_{\mathrm{inj,ip}} = 0.25\,\mathrm{mT}$ (where we set $I_{\mathrm{rf}} = 200\,\mu\mathrm{A}$, $w_{\mathrm{cc}} = 500\,\mathrm{nm}$, $x = 5\,\mathrm{nm}$ and $y = 0\,\mathrm{nm}$). This is about three orders of magnitude smaller than the static external magnetic field. If we naively assume that this ratio is reflected one-to-one in the leakage of the spin pumping voltage, we would expect that about one percent of the spin pumping voltage is detected by the lock-in amplifier. This would roughly agree with the observations.

On the other hand, the variation in out-of-plane direction introduces an up-and-down wiggling of the external magnetic field and consequently of the magnetization of the YIG. This plays a relevant role only away from the injector, so mainly for the local spin pumping below the detector strip. A rough estimate with Eq. (2.5) gives $h_{\mathrm{inj,oop}} = 0.04\,\mathrm{mT}$ (where we set $I_{\mathrm{rf}} = 200\,\mathrm{\mu A}$, $w_{\mathrm{cc}} = 500\,\mathrm{nm}$, $x = 5\,\mathrm{nm}$ and $y = 1\,\mathrm{\mu m}$), which is four orders of magnitude smaller than the external magnetic field. Yet, it points perpendicular to the static external magnetic field, whereas the actually relevant variation has to be introduced into the parallel component and is thus even smaller. Because of this, and since we assumed in Section 3.3.2 that the local contribution to the spin pumping is negligibly small for most powers, we could deduce the same for the measurement artifacts. However, the oop-field scenario could explain why the measurement artifact is so striking in the second harmonic, as the up-and-down wiggling generates a small variation in y-direction with twice the frequency of the up-and-down movement.

Nevertheless, the exact origin and influence of the measurement artifacts can only be revealed by further measurements. Whether the work of Liu *et al.* [Liu+19] is also affected by those measurement artifacts is difficult to determine. They use a somewhat different sample design, where the microstrip antenna is much wider and placed next to one end of the strips and not right in between, so that there is only an out-of-plane component of the RF driving field below the strips. These simple geometric differences already makes a comparison regarding measurement artifacts very difficult. In any case, our results shine a different light on the matter and urge great caution in future experiments.

3.5 Summary

Recapitulating, we first managed to characterize the local properties of the thin YIG film via spin pumping through ferromagnetic resonance using a small on chip antenna. We saw Kittel-like behavior for the frequency dependence of the resonance field in good agreement with other works. Because of the splitting of the FMR into several modes for lower frequencies, we refrained from a detailed analysis of the frequency dependence of the linewidth, but still managed to observe a clear increase with the driving power.

Besides, the power dependence of the FMR spin pumping was also analyzed. There, we could differentiate between a linear and nonlinear regime, where the transition was indicated by a sudden increase of the linewidth, a premature saturation of the spin pumping amplitude and a deformation of the lineshape. Altogether, this proved the existence and relevance of higher order processes such as the second order Suhl instability. We also discussed that the deformation of the lineshape can be partially explained by effects of propagating magnon induced spin pumping as well.

Furthermore, the parametric pumping regime was reached, where we observed the formation of a subsidiary resonance (SR) stemming from the parallel pumping and/or the first order Suhl instability. Unfortunately, due to our sample layout, we could **not** differentiate between these two effects. For an RF driving frequency of 6 GHz, the power dependence of the SR was examined, detecting a clear threshold behavior. In addition, the frequency dependence of the onset of the SR was analyzed and fitted to theory.

We additionally characterized the amplitude of the magnon transport in the sample by angle dependent all-electrical magnon spin transport measurements. Then, an RF driving field was applied and its modulating influence on the transport voltages was examined. We observed modulations of the first and second harmonic voltage around ferromagnetic resonance and analyzed their power dependence, general shape and implications. On the one hand, a comparison with existing literature showed qualitative agreement in terms of general shape and power dependence. On the other hand, the modulation amplitudes in our data were much larger and even exceeded the transport baseline by several orders of magnitude, indicating the presence of measurement artifacts, as discussed in the previous section. These originate most likely from a leakage of the spin pumping voltage into the lock-in detection, which then dominates the signal. Yet, further measurements need to be conducted to achieve complete certainty in this matter.

Chapter 4

Magnon-Phonon Coupling

The interaction of magnetization and the lattice is quantitatively described by the magneto-elastic interaction. This concept, however, is not limited to the static case, but can be extended to dynamic stress in the lattice and magnetic excitations like magnons. An *et al.* [An+20] experimentally demonstrated the occurrence of magnon-phonon coupling between a magnetic excitation and a standing stress pattern present in a bulk acoustic resonator. We expand on this concept, which has been investigated solely from the perspective of ferromagnetic resonance spectroscopy, and add the readout concept of electrically detected spin pumping.

4.1 Theoretical Concepts

We discuss the explicit case of a trilayer system, where two ferrimagnetic insulator (FMI) layers with a finite magneto-elastic coupling enclose a non-magnetic insulator (NMI). When one of the ferrimagnetic insulators becomes excited using ferromagnetic resonance techniques, the angular momentum contained in this excitation can be transferred via the phononic system to the opposing layer. This section focuses on the description of this process from a model and theory perspective.

4.1.1 Setup and Equations of Motion

We consider a system with a thin film of a ferrimagnetic insulator (FMI layer 1 with thickness t_{FMI1}) on the bottom followed up by a much thicker film of a non-magnetic insulator (NMI with thickness t_{NMI}). This is then capped by a second ferrimagnetic insulator (FMI layer 2 with thickness t_{FMI2}). In general, the two FMI layers can be of different thickness and material, but for the scope of this thesis, they will be considered equal with only a slight difference in the Kittel FMR resonance behavior. This configuration is depicted in Fig. 4.1.

An RF driving field $\mathbf{h}_{\mathrm{rf}}$ is applied to the FMI|NMI|FMI-stack, driving the magnetization of both FMI layers via the process of ferromagnetic resonance. The result is a dynamic motion of both magnetizations. Those can now transform their spin angular momentum in a shear lattice deformation that travels through the NMI as phonons. In more detail, a precession of the magnetization in a ferrimagnetic insulator thin film is coupled to the lattice via magnetostriction [Kit58]. Hence, a precessing

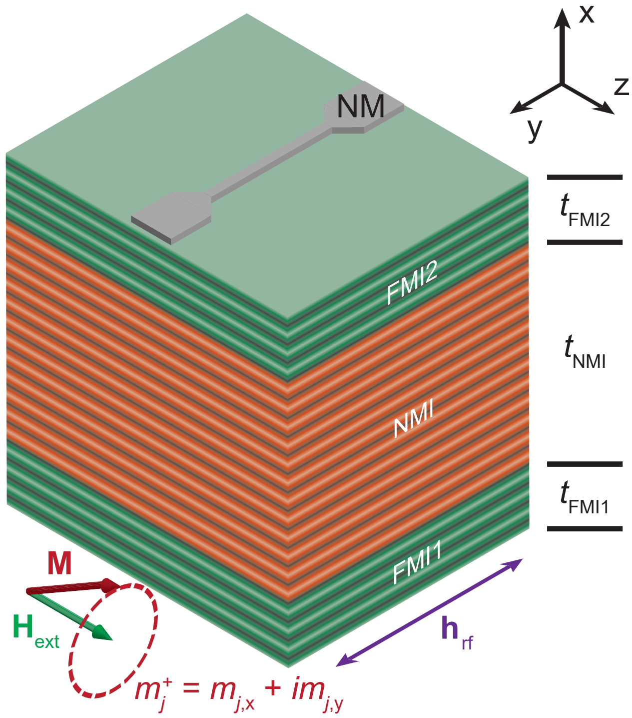

Figure 4.1: FMI|NMI|FMI trilayer in an in-plane applied external magnetic field $\mathbf{H}_{\text{ext}}$, causing a precession of the magnetizations $\mathbf{M}$ of each layer, which is resonantly driven by an RF field $\mathbf{h}_{\text{rf}}$ in ferromagnetic resonance. For simplicity, only one magnetization is shown. The magnetization dynamics perpendicular to the external magnetic field are described by the complex-valued parameters m_j^+ with $j = 1$ or 2 for the lower or upper FMI layer, respectively. Phononic shear deformation of the lattice is indicated by the periodic change of color along the thickness of the trilayer.

magnetization induces an oscillation of the lattice with the same frequency as the precessional motion, resulting in phonon excitations. A more detailed theoretical description is given by Streib *et al.* [Str+19]. If, for example, we consider the case where the magnetization is aligned in normal direction with respect to the film plane, the surface of the thin film starts a rotational shear deformation around H_{ext}. This creates circularly polarized transverse sound waves that can be emitted into a neighboring non-magnetic insulator. This transformation of spin waves into acoustic waves (and the other way around) was first observed by H. Bömmel and K. Dransfeld in 1959 [BD59]. It creates an additional damping channel for the magnetization, as magnetic excitation can be transformed into phonons and absorbed by the non-magnetic layer [SKB18]. On the other side of the NMI, those phonons can be transformed back into magnons via the inverse process and eventually influence the magnetization precession of the other film. In short, this allows coupling of the two magnetic layers via a phononic bus. This interaction can be described via three coupled differential equations for the three subsystems (FMI1, FMI2, NMI) [An+20]

$$(\omega_{\mathrm{rf}} - \omega_1 + i\eta_{\mathrm{m}})\, m_1^+ = \Omega_1 u_n^+/2 + \kappa_1 h_{\mathrm{rf}}, \tag{4.1}$$

$$(\omega_{\mathrm{rf}} - \omega_2 + i\eta_{\mathrm{m}})\, m_2^+ = \Omega_2 u_n^+/2 + \kappa_2 h_{\mathrm{rf}}, \tag{4.2}$$

$$(\omega_{\mathrm{rf}} - \omega_n + i\eta_{\mathrm{a}})\, u_n^+ = \Omega_1 m_1^+/2 + \Omega_2 m_2^+/2. \tag{4.3}$$

Here, η_{m} (η_{a}) is the relaxation rate of the magnetic (acoustic) system, Ω_1 (Ω_2) the magneto-elastic interaction strength in the lower (upper) FMI layer and κ_1 (κ_2) the inductive coupling between the lower (upper) FMI layer and the RF driving field. For the magneto-elastic interaction, one can assume $\Omega_1 = \Omega_2$ for constructive and $\Omega_1 = -\Omega_2$ for destructive interference between the magnetization precessions of the two layers. Furthermore, ω_{rf} (h_{rf}) describes the angular frequency (amplitude) of the RF driving field. The Kittel resonance frequency of the lower (upper) FMI layer is given by ω_1 (ω_2). The dynamic motion of the magnetization of the lower (upper) layer is described by the complex-valued parameter m_1^+ (m_2^+), the shear lattice deformation of the trilayer by u_n^+. Note that the real and imaginary parts of the complex-valued parameters describe the dynamics in x- and y-direction, respectively, i.e. $m_j^+ = m_{j,\mathrm{x}} + i m_{j,\mathrm{y}}$ with $j = 1$ (or 2) for the lower (upper) FMI layer. The angular frequencies, where the phonon mediated interference effects take place, are equally spaced and given by ω_n. They can be calculated from the acoustic wave velocity v_{aw} and the total thickness $t_{\mathrm{tot}} = t_{\mathrm{FMI1}} + t_{\mathrm{NMI}} + t_{\mathrm{FMI2}}$ of the FMI|NMI|FMI-stack

$$\omega_n = \frac{\pi v_{\mathrm{aw}}}{t_{\mathrm{tot}}} n, \tag{4.4}$$

where $n \in \mathbb{N}$ gives the order of the resonance. In this thesis, the thicknesses of the two FMI layers are equal $t_{\mathrm{FMI1}} = t_{\mathrm{FMI2}} \equiv t_{\mathrm{FMI}}$ and we can rewrite the above equation to

$$\omega_n = \frac{\pi v_{\mathrm{aw}}}{2t_{\mathrm{FMI}} + t_{\mathrm{NMI}}} n. \tag{4.5}$$

As evident from Eqs. (4.1) to (4.3), the magnetic excitation of the two ferrimagnetic insulators and the acoustic excitation in the phononic system is modeled in terms of harmonic oscillators with resonance frequencies ω_1, ω_2, and ω_{n} and a damping parameter η_{m} and η_{a} for the magnonic and phononic subsystems, respectively. In addition, the equations are coupled using the parameters Ω_1 and Ω_2 that quantify the magnon-phonon interaction. Eqs. (4.1) to (4.3) are solved for the complex-valued variables m_1^+, m_2^+ and u_n^+. In this spirit, one can understand Eq. (4.1) as the equation of motion for the magnetization of the lower FMI layer, Eq. (4.2) as that for the upper layer and Eq. (4.3) as that for the phonons present in the system. Those relatively simple equations grant us the possibility to calculate and simulate the theoretical behavior of the system.

4.1.2 Observables

One important question still left to answer is the qualitative connection between the abstract variables m_1^+, m_2^+ and u_n^+ in Eqs. (4.1) to (4.3) and real physical quantities that can be measured in an experiment. This is addressed in this section.

The observables in later experiments are the spin pumping voltage V_{sp} and the transmission through a CPW, measured as the complex S_{21} parameter of a vector network analyzer. We first take a closer look at the spin pumping voltage.

The process behind the creation of a spin pumping voltage was explained in detail in Section 2.6. There, we concluded the chapter with Eq. (2.45), an analytical expression for the spin pumping voltage. We also noted that its dependence on the cone angle θ of the magnetization precession, which is given by Eq. (2.46), is of special interest for us. Figure 4.2 visualizes the geometry of the situation again. With that, we can easily connect this experimental observable with the quantity m_i^+ via

$$V_{\mathrm{sp}} \propto \sin^2\theta \propto \left|m_2^+\right|^2 , \tag{4.6}$$

assuming that the magnetization is excited in the linear response regime. In particular, since spin pumping is sensitive to the specific interface of the FMI2|NM, we can selectively detect m_2^+. This is a huge advantage compared to the inductive signal originating from both FMI layers detected with CPW FMR, where it can be challenging to differentiate between the signals of both FMI layers. Furthermore, the CPW FMR signal is dominated by the lower FMI layer due to its higher inductive coupling to the CPW. It thus becomes challenging to observe the dynamics of the upper layer.

As stated before, the other observable is the transmission through the CPW, which is measured as the complex S_{21} parameter of a vector network analyzer (VNA) and was discussed in detail in Section 2.5. There, we concluded with Eq. (2.35), which is repeated in the following

$$|\Delta S_{21}| \propto |\mathbf{m}_\perp| .$$

Similar to the previously discussed case of the spin pumping voltage, one can identify $|\mathbf{m}_\perp|$ as $\left|m_i^+\right|$ in the equations of motion. Including a second FMI layer, this allows us to calculate ΔS_{21} from the theory equations

$$|\Delta S_{21}| \propto \left|m_1^+ + \frac{\kappa_2}{\kappa_1} m_2^+\right| , \tag{4.7}$$

where we included the coupling between the magnetization of each layer and the CPW because we need to account for it twice: once for the coupling to drive the magnetization and once for the inductive coupling of the precessing magnetization back to the CPW [Sil+16; Ber+18]. A potential phase difference caused by the different distances and thus propagation times between the respective FMI layer and

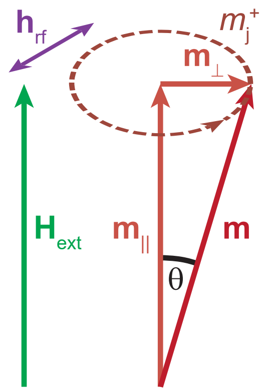

Figure 4.2: A magnetic moment $\mathbf{m}$ precessing in an external magnetic field $\mathbf{H}_{\text{ext}}$ with a cone angle θ. It is driven in ferromagnetic resonance by the RF field $\mathbf{h}_{\text{rf}}$. The magnetic moment can be split up into two components, one parallel $\mathbf{m}_{||}$ and one perpendicular $\mathbf{m}_{\perp}$ to $\mathbf{H}_{\text{ext}}$. Then, $\mathbf{m}_{||}$ stays constant with time, whereas $\mathbf{m}_{\perp}$ rotates around its origin. This motion can be described using the complex-valued parameter m_j^+.

the CPW is assumed to be negligibly small and is therefore not accounted for.

There are two main differences compared to the expression for the spin pumping voltage V_{sp} given in Eq. (4.6). First, both m_1^+ and m_2^+ of the upper and lower FMI layer contribute to the CPW FMR signal. Since the FMI layer 1 is much closer to the CPW, the amplitude of the RF driving field is larger there and its contribution to ΔS_{21} is dominating. Second, the CPW FMR signal ΔS_{21} only depends on the magnitude of m_j^+, whereas the spin pumping signal V_{sp} is given by the magnitude squared.

4.2 Simulation

To obtain further insight into the experiment, simulations were performed in *Wolfram Mathematica 12.1* [Wol] based on the theory proposed in Section 4.1. Given a set of parameters, Eqs. (4.1) to (4.3) are solved for the complex variables u_n^+, m_1^+ and m_2^+ in a desired magnetic field and microwave frequency range. Because it is not possible to evaluate Eqs. (4.1) to (4.3) for several phonon resonance angular frequencies ω_n simultaneously, the frequency range is set only around a given phonon resonance ω_n. This is done in such a way, that the calculated frequency range starts exactly in the middle between ω_{n-1} and ω_n, and ends in the middle between ω_n and ω_{n+1}. Consequently, one can afterwards simply go to the next ω_{n+1}, compute the variables in the next frequency range and place the result next to the last. With this approach, it is possible to iteratively obtain a complete simulation over a large frequency range with an arbitrary amount of magnon-phonon resonances, as long as they are spaced far enough apart relative to their frequency width.

4.2.1 Parameters

The values of the parameters in Eqs. (4.1) to (4.3) were manually optimized so that the final result is as close as possible to the experimental data (see Section 4.3). In this spirit, let us now discuss the individual parameters, how they are computed and how they generally influence the result.

$\boldsymbol{\Omega_{1/2}}$ describes the strength of **magneto-elastic interaction** of FMI layer 1/2 (lower/upper layer). It is equal to the value of the magneto-elastic overlap integral between the spin wave and the acoustic wave [Bra+20]. In general, its value strongly depends on the considered frequency interval. However, since we are only considering a small frequency range, it is assumed to be constant in the following. A higher value means a more effective conversion from magnons to phonons and broadens the phonon resonance in the frequency space. Lower values give a less effective conversion and curtail its width. Note that we assume $\Omega_1 = \pm\Omega_2$ with the plus (minus) sign for constructive (destructive) interference between the two FMI layers.

$\boldsymbol{\eta_a}$ represents the **acoustic relaxation rate**. Higher values imply a stronger relaxation channel, which blurs the phonon resonances. For lower values, the resonances get sharper.

$\boldsymbol{\eta_m}$ gives the **magnetic relaxation rate**. A higher value increases the magnetic damping and thus broadens the FMR of both layers. If the FMI films have significant differences, one should think about introducing individual relaxation rates for the two layers. But in the scope of this thesis, this is not required.

$\boldsymbol{\kappa_{1/2}}$ specifies the **inductive coupling** between FMI layer 1/2 and the RF driving field. The higher its value, the more energy is absorbed by the respective layer from the RF driving field. It can also be understood as a measure of the RF field magnitude at each FMI layer due to their different distances from the source of the RF driving field. The ratio between κ_1 and κ_2 is determined using the Karlqvist equations by calculating the in-plane RF driving field at the center above a coplanar waveguide (CPW) with Eq. (2.6) first for the distance to the lower FMI layer 1 and then to the upper FMI layer 2. The ratio between those two fields is assumed to be equal to the ratio between the inductive couplings

$$\frac{\kappa_1}{\kappa_2} = \frac{\mu_0 h_{\mathrm{rf},1}}{\mu_0 h_{\mathrm{rf},2}} \approx \frac{28\,\mu\mathrm{T}}{13\,\mu\mathrm{T}} \approx 2, \tag{4.8}$$

where we set $P_{\mathrm{rf}} = 20\,\mathrm{dBm}$, $Z_0 = 50\,\Omega$, $w_{\mathrm{cc}} = 1\,\mathrm{mm}$, $y = 0\,\mathrm{m}$ and $x = 1\,\mu\mathrm{m}$ or $545\,\mu\mathrm{m}$ for the lower or upper FMI layer, respectively. Since we are only interested in a qualitative simulation of the experiment, the exact values of κ_1, κ_2 and h_{rf} are of arbitrary choice as long as the condition in Eq. (4.8) is met.

$\boldsymbol{\omega_n}$ gives the location of a **phonon resonance**. Its value is directly taken from the experimental data. The distance between neighboring resonances is assumed to be constant $\omega_{n+1} - \omega_n = \mathrm{const.}$ and taken as the average spacing in the experiment.

$\boldsymbol{\omega_{1/2}}$ characterizes the **FMR resonance frequency** of FMI layer 1/2 and therefore depends on the external magnetic field $\mu_0 H_{\mathrm{ext}}$. It is calculated via the Kittel equations, which we solve for f_{res} in the in-plane case (see Eq. (2.24)). We further change to angular frequency by multiplying with 2π and correlate with the resonance frequencies ω_1 and ω_2 of the respective FMI layers to find

$$\omega_1 = \gamma\mu_0 \sqrt{\left(H_{\mathrm{ext}} + \frac{M_{\mathrm{eff}}}{2}\right)^2 - \left(\frac{M_{\mathrm{eff}}}{2}\right)^2}, \tag{4.9}$$

$$\omega_2 = \gamma\mu_0 \sqrt{\left(H_{\mathrm{ext}} - H_{\omega_1\omega_2} + \frac{M_{\mathrm{eff}}}{2}\right)^2 - \left(\frac{M_{\mathrm{eff}}}{2}\right)^2}, \tag{4.10}$$

where $\gamma = 28 \times 2\pi\,\mathrm{GHz/T}$ is the gyromagnetic ratio given by its literature value. With $H_{\omega_1\omega_2}$ we also introduced a phenomenological term in Eq. (4.10) that defines a finite offset between the position of the FMR of the upper and lower FMI film. Its value and the one of M_{eff} is selected so that the simulation describes the experimental data as well as possible. In general, higher values of $H_{\omega_1\omega_2}$ will increase the distance between the FMRs by shifting the FMR of FMI layer 2 towards higher external magnetic fields. An increase of the effective magnetization M_{eff} will cause an equal shift of the FMRs of both FMI films towards lower fields. Both M_{eff} and $H_{\omega_1\omega_2}$ are used to bring the simulated FMR into the field range observed in the experiment.

The simulation returns one matrix of values for the spin pumping voltage and one for the CPW FMR signal, which are calculated using Eqs. (4.6) and (4.7), respectively.

They are plotted in *Origin 2020* [Ori] in a 2D colorplot as a function of the external magnetic field $\mu_0 H_{\text{ext}}$ on the x-axis and the RF driving frequency $f_{\text{rf}} = \omega_{\text{s}}/(2\pi)$ on the y-axis in full analogy to the experimental data. The used parameter values are listed in Table 4.1.

Table 4.1: Parameter values used in all simulations presented in this chapter.

parameter	value
Ω_1	$0.8 \times 2\pi \times 10^6$
Ω_2	$\pm 0.8 \times 2\pi \times 10^6$
η_{a}	$1.5 \times 2\pi \times 10^5$
η_{m}	$15 \times 2\pi \times 10^6$
κ_1	10^6
κ_2	5×10^5
h_{rf}	100
ω_n	$2\pi \left(1.9516 \times 10^9 + n \times 3.2357 \times 10^6\right)$
$\mu_0 H_{\text{eff}}$	0.227
$\mu_0 H_{\omega_1 \omega_2}$	0.00047

4.2.2 Results

As previously stated, the simulation gives one matrix of values for the spin pumping and one for the CPW FMR signal, where the row and column of an entry indicate the associated RF driving frequency and external magnetic field, respectively. As shown in Fig. 4.3, this matrix can be visualized as a two dimensional colorplot with the external magnetic field on the x-axis and the RF driving frequency on the y-axis. The point spacing of the simulation is $20\,\mu\text{T}$ in field and $3.2357 \times 2\pi\,\text{MHz}/32 \approx 635\,\text{kHz}$ in frequency.

The dominant feature in the transmission plot in Fig. 4.3 (a) is the ferromagnetic resonance of the lower FMI layer. It shows up in the from of a black diagonal line. As visible there, and in agreement with the theory presented in Section 2.4, a higher external magnetic field amplitude corresponds to a higher eigenfrequency of the magnetization precession and thus requires a higher RF driving frequency (therefore the diagonal shape). At its right edge, the FMR of the upper FMI layer can be vaguely recognized as a light gray extension of the black diagonal. This agrees with the expectations because the transmission signal of the upper FMI layer is strongly suppressed compared to that of the lower layer due to its greater distance to the RF driving field source.

In contrast, the FMR of the upper FMI layer is clearly visible in the spin pumping voltage displayed in Fig. 4.3 (b), as it is only generated by the magnetization dynamics of the upper FMI layer. Moreover, the artificially introduced field shift

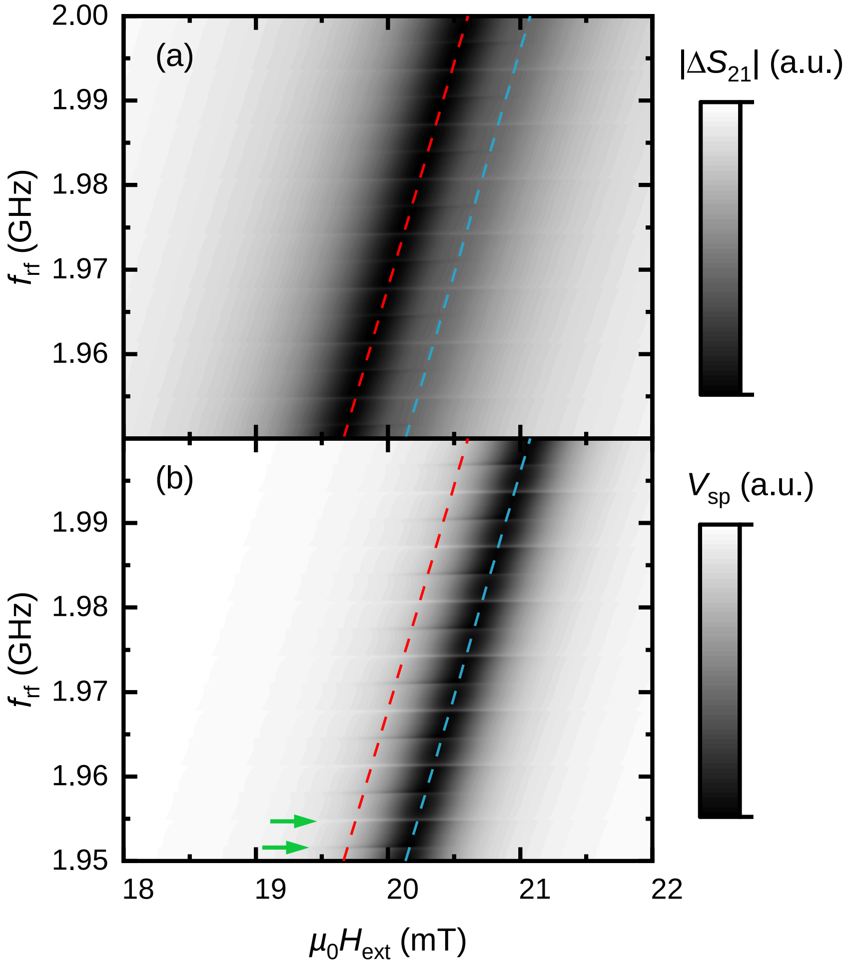

Figure 4.3: (a) Simulated ΔS_{21} parameter of the VNA and (b) spin pumping voltage V_{sp} as a function of the external magnetic field $\mu_0 H_{ext}$ on the x-axis and the RF driving frequency f_{rf} on the y-axis. The red and blue dashed lines show the FMRs of the lower (see Eq. (4.9)) and upper (see Eq. (4.10)) FMI layer, respectively. The first destructive (at lower frequency) and constructive (at higher frequency) magnon-phonon resonances are indicated by the green arrows. The parameter values used for the displayed simulation are given in Table 4.1.

between both FMRs can be well recognized by e.g. looking at the lower end of FMR1 and FMR2 at a bit above 19.5 mT in (a) and 20 mT in (b), respectively. Its size is defined by $H_{\omega_1\omega_2}$, which is 0.47 mT, and nicely reflected in the colorplot. The extended light gray area in Fig. 4.3 (a) also aligns well with the spin pumping signal in (b). As expected from the theory (see Section 4.1.2), there is no sign of the FMR of the lower FMI layer in the spin pumping voltage.

The magnon-phonon interference shows up as black and white horizontal lines in the ferromagnetic resonance. The first one can be seen slightly above 1.95 GHz as a horizontal black extension of the FMR towards higher fields in Fig. 4.3 (a) and towards lower fields in (b). It is of destructive nature. Afterwards, the resonances alternate between constructive and destructive, where constructive interferences occur for even mode numbers n in Eq. (4.4) and destructive for odd. More precisely, constructive interference means that the phonons pumped by the magnetization dynamics of the lower FMI layer are absorbed by the upper FMI layer, while they are reflected in the destructive case. This corresponds to the phonon amplitude being in phase for constructive interferences or out of phase for destructive interferences, respectively [An+20]. They clearly differ from each other in their shape and appearance in Fig. 4.3, where the destructive interference is characterized by an extended black horizontal line, whereas in the constructive case a white horizontal line can be seen. The detailed structure of the destructive interference is evident in the spin pumping voltage shown in Fig. 4.3 (b), where it appears as a white horizontal line at lower frequencies that changes into a black horizontal line at slightly higher frequencies. This shape can be explained by a phase shift of 180° between the precession of the magnetization of the upper and lower FMI layer in the case of destructive interference.

Compared to the simulation shown in An *et al.* [An+20], our FMR lines have a significantly wider frequency linewidth that masks the fine structures visible in [An+20]. Besides, a more educated model (see Eqs. (4.9) and (4.10)) is used in this thesis to calculate the position of the ferromagnetic resonance. This is necessary because we consider ferromagnetic resonance for a magnetic field applied in the film plane, whereas a simple linear model (i.e. $\omega_1 = \gamma\mu_0 (H_0 - M_1)$) is sufficient for the out-of-plane magnetic field geometry studied in An *et al.* [An+20]. Besides, the general qualitative shape is unsurprisingly very similar to our simulation, as we use the same theoretical model as a basis.

4.3 Experiment

Now that we have a basic understanding as well as an expectation for the results, we can come to the experimental part. First, the setup and the measurement techniques are presented. After that, the results are shown and discussed, always comparing to the theoretical model and the simulation presented in Sections 4.1.1 and 4.2.2, respectively.

4.3.1 Setup

The design of the experiment is based on the structural concept introduced earlier in Fig. 4.1 of Section 4.1.1 as the basis of the theoretical model. More precisely, we use again gadolinium gallium garnet (GGG, $Gd_3Ga_5O_{12}$) as a non-magnetic insulator and yttrium iron garnet (YIG, $Y_3Fe_5O_{12}$) as a ferrimagnetic insulator, as it was already shown by An *et al.* [An+20] that coherent long-range transfer of angular momentum between magnons and phonons can be observed in such a system. Both YIG layers have the same thickness with $t_{\mathrm{YIG1}} = t_{\mathrm{YIG2}} = 1\,\mu\mathrm{m}$. The GGG layer in between is significantly thicker at $t_{\mathrm{GGG}} = 0.5\,\mathrm{mm}$. The trilayer as a whole is 6 mm wide and 10 mm long. On its top side, platinum (Pt) is used for the nanostructured normal metal strip due to its high conversion efficiency between spin and charge currents. The Pt strip is Al wire bonded and connected to a nano-voltmeter so that a spin pumping voltage can be measured along its length. It has a width of 500 nm, a length of 100 µm and a thickness of 5 nm similar to before in Section 3.2.1. The magnetizations of both YIG films are aligned in-plane and perpendicular to the Pt strip by an external magnetic field, which is applied along the z-axis. All of this is depicted in Fig. 4.4.

Furthermore, the sample was glued on top of a coplanar waveguide (CPW), through which an RF current in the low GHz regime is driven by a vector network analyzer (VNA). This creates an RF driving field that deflects the magnetizations in the two YIG films from their equilibrium positions when the ferromagnetic resonance condition applies. The CPW has a center conductor width of 1 mm as a compromise between two competing factors. On the one hand, a broad CPW gives a large in-plane field component over a large area, which is necessary to drive the magnetization via FMR. Ideally, the RF driving field is oriented fully in-plane and perfectly parallel to the Pt strip along its entire length. Experimentally, this can be achieved much easier with a wide CPW. On the other hand, the driving field amplitude is, according to the Karlqvist equations (see Section 2.3), smaller for a broader center conductor. On top of that, the signal picked up by the CPW is also inversely proportional to the center conductor width [Ber+18]. Consequently, a thinner CPW would be beneficial in order to increase both the RF driving field amplitude and the signal amplitude in the S_{21} parameter.

The CPW with the trilayer on top was then mounted on a dipstick and placed into

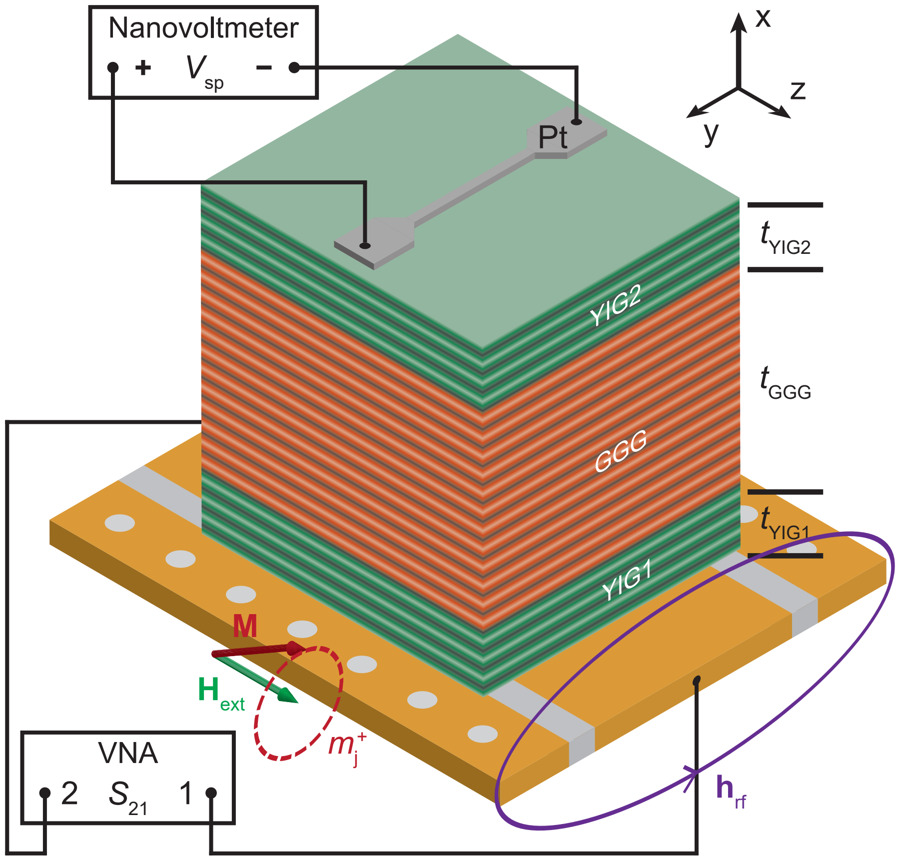

Figure 4.4: A trilayer of YIG|GGG|YIG on top of a coplanar waveguide (CPW). The magnetization $\mathbf{M}$ of both YIG films is aligned in-plane by an external magnetic field $\mathbf{H}_{\mathrm{ext}}$. The CPW is connected to a vector-network-analyzer (VNA), which sends an RF current through it in order to generate the RF driving field $\mathbf{h}_{\mathrm{rf}}$. The signal transmitted through the CPW is picked up again by the VNA and analyzed in terms of amplitude and phase relative to the output signal. A Pt strip is nanostructured on top the upper YIG layer. In ferromagnetic resonance, a spin pumping voltage V_{sp} is created, which we measure with a nanovoltmeter.

the ***CHAOS*** cryostat at the WMI. All measurements were performed at 280 K, i.e. at room temperature, and with an RF driving power of 20 dBm. A Keithley 2182 nanovoltmeter was used for the voltage measurements and a Keysight PNA as a VNA due to its high output power. For the VNA, a measurement bandwidth of 1 kHz and an averaging of ten points per frequency point was set.

4.3.2 Results

The measurement procedure in the experiment starts by first applying the external magnetic field at a fixed amplitude. Then a fixed RF driving frequency was set via the VNA, for which both the transmission through the CPW, i.e. the ΔS_{21} parameter, and the spin pumping voltage were measured. Then the frequency was slightly increased and the measurements were repeated. This was done until the entire frequency range was covered. Now the amplitude of the external magnetic field was slightly decreased and the same procedure was repeated. This time consuming measurement scheme is necessary because the VNA must always be operated in the continuous wave (CW) mode to allow a simultaneous measurement of the CPW FMR and the spin pumping voltage. So in short, the field was swept from large to small values and for each field amplitude the frequency was swept from small to large values. The inverted scheme, where the frequency is fixed and the whole field range is swept for each frequency point, is also conceivable, but brings with it some disadvantages. First, the repeated sweeping of the field can introduce trapped flux into the system and thus corrupt the measurements. Second, the measurements would take even longer since setting a new external magnetic field amplitude is experimentally much more time consuming than setting a different RF driving frequency.

With this, we obtain the spin pumping voltage and the transmission through the CPW as a function of both the external magnetic field amplitude $\mu_0 H_{\mathrm{ext}}$ and the RF driving frequency f_{rf}. They are both displayed as a two dimensional colorplot similar to the simulation in Section 4.2.2. The S_{21} parameter obtained from the VNA is divided by slice before it is plotted, which means that every frequency slice is divided by the frequency slice of the highest measured field. This is done to correct an amplitude change with frequency induced by the VNA, cables or CPW, i.e. the setup itself. It is the usual way in which results are displayed in this field of research. The resulting colorplots are shown in Fig. 4.5, where the upper panels (a) and (b) show the transmission and the lower panels (c) and (d) the spin pumping voltage, respectively. Experimentally obtained data is displayed on the right in (b) and (d), whereas on the left (a) and (c) depict the results of the simulation (see Fig. 4.3) again for comparison. Measurement points in the experiment were set at a distance of 50 µT in field and 100 kHz in frequency from each other.

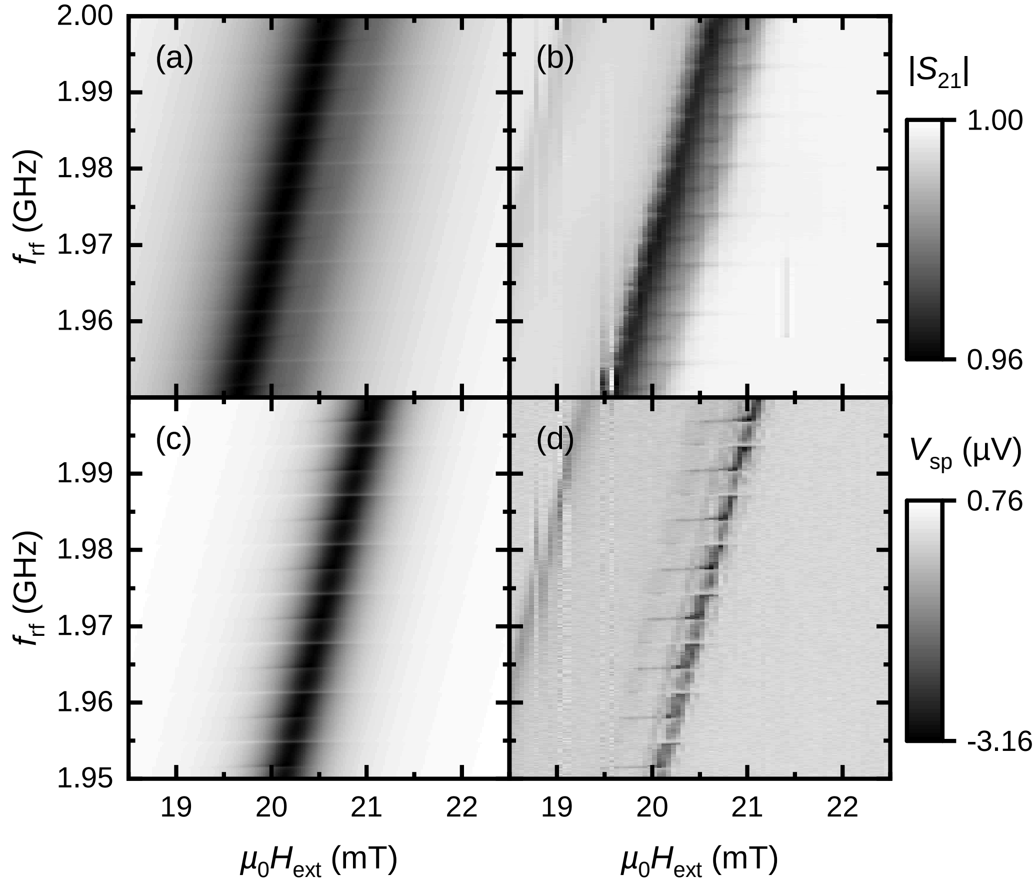

Figure 4.5: (a) and (b) S_{21} transmission parameter of the VNA and (c) and (d) spin pumping voltage, all plotted as a function of the external magnetic field $\mu_0 H_{\mathrm{ext}}$ on the x-axis and the RF driving frequency f_{rf} on the y-axis. The left panels (a) and (c) show the results from the simulation, whereas the right panels (b) and (d) depict the experimentally obtained data. The color scales on the right belong to panels (b) and (d), respectively.

The dark diagonal line created by the ferromagnetic resonance of the lower YIG layer is also clearly visible in the experimentally measured transmission in Fig. 4.5 (b), again with the light gray extension at the high-field side stemming from the FMR of the upper YIG layer. The spin pumping voltage also nicely reflects the expectations from the theory with a clearly visible FMR signal at the field and frequency position of the upper layer. Its maximal amplitude is with 3.16 µV a bit more than four times as large as the noise floor, which lies at around 0.76 µV. Furthermore, the simulation correctly reflects the shift between the two layers (which is obvious since the parameters were tuned in order to achieve this). An additional faint black line can be seen in the experimental data at lower magnetic fields especially in the spin pumping voltage, starting at around 1.965 GHz and 18.5 mT and ending at 19.25 mT and 2 GHz. Most likely, it can be explained by a perpendicular standing spin wave (PSSW). But since it does not affect the FMR and shows no apparent sign of magnon-phonon coupling, it is not investigated further.

As predicted by theory and simulation, the magnon-phonon resonances show up as horizontal lines in the FMR diagonals, obeying the characteristics demanded by the simulation. The destructive interferences are particularly evident in the spin pumping voltage. There, they appear as horizontal black lines that extend towards lower fields until the low-field end of the FMR of the lower YIG layer is reached, agreeing very nicely with the theoretical expectations. The white horizontal lines are again constructive magnon-phonon interferences. As expected, the two resonances alternate with each other and are also clearly visible in the transmission signal. Interestingly, the amplitude of the spin pumping voltage also alternates in the scheme of constructive and destructive interferences. It is larger (darker in Fig. 4.5) above a destructive and smaller (lighter) above a constructive resonance. In terms of general qualitative shape, the simulation describes the experiment very well. Moreover, the experimental field and frequency resolution of the spin pumping voltage seems to be better than that of the transmission signal, which looks rather smeared out in the experiment, even though they are measured simultaneously and thus with the same sampling. One conceivable reason for this difference might be that the detection of the spin pumping signal is strongly localized to the specific region of the YIG on which the Pt strip is patterned. The CPW FMR signal, on the other hand, is the response of the entire YIG film and thus an average over the entire layer. Due to fabrication imperfections, different areas of the YIG have slightly different properties, which influences the local FMR condition and consequently creates a smearing of the measured sum signal. Another possible cause for the increased smearing could be the tenfold averaging of each measurement point of the CPW FMR signal, in contrast to the single measurement for each point of the spin pumping signal.

From the experimental data, one can calculate the periodicity between the magnon-phonon resonances. We extract the frequency of the lowest and highest measured resonance by hand and divide the difference by the number of resonances in between to find a periodicity of

$$\frac{1.9970\,\mathrm{GHz} - 1.9516\,\mathrm{GHz}}{14} \approx 3.24\,\mathrm{MHz}, \tag{4.11}$$

which is in good agreement with the 3.50 MHz observed by An *et al.* [An+20] and the theoretical expectations from the transverse sound velocity $v_{\mathrm{aw}} = 3.53\,\mathrm{km/s}$ [YD91; Khi+18] in GGG along the (111)-direction. The experimentally obtained value given in Eq. (4.11) is used for the spacing of the interferences in the simulation (see value of ω_n in Table 4.1). It can further be translated into an expectation for the total sample thickness via Eq. (4.4). We find $t_{\mathrm{tot}} = 545\,\mathrm{\mu m}$, which corresponds to a 543 µm thick GGG layer in the middle, assuming a thickness of 1 µm of the upper and lower YIG layer. This is in relatively good agreement with the typical thickness of around 500 µm. Besides, we can calculate the phonon mode number n of the interference and find $n \approx 610$, assuming a constant spacing down to zero frequency. As expected, this is much lower compared to An *et al.* [An+20] (who found $n \approx 1400$), since they operated their experiment in a different frequency and field range at around 5.1 GHz and 345 mT.

An *et al.* [An+20] further extract diagonal slices along the course of the FMR from their measurements. There, they observe a periodic amplitude modulation as an indication of the magnon-phonon resonances. We have tried to reproduce this, but with insufficient results. Most likely due to an insufficient point spacing in our case, artifacts are introduced as the predominant feature. Thus, we could not reproduce the results in [An+20] in this specific regard, which is why these slices are not shown here. Nevertheless, our observations agree very well with [An+20] in terms of qualitative shape and appearance (e.g. they also saw the magnon-phonon interferences as horizontal lines in the ferromagnetic resonance) as well as in the resonance spacing discussed in the paragraph above. Moreover, we especially shed new light on the matter by measuring the spin pumping voltage. This allows direct and exclusive access to the dynamics of the upper YIG layer, which was previously **not** possible. We also apply the RF driving field via a coplanar waveguide, whereas in contrast, An *et al.* [An+20] relied on a microwave cavity. On the negative, the CPW generally has a worse signal to noise ratio than a cavity as used in [An+20]. But on the positive, a cavity restricts the experimentalist to a narrow frequency range around the resonance frequency of the cavity, whereas a CPW enables an examination of the phenomenon over a broad frequency range.

As a next step, we will take a closer look at the properties and the appearance of a single magnon-phonon resonance. For this purpose, the field and frequency resolution is significantly increased to a point spacing of 20 µT and 20 kHz in the experiment and 5 µT and $3.2357 \times 2\pi\,\mathrm{MHz}/128 \approx 159\,\mathrm{kHz}$ in the simulation. In return, only a small section focused around one neighboring constructive and destructive resonance is considered. This is plotted in Fig. 4.6 using the same structure as before in Fig. 4.5, where panels (a) and (b) show the transmission and panels (c) and (d) the spin pumping voltage. Experimentally obtained data is again depicted on the right in (b) and (d), while the results of the simulation are displayed on the left in (a) and (c).

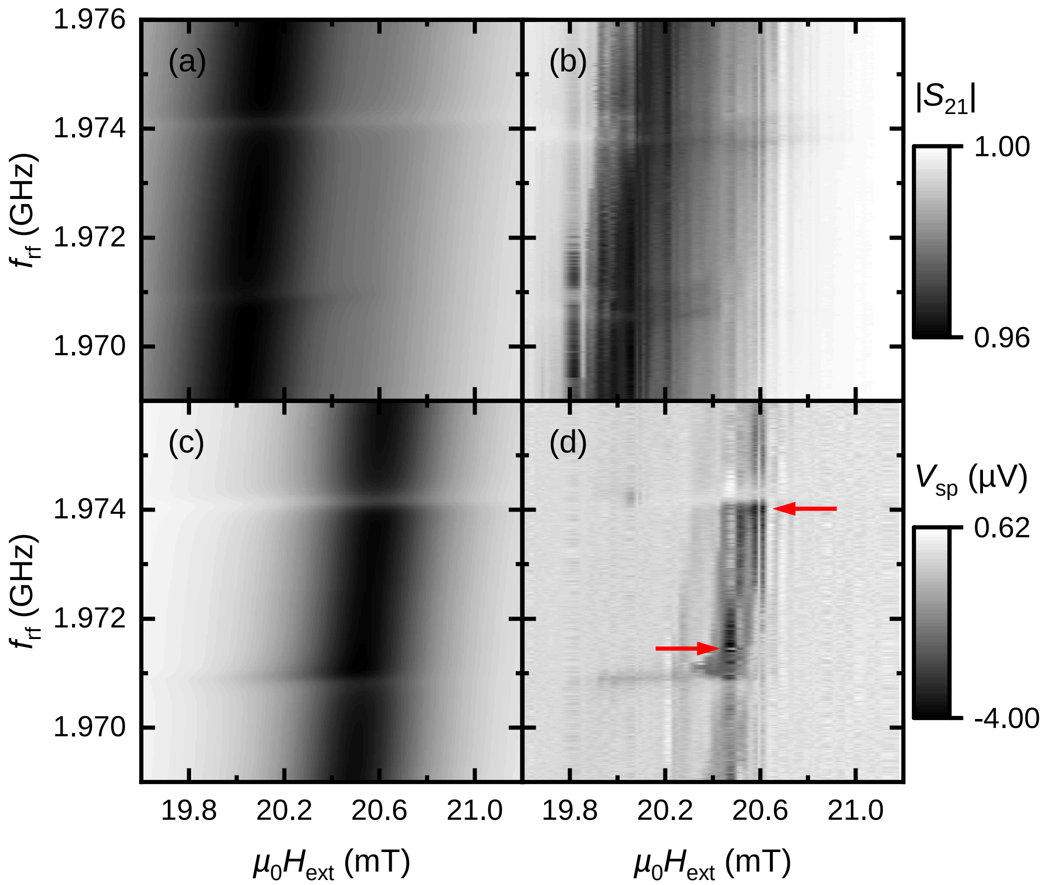

Figure 4.6: Zoom on a constructive and destructive magnon-phonon resonance pair. (a) and (b) show the transmission S_{21} parameter of the VNA and (c) and (d) the spin pumping voltage. They are plotted as a function of the external magnetic field $\mu_0 H_{\text{ext}}$ on the x-axis and the RF driving frequency f_{rf} on the y-axis. The left panels (a) and (c) display the results from the simulation, whereas the right panels (b) and (d) depict the experimentally obtained data. The color scales on the right belong to (b) and (d), respectively.

Figure 4.6 shows a destructive magnon-phonon interference at the bottom (at 1.9709 GHz) and a constructive at the top (at 1.9742 GHz). Especially the transmission measurement in Fig. 4.6 (b) has a smeared and blurred appearance, which can be explained by the fact that, with the chosen point spacing, we reach the resolution limit of our experimental setup. Nevertheless, the shape of the magnon-phonon resonance is more clearly visible than before in Fig. 4.5 and further details become apparent, especially in the spin pumping voltage in Fig. 4.6 (d). Furthermore, we observe that the spin pumping voltage is particularly large directly above the destructive and below the constructive interference, which appears in form of two dark black spots that are marked by the red arrows in Fig. 4.6 (d). We can also very nicely observe that the horizontal black line stemming from the destructive interference extends towards lower field amplitudes until about 19.9 mT, which is exactly when it reaches the FMR of the lower YIG film. This proves that there is indeed a transfer of angular momentum from the lower to the upper YIG layer due to the magnon-phonon coupling, which we observe by means of the spin pumping voltage. All in all, similar to before, we observe great qualitative agreement between experiment and simulation. Additionally, the linewidth of the FMR appears to be broader in the transmission measurements compared to the spin pumping voltage. This is first due to the fact that both YIG layers appear in the transmission, whereas only the upper layer contributes to the spin pumping. Second, the spin pumping voltage has a quadratic dependence on the magnitude of the perpendicular component of the magnetization, while the CPW FMR exhibits a linear dependence (see Eqs. (4.6) and (4.7)). This makes the amplitude decay faster in the spin pumping voltage.

We can also use Fig. 4.6 (d) for a rough estimate of the FMR linewidth in the range of 0.3 mT, extracted manually from the colorplot. This is still about one order of magnitude higher than the driving field amplitude (which was estimated as around 28 µT in Eq. (4.8)). We can therefore conclude that we operate well in the linear regime of ferromagnetic resonance. From this point of view, an increase of the RF driving power could be favorable in future experiments in order to increase the signal amplitude and thus improve the signal to noise ratio. But unfortunately, this is not possible with the used equipment, since the vector network analyzer was already operated at its upper output power limit.

4.4 Summary

In this chapter, the coupling between magnetic and acoustic excitations in a FMI|NMI|FMI trilayer was first described and modeled with a coupled system of equations of motion for the magnetization and lattice dynamics, as proposed by An *et al.* [An+20]. Qualitative relations were derived between the variables in the theory and the spin pumping voltage as well as the S_{21} transmission parameter of a VNA, which are the two observables in the conducted experiment. This allowed us to calculate and simulate theoretical expectations optimized for the system considered in the experiment. Those were then presented and discussed.

In the second part, the experimental setup and system of a YIG|GGG|YIG trilayer was introduced. We managed to find experimental evidence for the coupling between magnons and phonons in this system by (i) means of transmission measurements through a CPW and (ii) newly introduced voltage measurements via the spin pumping mechanism in a nanostructured Pt strip on top of the trilayer. Both were recorded simultaneously to compare between the techniques. While the latter allows us to focus only on the magnetization dynamics of one of the two YIG layers, since direct contact between the YIG and Pt is required, the transmission measurements are influenced by both layers, whereby the lower YIG layer strongly dominates due to its closer proximity. All in all, this gives us good and selective access to the magnetization dynamics of the lower layer (via transmission) and the upper layer (via spin pumping).

We could clearly differentiate between constructive and destructive magnon-phonon interferences and identify additional features in the data, such as e.g. a spin pumping voltage whose amplitude changes between high and low even far from the actual magnon-phonon resonances, according to their alternation between constructive and destructive interference. Generally speaking, the experimental observations were in good agreement with the simulation obtained from theory and existing literature [An+20; Bra+20].

Chapter 5

Summary

In this thesis, spin excitations in nanostructures were investigated via spin pumping, CPW FMR and all-electrical magnon transport measurements. In general, two different systems were probed. First, nonlinear spin pumping, parametric processes and the influence of FMR on magnon transport were studied. Second, the coupling between magnetic and acoustic excitations was considered in more detail.

In the first part of this thesis, entitled ***Microwave Control of Magnons***, we investigated magnon transport in a thin YIG film between two Pt strips, between which a Ru|Cu|Ta microstrip antenna was nanostructured. By considering only the DC spin pumping voltage induced in one of the two Pt strips around FMR, we managed to characterize the local properties of the YIG film. Furthermore, we succeeded in reaching a nonlinear regime of FMR and distinguishing it from the linear regime. The transition was indicated by a sudden increase of the resonance linewidth, a deformation of the lineshape and a premature saturation of the amplitude. In addition, parametric effects in the form of a sudden formation of a subsidiary resonance were observed at high powers. Both observations are in good agreement with existing literature. As a next step, we considered the whole structure and thus the magnon transport between the two Pt strips when an RF driving field was applied via the microstrip antenna. We report strong modulations of both the SHE and Joule heating induced magnon transport voltage around FMR, which were analyzed with respect to their power dependence and general shape. Since the amplitudes of the observed modulations were much too large, we suspected that they are most likely created by spurious effects, where a modulation of the spin pumping voltage via the Oersted field of the AC current on the injector Pt strip gives rise to lock-in signals.

In the second part, titled ***Magnon-Phonon Coupling***, we conducted for the first time broadband measurements on magnon-phonon coupling effects in a YIG|GGG|YIG trilayer. The results were obtained by simultaneous CPW FMR and spin pumping voltage measurements around FMR and agree very well with expectations from theory, simulations and other experiments, thus providing clear evidence for magnon-phonon coupling. Especially the newly introduced measurement of the spin pumping voltage allows us to focus on the dynamics of only one of the two YIG layers, where we still observe magnon-phonon coupling.

Chapter 6

Outlook

The results and achievements obtained in this work are not yet understood in every detail and thus far from shaping a complete picture. In regards to some aspects, they rather raise deeper questions instead and point to further possibilities for future research, some of which will be discussed in this chapter.

In the discussion of the microwave control of magnon transport experiments presented in Chapter 3, we have already frequently referred to issues that have not been finally clarified. One of these was the existence and origin of measurement artifacts (see Section 3.4.3), which could not be clearly shown with the measurements performed. However, there are some different and promising approaches with which this could be possible. Firstly, we suggested that the used lock-in amplifier plays a relevant role in the generation of the artifacts. Prospectively, one could try to use a different measurement technique that might not have the same issue. Here, we suggest the DC technique [Güc+20] as an alternative approach, as it is already shown to yield the same results in angular dependent all-electrical magnon transport experiments [Güc+20]. Another option would be measurements at low temperatures (e.g. 50 K), for which it is shown that the magnon transport voltages vanish because the magnon injection process requires thermal fluctuations [Goe+15; CSW16]. If the lock-in amplifier still measures a finite voltage around ferromagnetic resonance, it has to be generated by the spin pumping mechanism, which still works for low temperatures. Consequently, this would show the existence of measurement artifacts. A third option would be measurements with a bias-T, where we only use the microstrip antenna and one Pt strip. One would apply the RF current to the antenna in the same way as before, but now additionally add a low frequency quasi-DC voltage bias to the antenna with the bias-T. We measure the first and second harmonic voltage of the lock-in amplifier, which should ideally not pick up any signal since there is no magnon transport initiated. If we still observe a finite voltage around FMR, this would again show the existence of measurement artifacts stemming from the spin pumping mechanism. If the issue of measurement artifacts is solved, and a clean unaffected technique is found, one could finally investigate the changes in magnon transport during ferromagnetic resonance and parametric pumping around the subsidiary resonance.

Another aspect, in which improvements can still be made with respect to the experiments in Chapter 3, is the sample geometry and layout. As discussed before in Section 3.3.3, with the current design it is unfortunately **not** possible to distinguish between parallel and perpendicular pumping effects. Both are instead likely to play a relevant role in the experiments. Accordingly, an improvement of the sample layout that simplifies the RF driving field geometry is necessary. A conceivable concept that could be pursued in the future is that of an on-top antenna. Here, the two Pt strips are first sputtered onto the YIG film. In a second step, an insulating spacer layer is deposited over the entire surface, covering at the very least both Pt strips as well the gap in between them. In the last step, a wide antenna is structured on top of the insulator, which covers both Pt strips. It consequently generates an RF driving field with a strongly dominating in-plane component and thus the parallel pumping mechanism is favored. Perpendicular pumping effects should play **no** relevant role. Moreover, in this driving field configuration, it is shown that a magnon Bose–Einstein condensate (BEC) can be formed [Dem+06; Ser+14; Cla+15; Kre+18]. Its modulating influence on magnon transport can be expected to be particularly strong and interesting. In addition, this would allow comparison with the effects on magnon transport caused by DC current magnon pumping [Wim+19; Güc+20], thus providing insight into the microscopic processes at work there. In particular, more light could be shed on the work of Wimmer *et al.* [Wim+19], in which a zero damping state was achieved via DC current magnon pumping. This could possibly be explained by the generation of a magnon BEC, but Wimmer *et al.* [Wim+19] could not sufficiently verfiy this claim. Since the generation of a magnon BEC via parallel pumping is well established in literature, a comparison with future data could provide indirect evidence for the creation of a magnon BEC in Wimmer *et al.* [Wim+19].

As a bonus, the suggested layout massively simplifies the alignment requirements in the fabrication process, which is currently tedious and prone to errors, thus making fabrication more reliable in this regard. Also, the microstrip antenna would increase its width from 500 nm to around 2 or 3 µm, allowing for higher driving powers and making it less susceptible to electrostatic discharges, which were a big experimental obstacle and destroyed several structures before they could be measured.

To get to this new device layout, the first step is to find an insulating material that does **not** interfere with magnon transport in the YIG below. To this end, initial experiments have already been carried out with a total of three potential material candidates available in the ***SUPERBOWL*** (AlN, SiO_2) and ***ULTRADISK*** system (Si_3N_4). For this, several sets of two Pt strips at a distance of 500 nm or 1 µm were patterned onto a thin YIG film grown via PLD and then covered with one of the insulators, but **no** antenna was structured on top. Two different concepts were pursued, both of which can be seen in the exemplary section of a microscope image of the sample shown in Fig. 6.1. One approach was to completely cover the structures with the insulating spacer layer including the bonding pads (left in Fig. 6.1), the

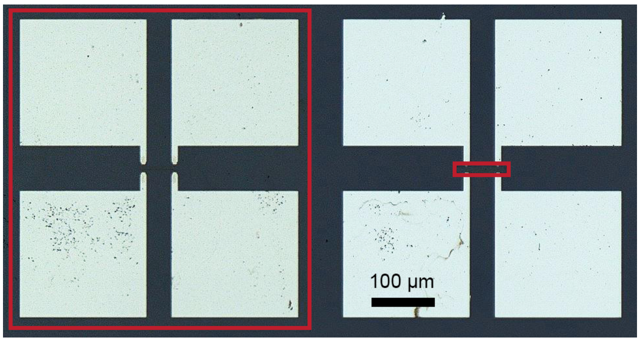

Figure 6.1: Microscope image of a section of the sample. The red squares indicate the areas covered by an insulating layer. On the left, the insulator covers the entire structure including the large square bonding pads, while on the right it covers only the thin Pt strips in the middle.

other was to cover only the two thin Pt strips in the middle (right in Fig. 6.1). Since no differences between the two concepts were found in the experiment, we do **not** distinguish between them in the following discussion.

The goal of the experiments was to detect changes in the amplitude of the magnon transport induced by the insulator layers. In this spirit, angular dependent all-electrical magnon transport experiments (see Section 2.7 and Section 3.4.1) were conducted using the DC measurement technique [Güc+20]. The results for the insulators aluminum nitride (AlN) and silicon dioxide (SiO_2) are shown in Fig. 6.2, together with an uncovered structure (labeled as "clean"). All data is already corrected by a voltage and an angle offset. The external magnetic field amplitude was fixed to 50 mT.

The third material used was silicon nitride (Si_3N_4). It is **not** depicted in Fig. 6.2 and **not** discussed further, as the layer later turned out to be slightly conducting, giving rise to a cross-resistance between the two Pt strips of around 2.6 MΩ and consequently rendering all measurements useless. This might be due to a **not** optimized sputtering process, where we are **not** entirely certain about the actual nature of the resulting material.

Figure 6.2 (a) and (b) show the SHE induced magnon transport voltage for an injector to detector distance of 500 nm and 1 µm, respectively. There, one can see that for both insulators we still observe a finite amplitude and the same cosine squared shape as in the uncovered case. However, for both insulators, the amplitude is reduced. An exception is the measurement for aluminum nitride in Fig. 6.2 (a), where the transport amplitude appears to be greatly magnified to almost twice as large as in the uncovered case. This is most likely some artifact, because this particular structure broke halfway through the displayed measurement. Generally,

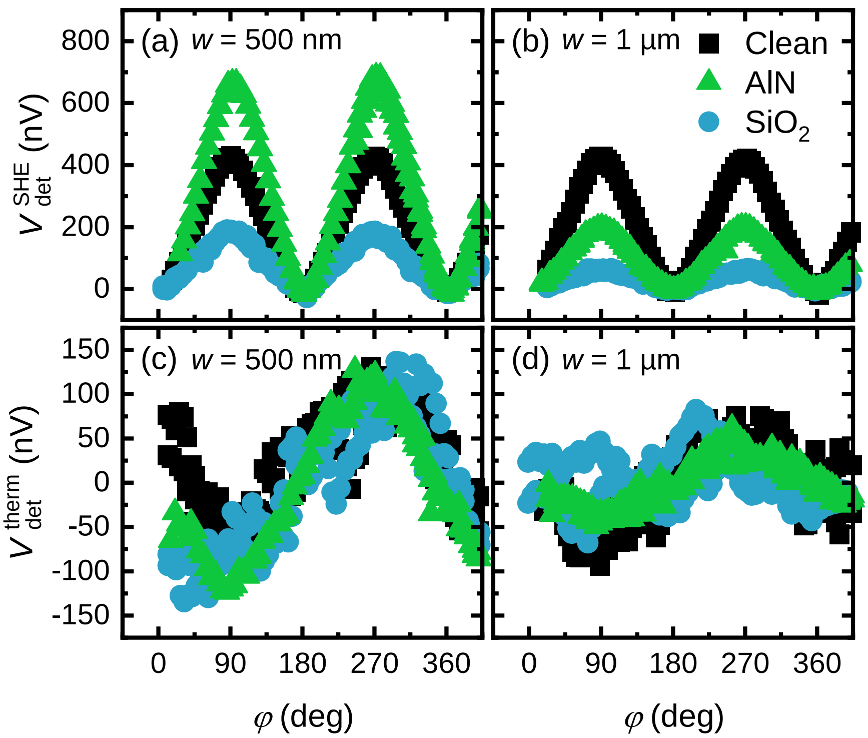

Figure 6.2: Angular dependent all-electrical magnon transport measurements for two Pt strip structures covered by various different insulators. The SHE transport voltages $V_{\mathrm{det}}^{\mathrm{SHE}}$ are shown on the upper panels (a) and (b), the Joule heating transport voltages $V_{\mathrm{det}}^{\mathrm{therm}}$ on the lower panels (c) and (d), both as a function of the angle φ between the orientation of the Pt strips and the external magnetic field of 50 mT amplitude. The left side depicts structures with an injector to detector distance of 500 nm, while the right side shows the data for a 1 µm gap.

silicon dioxide seems to reduce the magnon transport quite significantly, especially for the higher injector detector distance in Fig. 6.2 (b). Here, a reduction to about half of the amplitude of the uncovered case is visible for aluminum nitride, which seems more realistic than the amplification in Fig. 6.2 (a). All in all, aluminum nitride and silicon dioxide both show a reduced but still finite magnon transport amplitude. Out of all tested materials, aluminum nitride seems to be the most promising candidate for further investigation and application. It is also important to note that the effect of insulating layers on the all-electrical magnon transport signals has yet to be investigated. Presently, we can only speculate on the physical origin of the difference in signal reduction for the different materials.

The transport of Joule heating induced magnons is displayed in Fig. 6.2 (c) and (d). Its amplitude seems to be unaffected by the introduction of insulating layers for both the 500 nm and 1 µm injector detector distance. The only noticeable differ-

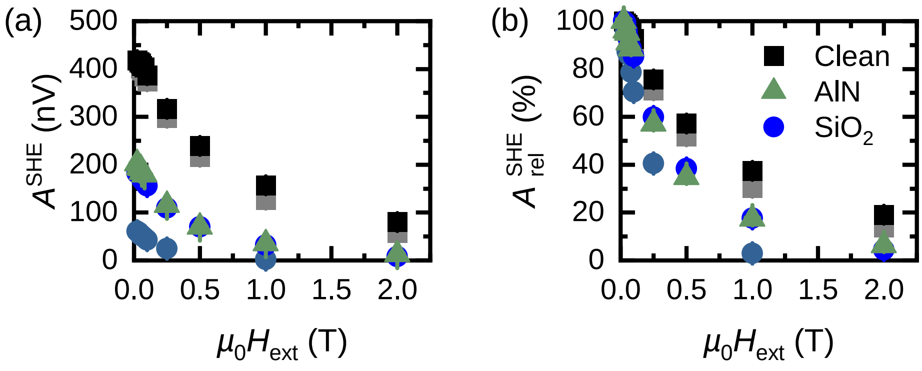

Figure 6.3: (a) Absolute SHE transport voltage amplitude A^{SHE} as a function of the external magnetic field $\mu_0 H_{\text{ext}}$. The various different materials are color and symbol coded in the same way as before in Fig. 6.2. The bright and bleached colors represent $w = 500\,\text{nm}$ and $1\,\mu\text{m}$ injector to detector distance, respectively. (b) Relative field amplitude $A^{\text{SHE}}_{\text{rel}}$ as a function of $\mu_0 H_{\text{ext}}$ in percent. For this, A^{SHE} was normalized to its value for an external magnetic field amplitude of 25 mT, i.e. its maximum.

ence is a voltage offset between the different materials, which can **not** be seen in Fig. 6.2 (c) and (d) because we have already corrected it there. Consequently, the field suppression is only analyzed for the SHE induced magnon transport and displayed in Fig. 6.3.

Figure 6.3 (a) shows the field dependence of the absolute transport amplitude for all measured materials and injector detector distances in a field range from 25 mT to 2 T. There, one can nicely see that the transport amplitudes of aluminum nitride with $w = 1\,\mu\text{m}$ aligns with the ones of silicon dioxide with $w = 500\,\text{nm}$, which further supports that aluminum nitride is the most promising candidate. We also clearly see that both insulating materials reduce the amplitude compared to the uncovered case. Since it is difficult to spot differences in the field suppression, we plot the relative field suppression in Fig. 6.3 (b). It is calculated as the transport amplitude normalized to its value for 25 mT external magnetic field amplitude, which means that the data points for each material and distance start at 100% at 25 mT. Two main observations are made here. Firstly, the field suppression is stronger in all cases covered with an insulating layer. This is especially clear at the highest measured field of 2 T, where we still find a finite amplitude in the uncovered case. But for all insulators, the SHE induced transport is suppressed to zero or below the noise level. Secondly, a higher injector to detector distance also seems to create a stronger field suppression.

We can only speculate about the reasons for the stronger suppression and the reduced SHE transport amplitude. The reasons can be manifold and accordingly we do **not** discuss them further here. A systematic analysis of the subject can be found in Cornelissen *et al.* [CW16], but with the simplification that no insulating spacer layers were used. Even in the simpler case of only two Pt strips considered there, the effects are complex and both the injection/detection of magnons at the Pt strips and their transport in the YIG are influenced by the magnetic field amplitude [CW16]. Consequently, a more detailed systematic investigation will be necessary to generate further insights. Nevertheless, these are promising results that lay an important foundation for the use of on-top antennas in future magnon transport experiments.

Besides suggestions on future improvements for the magnon transport experiments presented in Chapter 3, we provide an outlook on the future of the magnon-phonon coupling investigated in Chapter 4. There, the whole field is far from being entirely understood as well. An aspect that might be worth exploring is the low temperature regime. One can expect that the coupling is still present at low temperatures such as 50 K and both explored measurement techniques still function there. But subtle details such as e.g. the coupling strength might be temperature dependent. In this spirit, one could also measure a temperature series in the future in order to deduce a temperature dependence of relevant parameters. We already conducted a rough transmission measurement at a low temperature of 50 K, where the magnon-phonon resonances still seem to be present in the known form of horizontal strips in the CPW FMR signal. Since the resolution is quite bad, the measurement is neither shown here nor discussed further.

Another interesting quantity that could be studied in more detail in future experiments is the RF driving frequency and thus the dependence of the coupling strength on it. As proposed by theoretical calculations, the coupling strength is given by the magneto-elastic overlap integral between spin waves and acoustic waves [Bra+20], which is dependent on the frequency of the magnetization precession and consequently the RF driving frequency. In the theoretical considerations made in this thesis in Section 4.1.1, the overlap integral is represented as a simple factor $\Omega_{1/2}$, i.e. it is assumed to be constant over the frequency range considered. However, the coplanar waveguide based setup used in this thesis also allows to investigate a wide frequency spectrum. This would allow us to track the amplitude of the overlap integral and thus the coupling strength over a broad frequency interval in future experiments. Alternating disappearances and appearances of the magnon-phonon resonances would be the theoretically expected picture.

Moreover, in the spirit of this thesis, which has already explored a novel approach to magnon-phonon coupling with spin pumping mechanism, other new measurement methods could be applied. One example would be the Frequency-Resolved Magneto-Optic Kerr Effect (FR-MOKE) technique developed here at the Walther-Meißner-Institute [Lie+19]. With this, it is possible to optically detect the magnetization dynamics of selectively either the upper or lower YIG layer with additional lateral resolution. Also phase sensitive measurements could be done, providing a deeper insight into the details of the dynamics.

Last but not least, other experimental parameters can be varied and explored. There are various conceivable options and adjusting screws that can be turned here. Examples include different thicknesses of the top and bottom YIG layers or the use of materials other than YIG and GGG.

Appendix A

Fabrication

This chapter gives a quick summary of the fabrication processes used in this thesis. Since different fabrication techniques were used in Chapters 3 and 4, we begin this appendix with a discussion of the fabrication process used in Chapter 3.

Here, yttrium iron garnet (YIG, $Y_3Fe_5O_{12}$) thin films were first grown on a (100)-oriented gadolinium gallium garnet (GGG, $Gd_3Ga_5O_{12}$) substrate by pulsed laser deposition (PLD) at the Walther-Meißner-Institute. These are then cleaned in acetone and isopropanol for around two minutes each in an ultrasonic bath. Next, alignment markers are applied in the first lithography step. For this, the samples are spin coated with an electron beam resist and baked according to the respective recipe given in Table A.1. Thereafter, the sample is introduced into the nanobeam system, which uses electron beam lithography to write the desired nanostructures into the resist. Since yttrium iron garnet is an insulating material, a conductive resist must be applied on top of the actual one during each electron beam lithography process. This allows the charge and electrons to flow off the sample and thus prevents a deterioration of the writing process due to an electrical charging of the YIG film. Afterwards, the resist is developed and the sample then sputtered with around 45 nm of platinum (Pt) in the ***SUPERBOWL*** system at the Walther-Meißner-Institute. After that, a lift-off procedure is performed in warm acetone by blowing with a pipette and weak and short pulses in an ultrasonic bath. In the second process step, tiny platinum strips are structures onto the sample in the same way as before, but with different resist layers according to the "nanostructures" recipe in Table A.1. Microstrip antennas and bondpads are sputtered onto the sample in the third step using again electron beam lithography ("nanostructures" recipe in Table A.1) and a trilayer of ruthenium (Ru), copper (Cu) and tantalum (Ta). For the sample presented in Chapter 6, step one and two remain the same as before. In the third step, aluminum (Al) bondpads are deposited this time. After that, step by step, various insulation layers were applied using the corresponding recipe in Table A.1.

The sample used in Chapter 4 is based on a YIG film from a commercial supplier that was grown by liquid phase epitaxy (LPE) on a GGG substrate. The nanostructuring process was already done prior to this thesis in [Cös18]. It can be looked up there and is therefore not explained further here.

	alignment marks
resists	PMMA 600K
spin coating	60 s at 4000 rpm
baking	120 s at 170 °C
exposure dose	4.9 C/m^2
development	120 s in AR 600-56, rinse with IPA
	nanostructures
resists	PMMA 600K, PMMA 950K
spin coating	60 s at 4000 rpm, 60 s at 4000 rpm
baking	300 s at 170 °C, 300 s at 170 °C
exposure dose	5.8 C/m^2
development	120 s in AR 600-56, rinse twice with IPA
	insulating layers
resists	PMMA/MA 33%
spin coating	60 s at 4000 rpm
baking	120 s at 170 °C
exposure dose	4.2 C/m^2
development	120 s in AR 600-56, rinse with IPA
	conductive resist
resists	PMMA Electra 92
spin coating	60 s at 4000 rpm
baking	120 s at 90 °C
exposure dose	-
development	30 s in distilled water, rinse with distilled water

Table A.1: Process parameters of the electron beam lithography for various steps in the fabrication process.

Bibliography

[AAS11] K. Ando, T. An and E. Saitoh. 'Nonlinear spin pumping induced by parametric excitation'. In: *Applied Physics Letters* 99 (2011), p. 092510. DOI: 10.1063/1.3633348.

[Åke05] J. Åkerman. 'Toward a Universal Memory'. In: *Science* 308 (2005), pp. 508–510. DOI: 10.1126/science.1110549.

[Alt+13] M. Althammer, S. Meyer, H. Nakayama, M. Schreier, S. Altmannshofer, M. Weiler, H. Huebl, S. Geprägs, M. Opel, R. Gross, D. Meier, C. Klewe, T. Kuschel, J.-M. Schmalhorst, G. Reiss, L. Shen, A. Gupta, Y.-T. Chen, G. E. W. Bauer, E. Saitoh and S. T. B. Goennenwein. 'Quantitative study of the spin Hall magnetoresistance in ferromagnetic insulator/normal metal hybrids'. In: *Phys. Rev. B* 87 (2013), p. 224401. DOI: 10.1103/PhysRevB.87.224401.

[Alt18] M. Althammer. 'Pure spin currents in magnetically ordered insulator/normal metal heterostructures'. In: *Journal of Physics D: Applied Physics* 51 (2018), p. 313001. DOI: 10.1088/1361-6463/aaca89.

[An+04] S. Y. An, P. Krivosik, M. A. Kraemer, H. M. Olson, A. V. Nazarov and C. E. Patton. 'High power ferromagnetic resonance and spin wave instability processes in Permalloy thin films'. In: *Journal of Applied Physics* 96 (2004), pp. 1572–1580. DOI: 10.1063/1.1763996.

[An+20] K. An, A. N. Litvinenko, R. Kohno, A. A. Fuad, V. V. Naletov, L. Vila, U. Ebels, G. de Loubens, H. Hurdequint, N. Beaulieu, J. Ben Youssef, N. Vukadinovic, G. E. W. Bauer, A. N. Slavin, V. S. Tiberkevich and O. Klein. 'Coherent long-range transfer of angular momentum between magnon Kittel modes by phonons'. In: *Phys. Rev. B* 101 (2020), p. 060407. DOI: 10.1103/PhysRevB.101.060407.

[AYS09] K. Ando, T. Yoshino and E. Saitoh. 'Optimum condition for spin-current generation from magnetization precession in thin film systems'. In: *Applied Physics Letters* 94 (2009), p. 152509. DOI: 10.1063/1.3119314.

[Bau+15] H. G. Bauer, P. Majchrak, T. Kachel, C. H. Back and G. Woltersdorf. 'Nonlinear spin-wave excitations at low magnetic bias fields'. In: *Nature Communications* 6 (2015), p. 8274. DOI: 10.1038/ncomms9274.

[BD59] H. Bömmel and K. Dransfeld. 'Excitation of Hypersonic Waves by Ferromagnetic Resonance'. In: *Phys. Rev. Lett.* 3 (1959), pp. 83–84. DOI: 10.1103/PhysRevLett.3.83.

[Ber+18] A. J. Berger, E. R. J. Edwards, H. T. Nembach, A. D. Karenowska, M. Weiler and T. J. Silva. 'Inductive detection of fieldlike and dampinglike ac inverse spin-orbit torques in ferromagnet/normal-metal bilayers'. In: *Phys. Rev. B* 97 (2018), p. 094407. DOI: 10.1103/PhysRevB.97.094407.

[Ber96] L. Berger. 'Emission of spin waves by a magnetic multilayer traversed by a current'. In: *Phys. Rev. B* 54 (1996), pp. 9353–9358. DOI: 10.1103/PhysRevB.54.9353.

[BKO12] A. Brataas, A. D. Kent and H. Ohno. 'Current-induced torques in magnetic materials'. In: *Nature Materials* 11 (2012), pp. 372–381. DOI: 10.1038/nmat3311.

[BM65] H. S. Bennett and P. C. Martin. 'Spin Diffusion in the Heisenberg Paramagnet'. In: *Phys. Rev.* 138 (1965), A608–A617. DOI: 10.1103/PhysRev.138.A608.

[Bou+10] G. Bourianoff, M. Brillouet, R. K. Cavin, T. Hiramoto, J. A. Hutchby, A. M. Ionescu and K. Uchida. 'Nanoelectronics Research for Beyond CMOS Information Processing [Scanning the Issue]'. In: *Proceedings of the IEEE* 98 (2010), pp. 1986–1992. DOI: 10.1109/JPROC.2010.2077211.

[BPH17] T. Brächer, P. Pirro and B. Hillebrands. 'Parallel pumping for magnon spintronics: Amplification and manipulation of magnon spin currents on the micron-scale'. In: *Physics Reports* 699 (2017), pp. 1–34. DOI: 10.1016/j.physrep.2017.07.003.

[Bra+20] A. Brataas, B. van Wees, O. Klein, G. de Loubens and M. Viret. 'Spin insulatronics'. In: *Physics Reports* 885 (2020), pp. 1–27. DOI: 10.1016/j.physrep.2020.08.006.

[BSW12] G. E. W. Bauer, E. Saitoh and B. J. van Wees. 'Spin caloritronics'. In: *Nature Materials* 11 (2012), pp. 391–399. DOI: 10.1038/nmat3301.

[BT15] S. A. Bender and Y. Tserkovnyak. 'Interfacial spin and heat transfer between metals and magnetic insulators'. In: *Phys. Rev. B* 91 (2015), p. 140402. DOI: 10.1103/PhysRevB.91.140402.

[BW54] N. Bloembergen and S. Wang. 'Relaxation Effects in Para- and Ferromagnetic Resonance'. In: *Phys. Rev.* 93 (1954), pp. 72–83. DOI: 10.1103/PhysRev.93.72.

[Cas+12] V. Castel, N. Vlietstra, B. J. van Wees and J. Ben Youssef. 'Frequency and power dependence of spin-current emission by spin pumping in a thin-film YIG/Pt system'. In: *Phys. Rev. B* 86 (2012), p. 134419. DOI: 10.1103/PhysRevB.86.134419.

[Che+13] Y.-T. Chen, S. Takahashi, H. Nakayama, M. Althammer, S. T. B. Goennenwein, E. Saitoh and G. E. W. Bauer. 'Theory of spin Hall magnetoresistance'. In: *Phys. Rev. B* 87 (2013), p. 144411. DOI: 10.1103/PhysRevB.87.144411.

[Che+20] Y. Cheng, A. J. Lee, G. Wu, D. V. Pelekhov, P. C. Hammel and F. Yang. 'Nonlocal Uniform-Mode Ferromagnetic Resonance Spin Pumping'. In: *Nano Letters* 20 (2020), pp. 7257–7262. DOI: 10.1021/acs.nanolett.0c02640.

[Chu+12] A. V. Chumak, A. A. Serga, M. B. Jungfleisch, R. Neb, D. A. Bozhko, V. S. Tiberkevich and B. Hillebrands. 'Direct detection of magnon spin transport by the inverse spin Hall effect'. In: *Applied Physics Letters* 100 (2012), p. 082405. DOI: 10.1063/1.3689787.

[CKL93] V. Cherepanov, I. Kolokolov and V. L'vov. 'The Saga of YIG: Spectra, Thermodynamics, Interaction and Relaxation of Magnons in a Complex Magnet'. Physics reports. North-Holland, 1993.

[Cla+15] P. Clausen, D. A. Bozhko, V. I. Vasyuchka, B. Hillebrands, G. A. Melkov and A. A. Serga. 'Stimulated thermalization of a parametrically driven magnon gas as a prerequisite for Bose-Einstein magnon condensation'. In: *Phys. Rev. B* 91 (2015), p. 220402. DOI: 10.1103/PhysRevB.91.220402.

[Cor+15] L. J. Cornelissen, J. Liu, R. A. Duine, J. Ben Youssef and B. J. van Wees. 'Long-distance transport of magnon spin information in a magnetic insulator at room temperature'. In: *Nature Physics* 11 (2015), pp. 1022–1026. DOI: 10.1038/nphys3465.

[Cor+18] L. J. Cornelissen, J. Liu, B. J. van Wees and R. A. Duine. 'Spin-Current-Controlled Modulation of the Magnon Spin Conductance in a Three-Terminal Magnon Transistor'. In: *Phys. Rev. Lett.* 120 (2018), p. 097702. DOI: 10.1103/PhysRevLett.120.097702.

[Cös18] B. Cöster. 'Analysis of pure spin current transport in yttrium iron garnet|normal metal heterostructures'. Masterthesis. Technische Universität München, 2018.

[CP] M. Chen and C. E. Patton. 'Spin Wave Instability Processes in Ferrites'. In: *Nonlinear Phenomena and Chaos in Magnetic Materials*, pp. 33–82. DOI: 10.1142/9789814355810_0003.

[Cro+91] R. W. Cross, C. E. Patton, G. Srinivasan, J. G. Booth and M. Chen. 'Anomalous low-frequency butterfly curves for subsidiary and ferromagnetic resonance overlap at 3 GHz'. In: *Journal of Applied Physics* 69 (1991), pp. 1569–1573. DOI: 10.1063/1.347251.

[CSW16] L. J. Cornelissen, J. Shan and B. J. van Wees. 'Temperature dependence of the magnon spin diffusion length and magnon spin conductivity in the magnetic insulator yttrium iron garnet'. In: *Phys. Rev. B* 94 (2016), p. 180402. DOI: 10.1103/PhysRevB.94.180402.

[CW16] L. J. Cornelissen and B. J. van Wees. 'Magnetic field dependence of the magnon spin diffusion length in the magnetic insulator yttrium iron garnet'. In: *Phys. Rev. B* 93 (2016), p. 020403. DOI: 10.1103/PhysRevB.93.020403.

[Cze+11] F. D. Czeschka, L. Dreher, M. S. Brandt, M. Weiler, M. Althammer, I.-M. Imort, G. Reiss, A. Thomas, W. Schoch, W. Limmer, H. Huebl, R. Gross and S. T. B. Goennenwein. 'Scaling Behavior of the Spin Pumping Effect in Ferromagnet-Platinum Bilayers'. In: *Phys. Rev. Lett.* 107 (2011), p. 046601. DOI: 10.1103/PhysRevLett.107.046601.

[Cze11] F. D. Czeschka. 'Spin Currents in Metallic Nanostructures'. PhD thesis. Technische Universität München, 2011.

[Dam53] R. W. Damon. 'Relaxation Effects in the Ferromagnetic Resonance'. In: *Rev. Mod. Phys.* 25 (1953), pp. 239–245. DOI: 10.1103/RevModPhys.25.239.

[Dem+06] S. O. Demokritov, V. E. Demidov, O. Dzyapko, G. A. Melkov, B. Hillebrands and A. N. Slavin. 'Bose-Einstein condensation of quasi-equilibrium magnons at room temperature under pumping'. In: *Nature* 443 (2006), pp. 430–433. DOI: 10.1038/nature05117.

[Dub+17] C. Dubs, O. Surzhenko, R. Linke, A. Danilewsky, U. Brückner and J. Dellith. 'Sub-micrometer yttrium iron garnet LPE films with low ferromagnetic resonance losses'. In: *Journal of Physics D: Applied Physics* 50 (2017), p. 204005. DOI: 10.1088/1361-6463/aa6b1c.

[Dus+19] S. Dushenko, Y. Ando, T. Shinjo and M. Shiraishi. 'Ferromagnetic resonance imbalance at high microwave power: Effect on the Gilbert damping parameter'. In: *Journal of Applied Physics* 126 (2019), p. 203904. DOI: 10.1063/1.5127882.

[Far31] M. Faraday. 'XVII. On a peculiar class of acoustical figures; and on certain forms assumed by groups of particles upon vibrating elastic surfaces'. In: *Philosophical Transactions of the Royal Society of London* 121 (1831), pp. 299–340. DOI: 10.1098/rstl.1831.0018.

[Fla18] L. Flacke. 'Spin-Pumping and Spin Wave Damping in Co25Fe75 Thin-Film Heterostructures'. Masterthesis. Technische Universität München, 2018.

[Gan+16] K. Ganzhorn, S. Klingler, T. Wimmer, S. Geprägs, R. Gross, H. Huebl and S. T. B. Goennenwein. 'Magnon-based logic in a multi-terminal YIG/Pt nanostructure'. In: *Applied Physics Letters* 109 (2016), p. 022405. DOI: 10.1063/1.4958893.

[Gil04] T. L. Gilbert. 'A phenomenological theory of damping in ferromagnetic materials'. In: *IEEE Transactions on Magnetics* 40 (2004), pp. 3443–3449. DOI: 10.1109/TMAG.2004.836740.

[GM18] R. Gross and A. Marx. 'Festkörperphysik'. De Gruyter, 2018. DOI: doi:10.1515/9783110559187.

[Goe+15] S. T. B. Goennenwein, R. Schlitz, M. Pernpeintner, K. Ganzhorn, M. Althammer, R. Gross and H. Huebl. 'Non-local magnetoresistance in YIG/Pt nanostructures'. In: *Applied Physics Letters* 107 (2015), p. 172405. DOI: 10.1063/1.4935074.

[Goe01] J. W. Goethe. 'Faust, Der Tragödie Erster Teil'. Reclam, Ditzingen, 2001. ISBN: 978-3-15-000001-4.

[Güc+20] J. Gückelhorn, T. Wimmer, S. Geprägs, H. Huebl, R. Gross and M. Althammer. 'Quantitative comparison of magnon transport experiments in three-terminal YIG/Pt nanostructures acquired via dc and ac detection techniques'. In: *Applied Physics Letters* 117 (2020), p. 182401. DOI: 10.1063/5.0023307.

[Har+11] K. Harii, T. An, Y. Kajiwara, K. Ando, H. Nakayama, T. Yoshino and E. Saitoh. 'Frequency dependence of spin pumping in Pt/Y3Fe5O12 film'. In: *Journal of Applied Physics* 109 (2011), p. 116105. DOI: 10.1063/1.3594661.

[Hen+73] R. Henry, P. Besser, D. Heinz and J. Mee. 'Ferromagnetic resonance properties of LPE YIG films'. In: *IEEE Transactions on Magnetics* 9 (1973), pp. 535–537. DOI: 10.1109/TMAG.1973.1067610.

[Hir+20] A. Hirohata, K. Yamada, Y. Nakatani, I.-L. Prejbeanu, B. Diény, P. Pirro and B. Hillebrands. 'Review on spintronics: Principles and device applications'. In: *Journal of Magnetism and Magnetic Materials* 509 (2020), p. 166711. DOI: 10.1016/j.jmmm.2020.166711.

[Hir99] J. E. Hirsch. 'Spin Hall Effect'. In: *Phys. Rev. Lett.* 83 (1999), pp. 1834–1837. DOI: 10.1103/PhysRevLett.83.1834.

[HP40] T. Holstein and H. Primakoff. 'Field Dependence of the Intrinsic Domain Magnetization of a Ferromagnet'. In: *Phys. Rev.* 58 (1940), pp. 1098–1113. DOI: 10.1103/PhysRev.58.1098.

[HRT74] P. Hansen, P. Röschmann and W. Tolksdorf. 'Saturation magnetization of gallium-substituted yttrium iron garnet'. In: *Journal of Applied Physics* 45 (1974), pp. 2728–2732. DOI: 10.1063/1.1663657.

[IBM] IBM. *IBM 350 disk storage unit.* https://www.ibm.com/ibm/history/exhibits/storage/storage_350.html.

[Igu+12] R. Iguchil, K. Ando, T. An, E. Saitoh and T. Sato. 'Evaluation of Nonlinear Effect in High Power Spin Pumping in Polycrystalline Bi-Substituted Yttrium Iron Garnet (Bi:YIG)/Pt Bilayer Structure'. In: *IEEE Transactions on Magnetics* 48 (2012), pp. 3051–3053. DOI: 10.1109/TMAG.2012.2202382.

[JWO15] T. Jungwirth, J. Wunderlich and K. Olejník. 'Spin Hall effect devices'. In: *Nature Materials* 11 (2015), pp. 382–390. DOI: 10.1038/nmat3279.

[Kar21] E. Karadža. 'Disentangling Electrical and Thermal Modulations of Magnon Conductivity in Yttrium Iron Garnet'. Masterthesis. Technische Universität München, 2021.

[Kar54] O. Karlqvist. 'Calculation of the magnetic field in the ferromagnetic layer of a magnetic drum'. Henrik Lindståhls Bokhandel i Distribution, 1954.

[Khi+18] Y. V. Khivintsev, V. K. Sakharov, S. L. Vysotskii, Y. A. Filimonov, A. I. Stognii and S. A. Nikitov. 'Magnetoelastic Waves in Submicron Yttrium–Iron Garnet Films Manufactured by Means of Ion-Beam Sputtering onto Gadolinium–Gallium Garnet Substrates'. In: *Technical Physics* 63 (2018), pp. 1029–1035. DOI: 10.1134/S1063784218070162.

[Kit48] C. Kittel. 'On the Theory of Ferromagnetic Resonance Absorption'. In: *Phys. Rev.* 73 (1948), pp. 155–161. DOI: 10.1103/PhysRev.73.155.

[Kit58] C. Kittel. 'Interaction of Spin Waves and Ultrasonic Waves in Ferromagnetic Crystals'. In: *Phys. Rev.* 110 (1958), pp. 836–841. DOI: 10.1103/PhysRev.110.836.

[Kli+14] S. Klingler, A. V. Chumak, T. Mewes, B. Khodadadi, C. Mewes, C. Dubs, O. Surzhenko, B. Hillebrands and A. Conca. 'Measurements of the exchange stiffness of YIG films using broadband ferromagnetic resonance techniques'. In: *Journal of Physics D: Applied Physics* 48 (2014), p. 015001. DOI: 10.1088/0022-3727/48/1/015001.

[Kli+17] S. Klingler, H. Maier-Flaig, C. Dubs, O. Surzhenko, R. Gross, H. Huebl, S. T. B. Goennenwein and M. Weiler. 'Gilbert damping of magnetostatic modes in a yttrium iron garnet sphere'. In: *Applied Physics Letters* 110 (2017), p. 092409. DOI: 10.1063/1.4977423.

[KM63] L. P. Kadanoff and P. C. Martin. 'Hydrodynamic equations and correlation functions'. In: *Annals of Physics* 24 (1963), pp. 419–469. DOI: 10.1016/0003-4916(63)90078-2.

[KP10] P. Krivosik and C. E. Patton. 'Hamiltonian formulation of nonlinear spin-wave dynamics: Theory and applications'. In: *Phys. Rev. B* 82 (2010), p. 184428. DOI: 10.1103/PhysRevB.82.184428.

[Kre+18] A. J. E. Kreil, D. A. Bozhko, H. Y. Musiienko-Shmarova, V. I. Vasyuchka, V. S. L'vov, A. Pomyalov, B. Hillebrands and A. A. Serga. 'From Kinetic Instability to Bose-Einstein Condensation and Magnon Supercurrents'. In: *Phys. Rev. Lett.* 121 (2018), p. 077203. DOI: 10.1103/PhysRevLett.121.077203.

[KS86] B. A. Kalinikos and A. N. Slavin. 'Theory of dipole-exchange spin wave spectrum for ferromagnetic films with mixed exchange boundary conditions'. In: *Journal of Physics C: Solid State Physics* 19 (1986), pp. 7013–7033. DOI: 10.1088/0022-3719/19/35/014.

[LB29] H. P. Lovecraft and Z. Bishop. 'Weird Tales: The Unique Magazine'. Indianapolis, IN: Weird Tales Magazine (Pulp), 1st Edition, 1929.

[LG67] I. J. Lowe and S. Gade. 'Density-Matrix Derivation of the Spin-Diffusion Equation'. In: *Phys. Rev.* 156 (1967), pp. 817–825. DOI: 10.1103/PhysRev.156.817.

[Lie+19] L. Liensberger, L. Flacke, D. Rogerson, M. Althammer, R. Gross and M. Weiler. 'Spin-wave propagation in metallic CoFe films determined by microfocused frequency-resolved magneto-optic Kerr effect'. In: *IEEE Magnetics Letters* PP (2019), pp. 1–1. DOI: 10.1109/LMAG.2019.2918755.

[Liu+19] J. Liu, F. Feringa, B. Flebus, L. J. Cornelissen, J. C. Leutenantsmeyer, R. A. Duine and B. J. van Wees. 'Microwave control of thermal-magnon spin transport'. In: *Phys. Rev. B* 99 (2019), p. 054420. DOI: 10.1103/PhysRevB.99.054420.

[LL65] L. D. Landau and E. M. Lifshitz. 'On the Theory of the Dispersion of Magnetic Permeability in Ferromagnetic Bodies'. In: *Collected Papers of L.D. Landau*. Ed. by Ter Haar. Pergamon, 1965, pp. 101–114. ISBN: 978-0-08-010586-4. DOI: 10.1016/B978-0-08-010586-4.50023-7.

[Lou16] P. D. Louis. 'Broadband-Spectroscopy of Magnetic Materials at Low Temperatures'. Masterthesis. Technische Universität München, 2016.

[Lov] H. P. Lovecraft. *The Curse of Yig*. https://www.hplovecraft.com/writings/texts/fiction/cy.aspx.

[LSP58] R. C. LeCraw, E. G. Spencer and C. S. Porter. 'Ferromagnetic Resonance and Nonlinear Effects in Yttrium Iron Garnet'. In: *Journal of Applied Physics* 29 (1958), pp. 326–327. DOI: 10.1063/1.1723119.

[Lus+15] J. Lustikova, Y. Shiomi, Y. Handa and E. Saitoh. 'Spectral shape deformation in inverse spin Hall voltage in Y3Fe5O12|Pt bilayers at high microwave power levels'. In: *Journal of Applied Physics* 117 (2015), p. 073901. DOI: 10.1063/1.4908211.

[Mai+17] H. Maier-Flaig, S. Klingler, C. Dubs, O. Surzhenko, R. Gross, M. Weiler, H. Huebl and S. T. B. Goennenwein. 'Temperature-dependent magnetic damping of yttrium iron garnet spheres'. In: *Phys. Rev. B* 95 (2017), p. 214423. DOI: 10.1103/PhysRevB.95.214423.

[MD66] R. Moskowitz and E. Della Torre. 'Theoretical aspects of demagnetization tensors'. In: *IEEE Transactions on Magnetics* 2 (1966), pp. 739–744. DOI: 10.1109/TMAG.1966.1065973.

[Moo06] G. E. Moore. 'Cramming more components onto integrated circuits'. In: *IEEE Solid-State Circuits Society Newsletter* 11 (2006), pp. 33–35. DOI: 10.1109/N-SSC.2006.4785860.

[Mos+10] O. Mosendz, J. E. Pearson, F. Y. Fradin, G. E. W. Bauer, S. D. Bader and A. Hoffmann. 'Quantifying Spin Hall Angles from Spin Pumping: Experiments and Theory'. In: *Phys. Rev. Lett.* 104 (2010), p. 046601. DOI: 10.1103/PhysRevLett.104.046601.

[MP20] I. S. Maksymov and A. Pototsky. 'Excitation of Faraday-like body waves in vibrated living earthworms'. In: *Scientific Reports* 10 (2020). DOI: 10.1038/s41598-020-65295-4.

[Mül+21] M. Müller, L. Liensberger, L. Flacke, H. Huebl, A. Kamra, W. Belzig, R. Gross, M. Weiler and M. Althammer. 'Temperature-Dependent Spin Transport and Current-Induced Torques in Superconductor-Ferromagnet Heterostructures'. In: *Phys. Rev. Lett.* 126 (2021), p. 087201. DOI: 10.1103/PhysRevLett.126.087201.

[Mül19] M. Müller. 'Superconductor/Ferromagnet Heterostructures for Superconducting Spintronics'. Masterthesis. Technische Universität München, 2019.

[Noa+19] T. B. Noack, V. I. Vasyuchka, D. A. Bozhko, B. Heinz, P. Frey, D. V. Slobodianiuk, O. V. Prokopenko, G. A. Melkov, P. Kopietz, B. Hillebrands and A. A. Serga. 'Enhancement of the Spin Pumping Effect by Magnon Confluence Process in YIG/Pt Bilayers'. In: *physica status solidi (b)* 256 (2019), p. 1900121. DOI: 10.1002/pssb.201900121.

[Ols+07] H. M. Olson, P. Krivosik, K. Srinivasan and C. E. Patton. 'Ferromagnetic resonance saturation and second order Suhl spin wave instability processes in thin Permalloy films'. In: *Journal of Applied Physics* 102 (2007), p. 023904. DOI: 10.1063/1.2756481.

[Ori] OriginLab Corporation, Northampton, MA, USA. *OriginPro, Version 2020.*

[Pol49] D. Polder. 'VIII. On the theory of ferromagnetic resonance'. In: *The London, Edinburgh, and Dublin Philosophical Magazine and Journal of Science* 40 (1949), pp. 99–115. DOI: 10.1080/14786444908561215.

[RA90] S. M. Rezende and F. M. de Aguiar. 'Spin-wave instabilities, auto-oscillations, and chaos in yttrium-iron-garnet'. In: *Proceedings of the IEEE* 78 (1990), pp. 893–908. DOI: 10.1109/5.56906.

[Ros60] F. C. Rossol. 'Subsidiary Resonance in the Coincidence Region in Yttrium Iron Garnet'. In: *Journal of Applied Physics* 31 (1960), pp. 2273–2275. DOI: 10.1063/1.1735536.

[San+11] C. W. Sandweg, Y. Kajiwara, A. V. Chumak, A. A. Serga, V. I. Vasyuchka, M. B. Jungfleisch, E. Saitoh and B. Hillebrands. 'Spin Pumping by Parametrically Excited Exchange Magnons'. In: *Phys. Rev. Lett.* 106 (2011), p. 216601. DOI: 10.1103/PhysRevLett.106.216601.

[Ser+14] A. A. Serga, V. S. Tiberkevich, C. W. Sandweg, V. I. Vasyuchka, D. A. Bozhko, A. V. Chumak, T. Neumann, B. Obry, G. A. Melkov, A. N. Slavin and B. Hillebrands. 'Bose-Einstein condensation in an ultra-hot gas of pumped magnons'. In: *Nature Communications* 5 (2014), pp. 2041–1723. DOI: 10.1038/ncomms4452.

[Sil+16] T. J. Silva, H. T. Nembach, J. M. Shaw, B. Doyle, K. Oguz, K. O'brien and M. Doczy. 'Metrology and Diagnostic Techniques for Nanoelectronics'. Ed. by Z. Ma and D. G. Seiler. Jenny Stanford Publishing, 2016. ISBN: 9789814745086.

[SKB18] S. Streib, H. Keshtgar and G. E. W. Bauer. 'Damping of Magnetization Dynamics by Phonon Pumping'. In: *Phys. Rev. Lett.* 121 (2018), p. 027202. DOI: 10.1103/PhysRevLett.121.027202.

[Slo89] J. C. Slonczewski. 'Conductance and exchange coupling of two ferromagnets separated by a tunneling barrier'. In: *Phys. Rev. B* 39 (1989), pp. 6995–7002. DOI: 10.1103/PhysRevB.39.6995.

[SLP58] E. G. Spencer, R. C. LeCraw and C. S. Porter. 'Ferromagnetic Resonance in Yttrium Iron Garnet at Low Frequencies'. In: *Journal of Applied Physics* 29 (1958), pp. 429–430. DOI: 10.1063/1.1723168.

[Spa64] M. Sparks. 'Ferromagnetic-Relaxation Theory'. McGraw-Hill Book Company, New York, 1964.

[Sta93] D. D. Stancil. 'Theory of Magnetostatic Waves'. Springer-Verlag New York, 1993. ISBN: 978-1-4613-9338-2. DOI: 10.1007/978-1-4613-9338-2.

[Str+19] S. Streib, N. Vidal-Silva, K. Shen and G. E. W. Bauer. 'Magnon-phonon interactions in magnetic insulators'. In: *Phys. Rev. B* 99 (2019), p. 184442. DOI: 10.1103/PhysRevB.99.184442.

[Suh57] H. Suhl. 'The theory of ferromagnetic resonance at high signal powers'. In: *Journal of Physics and Chemistry of Solids* 1 (1957), pp. 209–227. DOI: 10.1016/0022-3697(57)90010-0.

[Sun+12] Y. Sun, Y.-Y. Song, H. Chang, M. Kabatek, M. Jantz, W. Schneider, M. Wu, H. Schultheiss and A. Hoffmann. 'Growth and ferromagnetic resonance properties of nanometer-thick yttrium iron garnet films'. In: *Applied Physics Letters* 101 (2012), p. 152405. DOI: 10.1063/1.4759039.

[TBB02a] Y. Tserkovnyak, A. Brataas and G. E. W. Bauer. 'Enhanced Gilbert Damping in Thin Ferromagnetic Films'. In: *Phys. Rev. Lett.* 88 (2002), p. 117601. DOI: 10.1103/PhysRevLett.88.117601.

[TBB02b] Y. Tserkovnyak, A. Brataas and G. E. W. Bauer. 'Spin pumping and magnetization dynamics in metallic multilayers'. In: *Phys. Rev. B* 66 (2002), p. 224403. DOI: 10.1103/PhysRevB.66.224403.

[Uch+10] K. Uchida, J. Xiao, H. Adachi, J. Ohe, S. Takahashi, J. Ieda, T. Ota, Y. Kajiwara, H. Umezawa, H. Kawai, G. E. W. Bauer, S. Maekawa and E. Saitoh. 'Spin Seebeck insulator'. In: *Nature Materials* 9 (2010), pp. 894–897. DOI: 10.1038/nmat2856.

[Wal16] M. Mitchell Waldrop. 'The chips are down for Moore's law'. In: *Nature* 530 (2016), pp. 144–147. DOI: 10.1038/530144a.

[Wim+19] T. Wimmer, M. Althammer, L. Liensberger, N. Vlietstra, S. Geprägs, M. Weiler, R. Gross and H. Huebl. 'Spin Transport in a Magnetic Insulator with Zero Effective Damping'. In: *Phys. Rev. Lett.* 123 (2019), p. 257201. DOI: 10.1103/PhysRevLett.123.257201.

[Wim16] T. Wimmer. 'Spin Transport in Magnetic Nanostructures'. Masterthesis. Technische Universität München, 2016.

[Wim21] T. Wimmer. 'Controlling Magnonic Spin Currents in Magnetic Insulators'. PhD thesis. Technische Universität München, 2021.

[Wol] Wolfram Research, Inc. *Mathematica, Version 12.1.*

[Xia+10] J. Xiao, G. E. W. Bauer, K.-C. Uchida, E. Saitoh and S. Maekawa. 'Theory of magnon-driven spin Seebeck effect'. In: *Phys. Rev. B* 81 (2010), p. 214418. DOI: 10.1103/PhysRevB.81.214418.

[YD91] M. Ye and H. Dötsch. 'Magnetoelastic instabilities in the ferrimagnetic resonance of magnetic garnet films'. In: *Phys. Rev. B* 44 (1991), pp. 9458–9466. DOI: 10.1103/PhysRevB.44.9458.

[Zho+16] H. Zhou, X. Fan, L. Ma, L. Cui, C. Jia, S. Zhou, Y. S. Gui, C.-M. Hu and D. Xue. 'Spin pumping in the nonlinear dynamic regime of a Pt/Y3Fe5O12 heterostructure'. In: *Applied Physics Letters* 108 (2016), p. 192408. DOI: 10.1063/1.4949555.

Acknowledgements
Danksagung

Das letzte Jahr war für uns alle speziell und damit auch besonders. Ein Jahr, wie es sicher noch niemand von uns erlebte. Ein Jahr, das jeden einzelnen und uns alle gemeinsam vor große Herausforderungen stellte. Ein Jahr im Zeichen der Pandemie; einer Krise, die uns wohl noch einige Zeit begleiten wird. Ein Jahr, in dem wir uns verändern und unseren Blick auf die Welt neu justieren mussten. Und ein Jahr, in dem die Fähigkeit eine große Rolle spielte, Neues zu erdenken und die Welt in einer Art und Weise zu betrachten, wie es noch nie jemand zuvor getan hat. Zwei Qualitäten, die man auch in der Wissenschaft benötigt. Und so kam es, dass das letzte Jahr noch zusätzlicher in einem weiteren Aspekt besonders für mich war: Ich durfte meine wissenschaftliche Grundausbildung hier am Walther-Meißner-Institut mit meiner Masterarbeit abschließen, und mich so nicht nur privat, sondern auch professionell diesen Qualitäten verschreiben. Ich hoffe, mir ist das in zufriedenstellender Art und Weise gelungen. In jedem Fall möchte ich mich für die wunderbare Zeit und die wundervollen Dinge bedanken, die ich hier erleben und erlernen durfte. Ich habe viel über mich und die Welt erfahren. Im Speziellen gilt mein Dank:

- **Prof. Dr. Rudolf Gross** zuvörderst für das Vertrauen und die Möglichkeit, meine Masterarbeit hier am Walther-Meißner-Institut anfertigen zu dürften.
- **Dr. Matthias Althammer**, der meine Faszination für dieses Themenfeld in seinen Vorlesungen wecken konnte. Und für das Angebot, dieser Faszination in Form einer Masterarbeit nachgehen zu dürfen. Außerdem für die vielen Stunden, in denen du mir ausführlich und geduldig Fragen beantwortest und mir im Labor geholfen hast. Und natürlich für das coole Thema, das ich mit dieser Arbeit bearbeiten durfte.
- **Priv. Doz. Dr. Hans Hübl** für die Betreuung des Abschnitts über die Magnon-Phonon-Kopplung und die vielen weiteren hervorragenden Anmerkungen. Beim Start der Masterarbeit hatte ich nicht erwartet, nach meiner Bachelorarbeit bei dir, dass ich auch hier bei dir landen würde.
- **Dr. Matthias Opel** und **Dr. Stephan Geprägs** für die reichlichen und vielfältigen Fragen, Beiträge und Anregungen im allwöchentlichen DC-Meeting.
- **Tobias Wimmer**, meinem Betreuer, für die vielen Stunden, die du investiert hast. Für die vielen Fragen, die du mir mit großer Geduld, sehr gutem Verständnis der Materie und abgrundartiger Tiefe beantworten konntest. Auch

wenn ich sozusagen in deinen letzten Zügen als PhD Student angefangen habe, hoffe ich, dass ich trotzdem meinen Teil zu deiner Arbeit beitragen konnte.

- **Janine Gückelhorn** für die enorm viele Zeit, die du in meine Betreuung investiert hast. Und das obwohl du nicht einmal von meiner Arbeit für die deine profitierst. Vieles, was ich im Bereich Fabrikation und Experiment weiß, habe ich vor dir gelernt. Und natürlich weiterhin Danke für die vielen hochqualitativen YIG-Filme, die du für mich hergestellt hast und ohne die nicht einmal ein einziges meiner Experimente möglich wäre. Möge der Allvater der Schlangen mit dir sein!

- **Manuel Müller**, für dich gilt selbstverständlich vieles von dem, was ich oben bereits bei Janine erwähnt hatte. Danke vor allem für die viele große Hilfe beim Sputtern verschiedener Materialen und bei den FMR Messungen. Deine Expertise im Bereich der Fertigung und der FMR Messungen half mir ungemein weiter. Außerdem vielen Dank für die FMR-Charakterisierung der YIG-Filme. Auch mit dir möge der Allvater der Schlangen sein!

- **Luis Flacke** für die Hilfe mit der SUPERBOWL und die kurze Betreuung für ein paar Messungen, die letztendlich leider nicht von Erfolg gekrönt wurden. Außerdem für die moralische Unterstützung, die nötig war, um an jenem denkwürdigen Abend den Double-Triple-Burger in guter Nährungen vollständig zu verdrücken.

- **Thomas Luschmann** für die extrem kompetente Hilfe und Lösung der Probleme mit der Nanobeam. Außerdem für die fast allmittaglichen Spezi-Pausen, die ich stets sehr genossen habe.

- **Lukas Liensberger** für die Expertise zur weiteren Untersuchen der Magnon-Phonon-Kopplung und Hilfe in diesem Bereich.

- **Christopher Waas** für die unvergessliche Zeit und großartige Atmosphäre im Büro, mit Spaß in der Halbe und produktiver Arbeitsatmosphäre in der andern Hälfte. Danke dir für die gegenseitige Hilfe, wenn einer einmal kurz eine zweite helfende Hand benötigt hat. Ich hatte großes Glück, an den dir gegenüberliegenden Tisch gesetzt zu werden.

- Euch vielen anderen Masterstudenten, die ihr stets für eine freundliche, spaßige und trotzdem produktive Stimmung gesorgt haben - insbesondere **Elisabeth Meidinger**, **Julia Lamprich**, **Monika Scheufele**, **Philipp Krüger** und **Philip Schwenke**.

- Dem gesamten technischen Personal des WMI, dem ich mit meinen Fragen und Ideen auf die Nerven gehen durfte. Im besonderen Andreas Russo, bei dem ich zahlreiche Stunden und Tage in der Elektronikwerkstatt verbrachte.

- Den Spitzen-Expertinnen und Laborassistentinnen im Bereich Sauberkeit, Maria Botta und Sybilla Plöderl, ohne die das Institut höchstwahrscheinlich binnen weniger Tage oder vielleicht sogar Stunden im allumfassenden Chaos versinken würde.

- Ein weiteres Dankeschön geht an meine Leidensgenossen aus dem Bachelor, **Fabian Salamon**, **Maximilian Ries** und **Paul Heinrich**, mit denen ich quasi jede Hausaufgabe anfertigte. Im Besonderen geht es an Maxi und Fabi für das gemeinsame Lernen auf jede Prüfung sowie die vielen Aktivitäten auch abseits des Uni-Alltags. Ohne euch hätte ich sicherlich das Mikrofon fallen gelassen und wäre einfach gegangen. Ein besonderer Dank darüber hinaus gilt dir, Fabi, da du mich auch im Master noch in einigen Vorlesungen ertragen hast und ich, mehr oder weniger ungeplant, mit dir die gemeinsame Ehre auf meinem Auslandssemester in Stockholm hatte.

- Meinen Freunden abseits der Uni, die mich immer unterstützen und nicht müde werden, mir zu sagen, wir krass das alles ist, was ich mache. Im besonderen gilt der Dank **Christian Budulack**, **Fritz Jüstel**, **Jennifer Niedermaier**, **Johannes Weiß**, **Maik Kaya**, **Robin Steil**, **Thomas Reibert** und allen, die ich aus Schusseligkeit vergessen habe.

- Wie immer kommst das Beste zum Schluss. Ich möchte mich bei den **besten Eltern** und der allgemein **besten Familie** bedanken, die ich mir vorstellen und wünschen kann. Ohne euch und eure Unterstützung in allen Belangen hätte ich nie angefangen geschweige denn die Möglichkeit gehabt, Physik zu studieren.

Danke euch allen für die großartige Zeit! Ich möchte mit einem kleinen Auszug schließen, der - wie ich finde - den Schreibprozess einer wissenschaftlichen Arbeit mit großem Humor und sehr treffend beschreibt. Bonuspunkte gibt es für all diejenigen, die diese kurzen Verse ihrem größeren Gesamtwerk zuordnen können [Goe01].

> Geschrieben steht: „Im Anfang war das Wort!“
> Hier stock ich schon! Wer hilft mir weiter fort?
> Ich kann das Wort so hoch unmöglich schätzen,
> Ich muss es anders übersetzen,
> Wenn ich vom Geiste recht erleuchtet bin.
> Geschrieben steht: Im Anfang war der Sinn.
> Bedenke wohl die erste Zeile,
> Dass deine Feder sich nicht übereile!
> Ist es der Sinn, der alles wirkt und schafft?
> Es sollte stehn: Im Anfang war die Kraft!
> Doch, auch indem ich dieses niederschreibe,
> Schon warnt mich was, dass ich dabei nicht bleibe.
> Mir hilft der Geist! Auf einmal seh ich Rat
> Und schreibe getrost: Im Anfang war die Tat!